Charles University in Prague
Faculty of Mathematics and Physics

MASTER THESIS

František Lukáč

Investigation of defects in Fe_3Al - based alloys by positron annihilation spectroscopy

Department of Low-Temperature Physics

Supervisor: doc. Mgr. Jakub Čížek, Ph.D.
Study programme: Physics
Specialization: Physics of Condensed Matter and Materials

Prague 2011

Acknowledgements

I would like to thank doc. Čížek for enabling the measurements and calculations performed in this work at the equipments of Positron annihilation laboratory of Low-Temperature physics and for his kind guidance, priceless advices and experiences helpful for handling the experimental data. My gratitude also goes to group of authors of the software ATSUP in [11] which enabled the theoretical quantum-mechanics calculations.

I hereby declare that I carried out this master thesis independently, and exclusively with the use of the cited sources, literature and other professional sources.

I understand that my work relates to rights and obligations under the Act No. 121/2000 Coll., the Copyright Act, as amended, in particular, that the Charles University in Prague has the right to conclude a license agreement for the use of this work as a school work according to Section 60 Paragraph 1 of the Copyright Act.

In ..... date .....

Název práce: Studium defektů ve slitinách na bázi Fe_3Al metodou pozitronové anihilační spektroskopie

Autor: Bc. František Lukáč
Katedra: Katedra fyziky nízkych teplot
Vedoucí diplomové práce: doc. Mgr. Jakub Čížek, Ph.D.

Abstrakt: V zliatinách železa a hliníku bola študovaná korelácia koncentrácie vakancií s mikrotvrdosťou vzorkov zakalených z 1000 °C a následne žíhaných na nižších teplotách. Pomocou difrakcie röntgenovho žiarenia bola zistená mriežková konštanta a kryštalografická niektorých vzorkov Fe-Al zliatin. Meraním doby života pozitronov bola zistená vysoká koncentrácia vakancií v zakalených vzorkoch a následné žíhanie vzorkov spôsobilo značný pokles koncentrácie vakancií, pričom vo vzorkoch s obsahom hliníka nad 39% bol nameraný pokles mikrotvrdosti. Koincidenčné meranie Dopplerovského rozšírenia anihilačného píku vzorku pomohlo rozlíšiť anihilácie pochádzajúce od zachyteného a delokalizovaného pozitronu anihilovaného elektrónmi od oboch typov atómov, Fe a Al. Porovnaním týchto výsledkov s teoretickými kvantovo-mechanickými výpočtami prevedenými v tejto dilpomovej práci bol určený najpravdepodobnejší typ defektu ako vakancia v A-podmriežke B2 štruktúry.

Klíčová slova: vakance pozitronová anihilační spektroskopie Fe-Al slitiny mikrotvrdost

Title: Investigation of defects in Fe_3Al - based alloys by positron annihilation spectroscopy

Author: Bc. František Lukáč
Department: Department of Low-Temperature Physics
Supervisor: doc. Mgr. Jakub Čížek, Ph.D.

Abstract: The correlation of vacancy concentration with microhardness of Fe-Al alloys was studied on samples quenched from 1000 °C and subsequently annealed at lower temperatures. Using X-ray diffraction the lattice parameter and crystal structure were determined for samples of Fe-Al alloys. By measurements of positron lifetime was revealed the high concentration of vacancies in quenched samples and subsequent annealing caused significant decrease in vacancy concentration while in samples with Al content above 39% also the decrease of microhardness was measured. Measurements of coincidence Doppler broadening of annihilation peak helped to distinguish the annihilations comming from positron trapped or delocalized annihilated by electrons of both atoms, Fe and Al. Comparison of measured results with theoretical quantum-mechanics calculations performed in this diploma thesis determined the most probable defect type as a vacancy on A-sublatice of B2 structure.

Keywords: vacancy positron annihilation spectroscopy Fe-Al alloys microhardness

Contents

Appendix

Introduction

Binary alloys of iron and aluminium are industrially interesting materials for their exceptional resistance to corrosion and advantageous strength-to-weight ratio. Moreover, at high temperatures these properties are preserved. Important for understanding of the behavior of intermetallics such as Fe-Al materials is investigation of vacancy-like point defects because vacancy concentrations of Fe-Al alloys are of several orders higher than in pure metals.

Positron annihilation spectroscopy is non-destructive method for studying defects in solid state materials. Measuring of the positron lifetime enables to classify defects type, volume size and concentration. Measuring of coincidence Doppler broadening of annihilation peak carries information about chemical environment of a positron trapped at the defect. The measurements are supported by quantum-mechanics theoretical calculations which help us to interpret the measured data. Mechanical properties were studied simultaneously by the measuring of Vickers microhardness and compared with the positron annihilation spectroscopy results. The correlation of defect concentration with mechanical properties was observed in Fe-Al alloys with various composition and after various thermal treatments.

Chapter 1

The methods of measurement

1.1 The measurement of positron lifetime

The measurement of positron lifetime in solid matter is a non-destructive method applied for investigations of defects and free volumes. This method takes advantage of the property of the positron source nucleus ^{22}Na which decays according to decay scheme it the Figure 1. After β^+-decay it subsequently deexcites by emission of a photon with the energy of 1274 keV - so-called start signal.

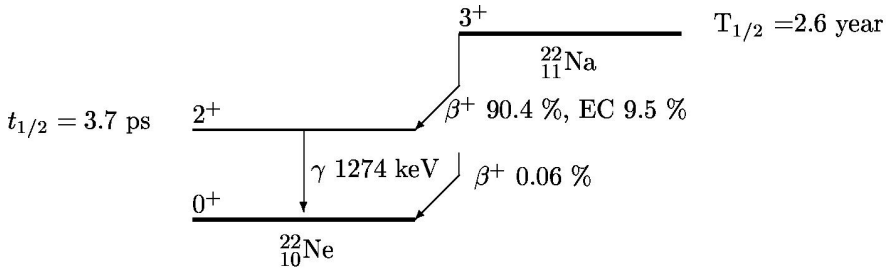

Figure 1: The decay scheme of the radiation source ^{22}Na. The half-life of the radioisotope ^{22}Na is $T_{1/2}$ =2.6 year, the half-life of the radioisotope ^{22}Ne is $T_{1/2}$ = 3.7 s.

Positron implantated in the studied sample thermalizes, i.e. looses its kinetic energy down to $k_BT = 39$ meV at the room temperature T. The energy losses are at high energies caused by ionization, subsequently at lower energies by excitation of the inner-shell electrons, then by excitation of the conducting electrons and at the last stage at epithermal energies by the phonon scattering. The mean kinetic energy of positrons emitted by ^{22}Na radioisotope is 270 keV. These positrons are thermalized in metals typically within a few picoseconds and the mean positron penetration depth falls in the range 10-100 μm [1]. Thermalized positron lives in the thermal equilibrium for certain time until it annihilates with an electron and mostly the two γ-rays are emitted with the energy close to 511 keV. The time interval between detection of the start signal and detection of the annihilation γ-ray equals to positron lifetime. Hence, measurement of time difference between detection of the start signal and the annihilation γ-ray allows the determination of the positron lifetime in the solid matter.

Positron in thermal equilibrium in a solid is scattered on phonons and in the classical approach it makes an isotropic random movement. The positron

diffusion coefficient D_+ in solids falls in the range from 0.1 to 2 $\mathrm{cm^2 s^{-1}}$ at the room temperature. Mean positron diffusion length $L_{+,B}$ is the mean distance from the place of the end of thermalization process to the place where it gets by diffusion motion during its lifetime τ_B. The relationship of the above mentioned quantities is

$$L_{+,B} = \sqrt{D_+ \tau_B}. \tag{1.1}$$

In metals $L_{+,B}$ is 100-200 nm and positron explores the volume containing about 10^7 atoms [1].

Annihilation rate λ_B of delocalized positron in metals is proportional to the overlap of the positron and electron density [1]

$$\lambda_B = \pi r_e^2 c \int \rho_+(\mathbf{r}) \rho_-(\mathbf{r}) \gamma(\mathbf{r}) d^3\mathbf{r}, \tag{1.2}$$

where $r_e = e^2/(4\pi\epsilon_0 mc^2)$ is the classical Thompson radius of the electron, $\rho_+(\mathbf{r})$ and $\rho_-(\mathbf{r})$ is the positron and electron density, respectively.

A delocalized positron attracts the electrons and causes an enhancement of electron density at positron site. Electron-positron correlation, which is taken in amount in equation (1.2) by the enhancement factor $\gamma(\mathbf{r})$, caused by the Coulombic attractive interaction increases positron annihilation rate λ_B. Therefore, it decreases the bulk positron lifetime τ_B, which is the inverse of the annihilation rate

$$\tau_B = \frac{1}{\lambda_B}. \tag{1.3}$$

In a perfect defect-free material the probability $n(t)$ that a positron is alive at the time t (measured from the moment of the implantation to the material) is given by expression

$$n(t) = \mathrm{e}^{-\lambda_B t}. \tag{1.4}$$

Hence, with a sufficient statistics of annihilation events measurement of positron lifetime results in exponential dependence of the number of annihilations on time. The positron lifetime $\tau_B = 1/\lambda_B$ is the mean value of this distribution. The real positron lifetime spectrum S is the convolution of the ideal spectrum

$$S_{id}(t) = -\frac{\mathrm{d}n(t)}{\mathrm{d}t} = \lambda_B \mathrm{e}^{-\lambda_B t} \tag{1.5}$$

with the resolution function R of the spectrometer with added background B caused by the random coincidences.

$$S(t) = S_{id}(t) * R(t) + B. \tag{1.6}$$

In the metals the positron bulk lifetime falls in the interval from 100 to 300 ps. In this work positron lifetimes were measured by digital spectrometer with the time resolution of 145 ps (FWHM of the resolution function $R(t)$) and the coincidence count rate 100 / s with 1.5 MBq ^{22}Na positron source [2, 3]. If a solid contains defects associated with free volume then of the repulsive interaction among positron and positive ions in the lattice is reduced in the defect site. As a consequence localized positron state may be formed in defect with lower energy eigenvalue than in the delocalized positron state. The energy difference of positron trapped at defect and delocalized positron defines the binding energy E_B of the

positron to the defect E_B. Since local electron density in open-volume defects is lowered the overlap of positron wavefunctions with electrons is smaller. The lifetime of the positrons trapped in open volume defect, e.g. vacancy, is therefore longer than the lifetime of delocalized positrons. The lifetime of trapped positrons increases with increasing open space in defect, e.g. lifetime of positrons trapped at vacancy cluster is longer than lifetime of positrons trapped in monovacancy.

Simple trapping model (STM) is used for the qualitative description of positron trapping at one type of defects [1]. Thermalized positron can annihilate only from free or trapped state. The probability that a positron is in the time t alive and in the free state is denoted $n_B(t)$ and the probability that positron is at time t alive and trapped at defect is $n_D(t)$. Trapped positron annihilates with the annihilation rate λ_D which reflects local electron density in defect and therefore it is a characteristic quantity for certain type of defect. In metals with the high concentration of vacancies positron trapping is transition limited process. The time necessary to the diffusion of the positron to the defects is negligible and the trapping rate is limited by the cross section of the quantum-mechanical transition from the delocalized state to the bounded state in the defect. The probability of capture of a free positron in defect is given by the trapping rate of defect K_D.

STM can be used for description of the kinetics of positron trapping when the following assumptions are fulfilled
1. only the thermalized positron can be trapped,
2. detrapping to the delocalized state is negligible,
3. spatial distribution of defects in the sample is uniform.

We obtain following form of the kinetic equations:

$$\frac{\mathrm{d}n_B(t)}{\mathrm{d}t} = -(\lambda_B + K_D)n_B(t) \tag{1.7}$$

$$\frac{\mathrm{d}n_D(t)}{\mathrm{d}t} = -\lambda_D n_D(t) + K_D n_B(t). \tag{1.8}$$

$$\tag{1.9}$$

Solving this system of equations (1.7) and (1.8) with the initial conditions $n_B(0) = 1$ and $n_D(0) = 0$ we obtain

$$n_B(t) = \mathrm{e}^{-(\lambda_B + K_D)t} \tag{1.10}$$

$$n_D(t) = \frac{K_D}{\lambda_B - \lambda_D + K_D}(\mathrm{e}^{-\lambda_D t} - \mathrm{e}^{-(\lambda_B + K_D)t}). \tag{1.11}$$

$$\tag{1.12}$$

The ideal positron lifetime spectrum is two-component

$$S_{id}(t) = -\frac{\mathrm{d}(n_B + n_D)}{\mathrm{d}t} = \lambda_1 I_1 \mathrm{e}^{-\lambda_1 t} + \lambda_2 I_2 \mathrm{e}^{-\lambda_2 t}. \tag{1.13}$$

For lifetimes annihilation rates and relative intensities of the components one can derive from equations (1.10) - (1.13)

$$\tau_1 = \frac{1}{\lambda_1} = \frac{1}{\lambda_B + K_D}, \quad I_1 = 1 - I_2 \tag{1.14}$$

$$\tau_2 = \frac{1}{\lambda_2} = \frac{1}{\lambda_D}, \qquad I_2 = \frac{K_D}{\lambda_1 - \lambda_D}. \tag{1.15}$$

The shorter component with the lifetime τ_1 comes from annihilations of free positrons while the longer component with the lifetime τ_2 represents the contribution of positrons trapped at defects.

The trapping rate to defects is proportional to the defect concentration c_D

$$K_D = \nu_D c_D, \tag{1.16}$$

where ν_D is the specific positron trapping rate of to the defect. From the relations (1.14) - (1.15) the positron trapping rate can be derived as

$$K_D = \frac{I_2}{I_1}\left(\frac{1}{\tau_B} - \frac{1}{\tau_2}\right). \tag{1.17}$$

In the case of more than the one type of defects in the sample additional components appears in positron lifetime spectrum. Each defect component exhibits different lifetime characteristic for each type of defect. Therefore, the real measured spectrum is a superposition of certain contributions with various lifetimes and intensities. It inevitably contains also a contribution of positrons annihilated in the source spot and in the covering foil. The annihilations coming from the sample arise from the different types of defects or from free positrons. With the increasing concentration of defects in the sample the intensity and also lifetime of the short-lived free positron component decreases. In practice it is impossible to resolve the free positron component in the positron lifetime spectrum when its intensity falls below $\sim$5%. This is called saturated positron trapping. For the vacancies in the Fe-Al alloys the maximum concentration which causes the saturated trapping of the positrons in defects is

$$c_{Vmax,LT} \approx 2 \times 10^{-4} at.^{-1}. \tag{1.18}$$

Within STM the quantity τ_f calculated from the relation

$$\tau_f = \left(\frac{I_1}{\tau_1} + \frac{I_2}{\tau_2}\right)^{-1} \tag{1.19}$$

equals the lifetime of positrons in defect-free material τ_B. Hence, equation (1.19) can be used to check if STM assumptions are fulfilled.

The positron trapping rate at a defect determines the fraction of trapped positron annihilations F_D as

$$F_D = \frac{K_D}{\lambda_B + K_D}. \tag{1.20}$$

1.2 Coincidence Doppler Broadening - CDB

The coincidence measurement of the Doppler broadening of the annihilation peak (CDB) is convenient method for investigations of chemical environment of defects. Every chemical element has a unique shape of the CDB spectrum. Since thermalized positron has negligible momentum compared to electrons, the momentum of annihilating electron-positron pair is given by the momentum of electron. Hence, by measuring the Doppler shift in energy of the annihilation γ-rays we obtain knowledge about momentum distribution of electrons which annihilated positrons. In the center-of-mass frame the total momentum of the annihilating pair electron-positron is zero. The law of conservation of momentum requires for both annihilation photons to be strictly anticolinear with the energy which equals the rest mass of positron 511 keV. In the laboratory frame the annihilation photons deviate from the anticolinearity because of a nonzero momentum of the annihilation pair as illustrated in Figure 2. The longitudal and the transversal

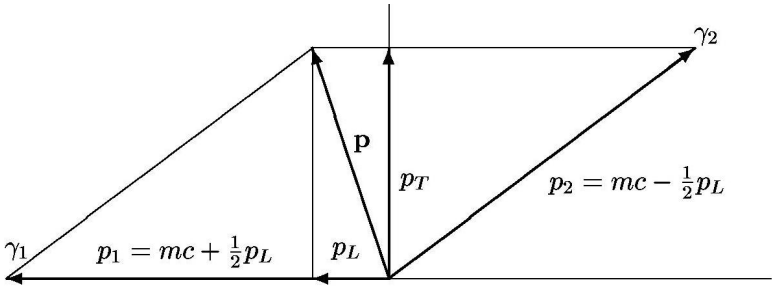

Figure 2: Vector diagram of the momentum conservation law in the annihilation process.

component of the momentum $\mathbf{p}$ are denoted as p_L and p_T, respectively. The motion of the annihliation pair in the laboratory frame causes a Doppler shift in the energy of the annihilation photons measured in the laboratory frame. The shift in frequencies is expressed as $\Delta\nu/\nu \approx v_L/c$, therefore, the longitudal velocity is $v_L = p_L/2m$. The relative Doppler shift in the energy is $\Delta E/E = \Delta\nu/\nu$, therefore,

$$\Delta E = \frac{v_L}{c}E = c\frac{p_L}{2}. \tag{1.21}$$

Hence, the Doppler shift in the energy depends on the longitudal component of the electron momentum.

Measurement of energy of both annihilation photons in coincidence suppresses the accidental events from the background by the recording only events of the simultaneous detection of both annihilation γ-rays. The difference in energies of the two annihilation photons is

$$E_1 - E_2 = 2\Delta E = cp_L, \tag{1.22}$$

i.e. it is directly proportional to the component of electron momentum to the direction of emitted annihilation photon. The sum of the energies provides us the information about the resolution function of the apparature. The CDB spectrometer is equipped with two semiconductor High purity Ge detectors. The overall

energy resolution of CDB spectrometer is 1.0 keV (FWHM) at the energy of 511 keV. With 1.5 MBq positron source ^{22}Na approximately 500 coincidences per second are recorded. At least 100 millions of positron annihilation events were accumulated in each CDB spectrum.

1.3 Slow positron implantation spectroscopy SPIS

Slow Positron Implantation Spectroscopy (SPIS) is a method investigating a sample by the beam of slow monoenergetic positrons. Positrons are magnetically guided from the positron source to the accelerator which enables to accelerate positrons up to the energies from 30 eV to 36 keV. The positron thermalization process is influenced by the initial positron energy and therefore it is possible to investigate different depths of the sample. The Germanium detector with the average resolution 1.09 keV (FWHM at the energy 511 keV) is used to measure th Doppler broadening of the annihilation peak in the spectrum. The S-parameter determined from the spectrum is defined as the ratio of the area under the certain energy interval around the center of the peak. The initial positron energy is changed and the changes in the S-parameter are observed during experiment. Contributions to the small Doppler shifts are caused by the positrons localized in the defects, e.g. vacancies, because they annihilate mostly with free electrons with the lowest momentum. Therefore, the S-parameter increases with the increasing concentration of defects. The trapping rate of a vacancy K_V is the probability of the capture of a free positron in the vacancy and is determined by

$$K_V = \frac{1}{\tau_B}\left(\frac{L_{+,B}^2}{L_+^2} - 1\right), \tag{1.23}$$

where $L_{+,B}$ is positron diffusion length in defect-free material from the relation (1.1), L_+ is the positron diffusion length in the studied sample. Positron diffusion length can be obtained because of the different properties of the the material in the volume and on its surface. After thermalization positron moves in a sample by random motion. If positrons thermalize in the depth smaller than the positron diffusion length some of the positrons diffuse to the surface and annihilates there. The high-energy positrons which penetrates to the sample deeper than the positron diffusion length L_+ have the same bulk annihilation S-parameter because the diffusion to the surface is impossible for these positrons due to the trapping on defects. The low-energy positrons S-parameter is different because some positrons annihilate on the surface. By fitting the increase of S-parameter one can obtain the positron diffusion length L_+ in the sample. Diffusion coefficient D_+ in defect-free Fe_3Al is the weight average of iron and aluminium diffusion coefficients [4]

$$D_+ \approx \frac{3}{4}D_{+,Fe} + \frac{1}{4}D_{+,Al} = 3cm^2s^{-1} \tag{1.24}$$

Trapping rate of the vacancy K_V is directly proportional to the concentration of vacancies c_V calculated from the equation

$$c_V = \frac{K_V}{\nu_V} \tag{1.25}$$

where is the specific positron trapping rate $\nu_V = 4 \times 10^{14} at.s^{-1}$ for the vacancy in Fe_3Al [5].

1.4 X-Ray Diffraction

Some of the samples were studied by the X-ray diffraction. It is valuable precise method for determination of the crystallographic structure of the sample [6]. Polycrystalline samples are studied by the means of the powder diffraction, which gives us the accurate values of inter-planar spacing in the crystalline lattice. The condition for diffraction of X-rays on planes with Miller indexes (hkl) is expressed by Bragg law

$$2d_{hkl}sin(\theta_{hkl}) = \lambda \tag{1.26}$$

where λ is the wavelength of X-rays, d_{hkl} is the inter-planar spacing of (hkl) planes and θ_{hkl} is the scattering angle, i.e. angle between the incidence beam and the normal to the sample surface. In the case of the monocrystalline sample it is possible to fulfill the Bragg condition by appropriate orientation of the crystal with respect to the incidence beam. For polycrystalline samples or powder samples with random orientation of individual crystalites some grains are likely oriented so that the (hkl) planes are in the diffraction position. This probability is increased by the number of the grains in the coherently irradiated volume. The X-rays diffracted by the (hkl) planes are scattered in the direction having the angle $2\theta_{hkl}$ with respect to the incident beam. If we rotate certain grain around the axis identical with the incidence beam direction the (hkl) planes remain in the diffraction condition and diffracted beam moves on the surface of a cone with the angle $4\theta_{hkl}$ and the axis in the direction of the incidence beam. Diffracted X-rays from all grains having (hkl) planes in the diffraction condition are scattered along this cone surface. If we take into account all planes with the inter-plannar distance which fulfills the Bragg law condition for given X-rays wavelength we obtain as the final diffraction effect a system of cone surfaces with axis identical with the direction of the incident beam and with cone angles $4\theta_{hkl}$ given by the interplannar distances. It is obvious that by the measuring of the diffraction angles one can measure the inter-plannar distances.

Using measured diffractogram one can determine the lattice parameters and geometry of the crystal lattice from positions of diffraction peaks. From integral intensities of the diffraction peaks one can determine the real structure of the sample, the texture, the size of the crystallites and the deformation stored in the sample. Positions and intensities of diffraction peaks can be extracted from the continuously recorded diffraction spectra. Presently the three groups of method exist on the dealing with the powder diffractograms: the direct analysis of the isolated diffraction lines, the approximation of the diffraction profiles by the appropriete analytical functions and approximation of the whole spectrum by the sum of the analytical functions calculated for the analyzed structure and taking into account the instrumental resolution function.

In this work diffraction peaks were fitted by by the Pearson VII function [7] including the background under the peak. The position of peak maximum was determined from fitting. Broadening of diffraction peaks is characterized by the integral breadth β, which is defined as the ratio of the peak area to the peak maximum. There are two options how to calculate the integral breadth: (i) calculate area under the experimental diffraction peak with subtracted background or (ii) to integrate the model function. Integral breadths determined using these two

approaches will be denoted as β_{exp} and β_{mod} respectively. Although in ideal case these breadths should equal to each other, the asymmetry of the peaks causes certain deviation of these values.

X-ray diffraction pattern reflects the crystal structure, more specifically the unit cell of the measured crystal. Every chemical element interacts uniquely with X-rays. The function describing intensity of X-rays scattered from one atom is called atom form factor. The atom form factor f_{at} is the Fourier transformation of the electron density at the atom

$$f_{at}(\vec{q}) = \int_V \rho(\vec{r}) exp(i\vec{q} \cdot \vec{r}) d\vec{r} \tag{1.27}$$

where $\vec{q}$ is diffraction vector, $\rho(\vec{r})$ is the electron density at the atom. When considering n-th atom in the m-th unit cell one can describe the whole crystal volume by the position vector

$$\vec{R_m^n} = m_1\vec{a} + m_2\vec{b} + m_3\vec{c} + \vec{r_n} \tag{1.28}$$

where $\vec{r_n}$ denotes the position only in the unit cell and the rest denotes the position of the unit cell in the volume of the crystal. The structure factor $F(\vec{q})$ describes the scattering on the unit cell containing N atoms indexed by n.

$$F(\vec{q}) = \sum_{n=1}^{N} f_n exp(i\vec{q} \cdot \vec{r_n}). \tag{1.29}$$

Here f_n is the form factor of n-th atom in the unit cell. If $\vec{q}$ fulfills the diffraction condition $\vec{q} = \vec{G}_{hkl}$, where $\vec{G}_{hkl} = ha^* + kb^* + lc^*$ is a vector in the reciprocal lattice and a^*, b^*, c^* are reciprocal lattice base vectors [6], then the structure factor is

$$F_{hkl} = \sum_{n=1}^{N} f_n exp[2\pi i(hx_n + ky_n + lz_n)] \tag{1.30}$$

The structure factor may cause extinction of diffraction peaks when $F_{hkl} = 0$ because the intensity of the diffracted radiation depends on the structure factor $I \propto |F_{hkl}|^2$.

The indexation of the peaks in powder diffractogram means association of the diffraction indices with the corresponding diffraction lines. It is important to realize that in the powder diffraction chosen diffraction indices correspond to the whole set of equivalent planes. The occurence of the extinction of diffraction peaks is related to the symmetry of the crystal and the elementary cell.

In cubic structures all possible diffractions are present only in the crystals with the simple cubic elementary cell. Some diffractions extinct in the body centered and face centered cubic cells. The following equation is useful for indexation of the diffraction record of cubic crystal

$$\frac{1}{d_{hkl}^2} = \frac{h^2 + k^2 + l^2}{a^2}. \tag{1.31}$$

Here a is the lattice parameter and h, k, l are the diffraction indices. One can calculate the values Q_i:

$$Q_i = \frac{1/d^2_{hi,ki,li}}{1/d^2_{h1,k1,l1}} = \frac{h_i^2 + k_i^2 + l_i^2}{h_1^2 + k_1^2 + l_1^2}, \tag{1.32}$$

where indices 1 and i denotes the first and i-th diffraction, respectively. The ratios Q_i do not depend on the size of the lattice parameter but only on the values of the allowed h, k, l for each structure type [8]. By comparison of Q_i values obtained in experiment with literature one can find out the structure type. Extinction rules for given structure are used for indexation of diffraction lines and the sequence of the diffraction indices characterized by increasing sum $h^2 + k^2 + l^2$ is created. Approximate values of the lattice parameter are obtained from equation (1.31).

Our intention when measuring powder diffraction is to obtain the lattice parameter as precise as possible. For determination of the lattice parameter a it is efficient to use as many diffractions as possible including peaks at hugest diffraction angles. For cubic materials one can obtain a_{hkl} from the inter-planar distances d^2_{hkl} by the relation (1.31). However the accuracy of a_{hkl} values determined from positions of various diffraction peaks is unequal because of systematic errors. For the conventional bulk diffraction in Bragg-Brentano symmetric geometry the extrapolation function of $\cos\theta \cot\theta$ is used. The extrapolation corrects the error from the excentric position of the sample in the center of the goniometer circle. Accurate lattice parameter a_e can be obtained from the linear regression of the Cohen-Wagner plot

$$a_{hkl} = a_e + s \cos\theta \cot\theta \tag{1.33}$$

where s is a constant which includes instrumental factors.

Shape of a diffraction profile is influenced by two different types of broadening. The instrumental broadening is caused by the resolution function of the apparatus. This can be experimentally found out by the measuring standards, i.e. high quality crystals which exhibit high narrow diffraction peaks resembling to the δ-function (e.g. high quality Si or LaB_6). In addition to instrumental broadening there are also physical factors causing broadening of diffraction profiles. The deconvolution of the measured profile using experimental resolution function determined by measurement of standards gives the physical broadening of the diffraction peak. Width of diffraction profile is influenced by the mean size of crystallites and by presence of microstrains introduced e.g. by dislocations.

1.5 Vickers Microhardness

The first step in measuring of Vickers microhardness constists of pressing the diamond intender of certain geometry with precise load to the sample surface. The second step is the measuring of the size of the mark left on the sample with surface polished to the optical mirror. The microhardness was measured by STRUERS Duramin-2 micro-tester. The load of 100 gram was applied for 10 seconds. The tip of the intender is of defined pyramidal shape with the angle 136°. The square-like mark on the surface is measured by the optical microscope equipped with measuring line scale in the objective. The diagonal size of the square is measured and the Vickers microhardness HV0.1 is calculated from the equation

$$HV = \frac{F}{A} = \frac{2F\sin(136°/2)}{d^2} \tag{1.34}$$

where F is the force applied by the load, A is the size of the intendation and d is the size of the diagonals.

Chapter 2

Theoretical calculations

2.1 Two-component density functional theory

Quantum-mechanical calculations of positron parameters were performed in this diploma thesis. The first principle calculations can be made in principle by the two approaches: Hartree-Fock method (HF) and Density functional theory (DFT). HF calculations are with the increasing number of atoms enormally demanding on the computation time and the computers performance. The DFT calculation are much more affordable and were successfully employed even in complicated systems. In DFT theory the functional of the energy dependent only on the electron density is constructed. In the two-component model the functional depends on the positron density, too. The minimum of the functional is found iteratively by a self-consistent variational method. The program on the solution of the following equations was written in the *FORTRAN* programming language. It enables to calculate the annihilation characteristics of the positron in the material, which allows the comparing with the physical measurements. By this means it is possible to find out what is happening in the material when varying the conditions and how changes observed in experiment are related to the concentration and type of the defects, the size, geometry and the chemical environment of defects. Theoretical calculations are essential for proper interpretation of experimental results obtained by positron annihilation spectroscopy.

2.2 Kohm-Sham equations

The Kohm-Sham equations are principal equations of DFT. The total energy of the quantum-mechanical system of interacting electron and positron E is expressed as a functional of the electron and the positron densities $n_+(\mathbf{r}), n_-(\mathbf{r})$.

$$\begin{aligned} E[n_+, n_-] = T_0[n_+] + T_0[n_-] + \int V_{ext}(\mathbf{r})(n_-(\mathbf{r}) - n_+(\mathbf{r}))d^3(\mathbf{r}) \\ - \int\int \frac{n_+(\mathbf{r})n_-(\mathbf{r})}{|(\mathbf{r}) - (\mathbf{r}')|} d^3(\mathbf{r}')d^3(\mathbf{r}) \\ + \frac{1}{2}\int\int \frac{n_+(\mathbf{r})n_+(\mathbf{r}')}{|(\mathbf{r}) - (\mathbf{r}')|} d^3(\mathbf{r}')d^3(\mathbf{r}) + \frac{1}{2}\int\int \frac{n_-(\mathbf{r})n_-(\mathbf{r}')}{|(\mathbf{r}) - (\mathbf{r}')|} d^3(\mathbf{r}')d^3(\mathbf{r}) \\ + E_c^{e-p}[n_+, n_-] + E_{xc}[n_+] + E_{xc}[n_-] \end{aligned} \tag{2.1}$$

First three terms express the kinetic energy of the non-interacting positron and electron gas and the external potential. The double integral terms accounts for the Coulombic interaction of these particle densities of each other and by itself. The term E_c^{e-p} represents the positron-electron correlation energy and the terms E_{xc} describe the exchange correlation energy.

For the seeking of the minimum of the functional (2.1) variation principle is used. By the variation of the functional we get the Kohm-Sham equations for the system.

$$\frac{\delta E[n_+,n_-]}{\delta n_-} = \frac{\delta T_0[n_-]}{\delta n_-} + V_{ext}(\mathbf{r}) + \int \frac{n_+(\mathbf{r}') - n_-(\mathbf{r}')}{|(\mathbf{r}) - (\mathbf{r}')|} d^3(\mathbf{r}') + \frac{\delta E_c^{e-p}[n_+,n_-]}{\delta n_-} + \frac{\delta E_{xc}[n_-]}{\delta n_-} = \mu_-. \tag{2.2}$$

$$\frac{\delta E[n_+,n_-]}{\delta n_+} = \frac{\delta T_0[n_+]}{\delta n_+} - V_{ext}(\mathbf{r}) + \int \frac{n_+(\mathbf{r}') - n_-(\mathbf{r}')}{|(\mathbf{r}) - (\mathbf{r}')|} d^3(\mathbf{r}') + \frac{\delta E_c^{e-p}[n_+,n_-]}{\delta n_+} + \frac{\delta E_{xc}[n_+]}{\delta n_+} = \mu_+. \tag{2.3}$$

The chemical potentials μ_-, μ_+ on the right hand side of the equations (2.2) - (2.3) have the function of the Lagrange multiplicators which guarantee the constant number of particles.

For the non-interacting electrons and positrons in the potential $V_{eff}(\mathbf{r})$ these equations take form

$$\frac{\delta E[n_+,n_-]}{\delta n_-} = \frac{\delta T_0[n_-]}{\delta n_-} + V_{eff}(\mathbf{r}) = \mu_-, \tag{2.4}$$

$$\frac{\delta E[n_+,n_-]}{\delta n_+} = \frac{\delta T_0[n_+]}{\delta n_+} - V_{eff}(\mathbf{r}) = \mu_+. \tag{2.5}$$

The comparison of the equations for the non-interacting particles (2.4)-(2.5) with equations (2.2)-(2.3) one can rewrite $V_{eff}(\mathbf{r})$ in the equations (2.4)-(2.5) and self-consistently solve the one-particle Schrödinger equations

$$-\frac{1}{2}\Delta\psi_i^-(\mathbf{r}) + \{V_{ext}(\mathbf{r}) + \int \frac{n_-(\mathbf{r}') - n_+(\mathbf{r}')}{|(\mathbf{r}) - (\mathbf{r}')|} d^3(\mathbf{r}') + \frac{\delta E_c^{e-p}[n_+,n_-]}{\delta n_-} + \frac{\delta E_{xc}[n_-]}{\delta n_-}\}\psi_i^-(\mathbf{r}) = \epsilon_i\psi_i^-(\mathbf{r}) \tag{2.6}$$

$$-\frac{1}{2}\Delta\psi_i^+(\mathbf{r}) - \{V_{ext}(\mathbf{r}) + \int \frac{n_-(\mathbf{r}') - n_+(\mathbf{r}')}{|(\mathbf{r}) - (\mathbf{r}')|} d^3(\mathbf{r}') - \frac{\delta E_c^{e-p}[n_+,n_-]}{\delta n_+} - \frac{\delta E_{xc}[n_-]}{\delta n_+}\}\psi_i^+(\mathbf{r}) = \epsilon_i\psi_i^+(\mathbf{r}) \tag{2.7}$$

where positron and electron densities are

$$n_-(\mathbf{r}) = \sum_{\epsilon_i(<\epsilon_F)} \left|\psi_i^-(\mathbf{r})\right|^2, n_+(\mathbf{r}) = \sum_i^{N_+} \left|\psi_i^+(\mathbf{r})\right|^2 \tag{2.8}$$

where $\psi_i^+(\mathbf{r})$ and $\psi_i^-(\mathbf{r})$ are the wavefunctions of the positron and electron which solve the Kohn-Sham equations, ϵ_F is the Fermi energy of electrons and N_+ is the number of positrons in the solid. For the computing performance these equations are too demanding so the physical approximations are made to make the calculations tractable in reasonable time.

2.3 Approximations in the calculations

When using the conventional laboratory source of the activity roughly 1 MBq on average only one positron enters the material in one microsecond. The observed lifetimes of the positron in the solid matter do not exceed a few ns. The probability that more than one positron is in the sample at the same time is therefore negligible. Hence, one can use the limit of low positron density with the self-interacting correction (SIC); the positron exchange-correlation term and the Hartree positron Coulombic term cancel in (2.7)

$$\frac{\delta E_{xc}[n_+]}{\delta n_+} + \int \frac{n_+(\mathbf{r}')}{|(\mathbf{r}) - (\mathbf{r}')|} d^3(\mathbf{r}') = 0. \tag{2.9}$$

The potential for the positron then contains only the following terms

$$V_{eff}(\mathbf{r}) = -V_{ext}(\mathbf{r}) + \frac{\delta E_c^{e-p}[n_+, n_-]}{\delta n_+} - \int \frac{n_-(\mathbf{r}')}{|(\mathbf{r}) - (\mathbf{r}')|} d^3(\mathbf{r}'). \tag{2.10}$$

The term $V_{ext}(\mathbf{r})$ is the external potential, the second term is the positron-electron correlation potential and the third term is the Coulombic potential caused by the electrons. The potential V_{eff} is used in one-particle Schrödinger equation (2.6) for calculation of positron wave-function and energy eigenvalues. To solve equations (2.6)-(2.7) it is necessary to estimate the exchange-correlation term. This is performed within the local density approximation (LDA), i.e. assuming that electron-positron correlation depends only on the electron density at the positron site. In the ATSUP code LDA approach is implemented using the parametrization of the exchage-correlation potential and the enhancement factor $\gamma(r)$ in equation (1.2) proposed by Boroński and Nieminen [9]. The LDA approach was proved to give accurate positron lifetimes especially in metals when superimposed electron density is used in equations (2.6)-(2.7) [10]. For this reason the LDA scheme was used also in this work.

Hence, in ATSUP code the electron density and Coulomb potential are constructed by superposition of atomic densities and potentials

$$n(\mathbf{r}) = \sum_i n_{at}(|\mathbf{r} - \mathbf{R_i}|), V_C(\mathbf{r}) = \sum_i V_{at}(|\mathbf{r} - \mathbf{R_i}|). \tag{2.11}$$

where R_i runs over the occupied atomic sites, n_{at} and V_{at} are the atomic electron density and Coulomb potential, respectively.

The values of the potential and the densities of the particles are not possible to determine in the infinite number of the lattice points. Therefore, a discrete 3D mesh is used in the calculations and the Schrödinger equation for the positron is solved in every point of this mesh. The results are the eigenvalues of the positron energy ϵ_i^+ and the wavefunctions $\psi_i^+(\mathbf{r})$. Through difference between the ground

state energy of delocalized positron and positron trapped at defect one can find out the binding energy of the positron to the defect and the positron ground state wavefunction $\psi^+(\mathbf{r})$ clarifies the characteristics of the annihilation, e.g. the fraction of the annihilations with the electrons of different types of atoms. The position annihilation rate is determined by equations (1.2) with the calculated electron and positron densities.

2.4 Calculations by ATSUP code

In the ATSUP code the the Schrödinger equation of the positron is solved numerically in a 3D grid in real space. The seek for the positron wavefunction is realized by the minimalization of the functional itteratively by the conjuged gradient method [11]. The important input and output data will be discussed in this section. The INPUT file is shown in the Appendix A for better imagination of the calculations setup.

Iron and aluminum atoms were positioned into their sites in the supercell containing 1024 atoms. The supercell was periodically repeated in calculations. The atom coordinates are inserted as a parameter into the *POSITION* field in the INPUT file.

The boundary condition is set in the input file of the program. The setting 111 means that the value of the wavefunction is periodically repeated on the borders of the supercell. This setting must be used in the calculations for the non-defected material. For the vanishing boundary condition the value of the parameter *BOUNDARY* is set to 000, which means that positron wavefunction is zero at the borders of the supercell. This setting is used in the calculations of the annihilation of the positron trapped at defects.

Chapter 3

Results of the measurements

3.1 Samples of Fe-Al alloys

The Fe-Al alloys of various composition were studied in this work. Samples were prepared from 99.99% iron and 99.99% aluminium by induction and arc melting (Edmund Buehler furnace) in Ar gas protective atmosphere gathered by Ti. All the samples were repeatedly melted at least four times to guarantee mixing of the atoms and prevent the clustering of pure elements. The obtained ingots were cut to desired profiles by the rotation saw. The composition of samples in this work is noted as atomic fractions. All samples were annealed at 1000 °C for one hour in the silicone glass ampoule evacuated to vacuum of 10^{-3} mbar and subsequently quenched by immersing the ampoule into water of room temperature. After characterization of as-quenched state some samples were subjected to isochronnal annealing performed in steps 40 °C / 40 min. The samples were annealed on air wrapped in a steel foil. Temperature in the furnace was stabilized within ± 1 °C. Each annealing step was finished by quenching into silicon oil of room temperature.

The equilibrium phase diagram of the Fe-Al alloys was firstly proposed by Kubaschewski [12] and subsequently extended to present form in the Figure 3.

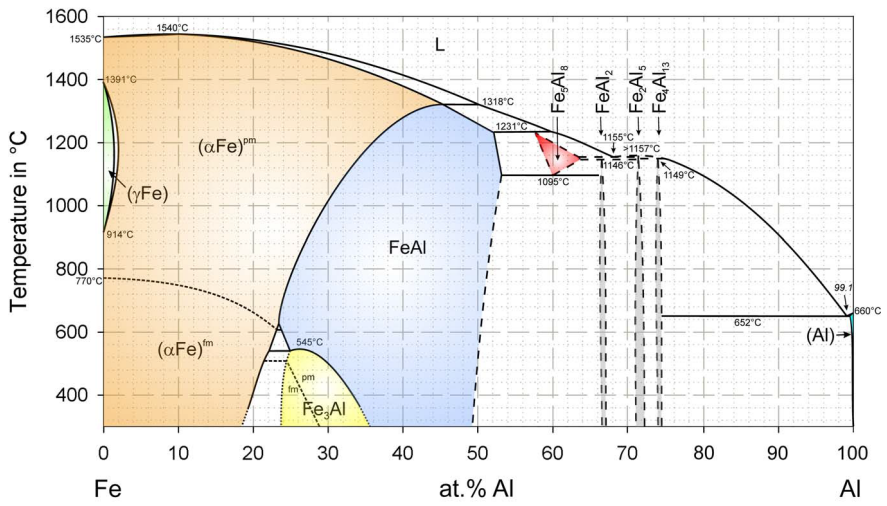

Figure 3: Equilibrium phase diagram of Fe-Al binary system [12].

The structure of the iron-aluminium alloys in the interval 0 - 50 at. % Al can be described by a body centered cubic (BCC) lattice which constists of two simple cubic (SC) sublattices. The A-sublattice is displaced with respect to the B-sublattice by the vector $[a/2, a/2, a/2]$ where a is the lattice parameter of the BCC lattice. Three phases may form in the studied samples. The A2 phase is derived from the $\alpha-$iron and represents disordered solid solution of Al in Fe, where both sublattices are randomly occupied by the Fe and Al atoms. The B2 structure consisting of the A-sublattice occupied exclusively by Fe atoms and the B-sublattice occupied by Al atoms is the equilibrium phase for the stoichiometric $Fe_{50}Al_{50}$ composition. In case of non-stochiometric composition the B2 phase is obtained by random occupation of the B-sublattice by both Al and Fe atoms. Alloys with compositions near the $Fe_{75}Al_{25}$ may form stable ordered phase $D0_3$ which is characterized by the Fe atoms in the A-sublattice while the B-sublattice consists of alternating Fe and Al atoms.

3.2 X-ray diffraction measurement

X-ray diffraction (XRD) measurements were performed on the diffractometer X´Pert-MRD (Panalytical) in the symmetric Bragg-Brentano geometry. Fe-Al alloys exhibit relatively large millimeter size grains. Therefore, orientation of crystallographic planes is not random like in powder samples because only very limited number of grains contribute to the diffraction pattern. For these reasons for samples $Fe_{75}Al_{25}$ and $Fe_{60.46}Al_{39.54}$ the classical $\theta - 2\theta$ scan was supported by the rotation around the axis normal to the surface, so-called ω scan.

Fe-Al alloys with composition were $Fe_{75}Al_{25}$ (i.e. stoichiometric Fe_3Al composition), $Fe_{60.46}Al_{39.54}$ and $Fe_{55.38}Al_{44.62}$ were investigated by XRD. Firstly, samples were quenched from 1000 °C. Secondly, samples were subjected to the same thermal treatment as quenched samples, but moreover after quenching were isochronally annealed in steps 40°C/40 min from 200 up to 520°C, except for $Fe_{55.38}Al_{44.62}$ which was annealed up to 600 °C.

The measured diffraction patterns from XRD measurements are plotted in Figures 4-8. Samples $Fe_{75}Al_{25}$ and $Fe_{60.46}Al_{39.54}$ were measured using Cu anode with wavelength $\lambda_{Cu-K\alpha 1} = 1.54056$Å, while $Fe_{55.38}Al_{44.62}$ using Co anode with wavelength $\lambda_{Cu-K\alpha 1} = 1.79026$Å, therefore scattering angles in the Figure 8 differs from the others. The diffraction lines calculated by the Carine Crystallography code for perfect A2, $D0_3$ and B2 structures of appropriate composition are shown in the figures as well. The intensity of calculated peaks is also illustrated by the height of diffraction pattern. The relative heights of the calculated peaks do not correspond to the modeled intensities because of the texture in the sample which also influences the intensity of diffraction peaks.

The small peaks denoted by the symbol Cu-K_β are caused by the K_β line present in the Cu anode spectrum which is not entirely suppressed by the beta-filter foil. The peaks denoted W-K_α represent reflections of $K_{\alpha 1}$ and $K_{\alpha 2}$ X-ray created by electrons which hit the tungsten holder of Cu anode.

The A2 structure is formed by the random occupancies of atoms on the A and B-sublattices. It means its structure factor is composed from the average of the iron and aluminium atomic form factors. The A2 phase has BCC structure characterized by extinction of the the reflections which fulfill the condition $h + k + l = 2n + 1$; only the cubic reflections with the even sum are visible in the data. The random distribution causes that the atom form factor is the mean value of the Fe and Al atom form factors. The rules for the structure factor F are

$$F = \begin{cases} < f(Fe) + f(Al) > & \text{if } h + k + l = 2n \\ 0 & \text{if } h + k + l = 2n + 1. \end{cases}$$

In the B2 structure the A-sublattice is occupied exclusively by Fe atoms, while sites in the B-sublattice may be randomly occupied by Al or Fe atoms depending on the composition. For example in stoichiometric $Fe_{75}Al_{25}$ composition site on the B-sublattice are occupied with Fe and Al atoms with equal probability. On the other hand, in stoichiometric $Fe_{50}Al_{50}$ alloy the B sites are occupied only by Al atoms. For the ordered B2 structure corresponding to $Fe_{50}Al_{50}$ stoichiometry more reflections are observed, these are called super-lattice reflections and are caused by the long range order (LRO). In case of ideal B2 all the diffractions are visible because the structure factor (1.30) depends on the h, k, l like

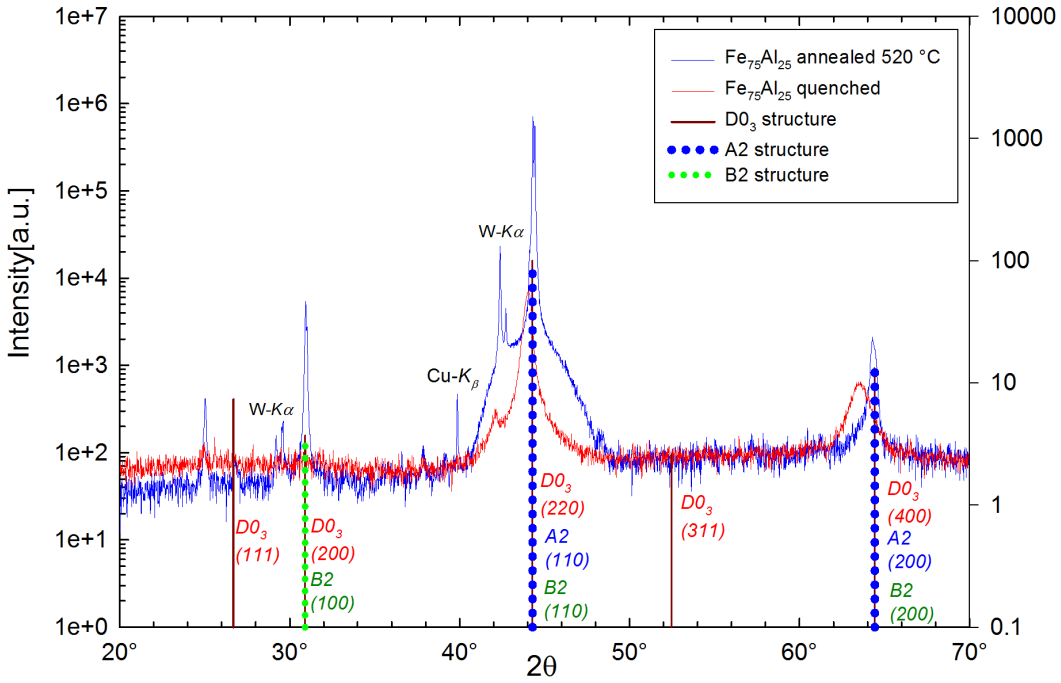

Figure 4: The recorded powder diffraction pattern of the samples $Fe_{75}Al_{25}$, low diffraction angles, Cu anode.

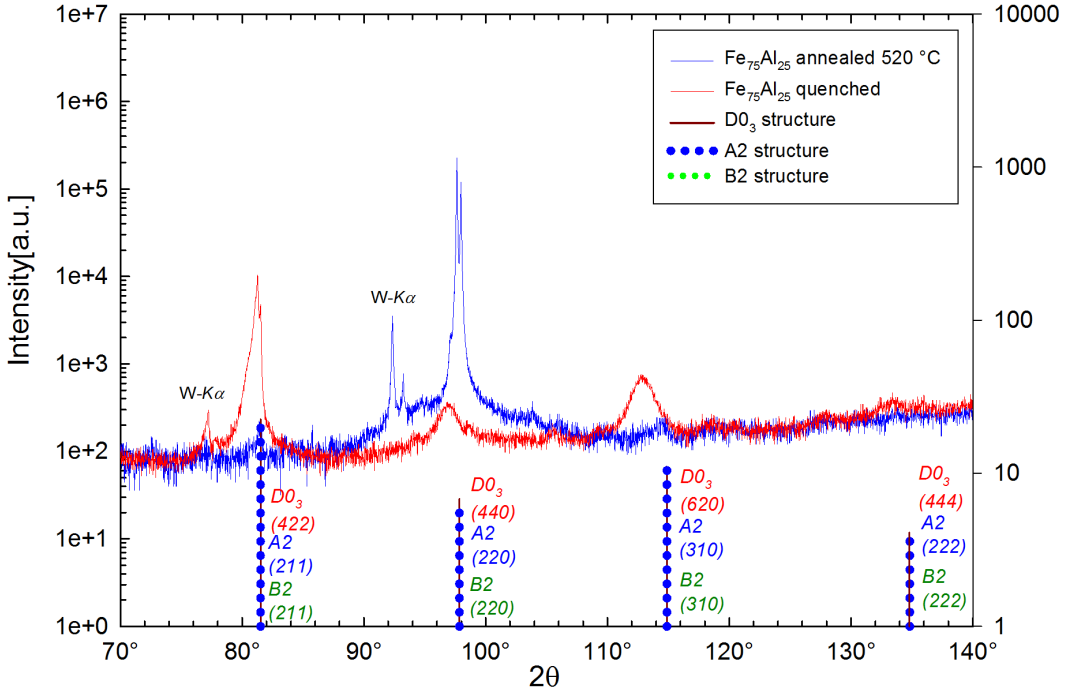

Figure 5: The recorded powder diffraction pattern of the samples $Fe_{75}Al_{25}$, high diffraction angles, Cu anode.

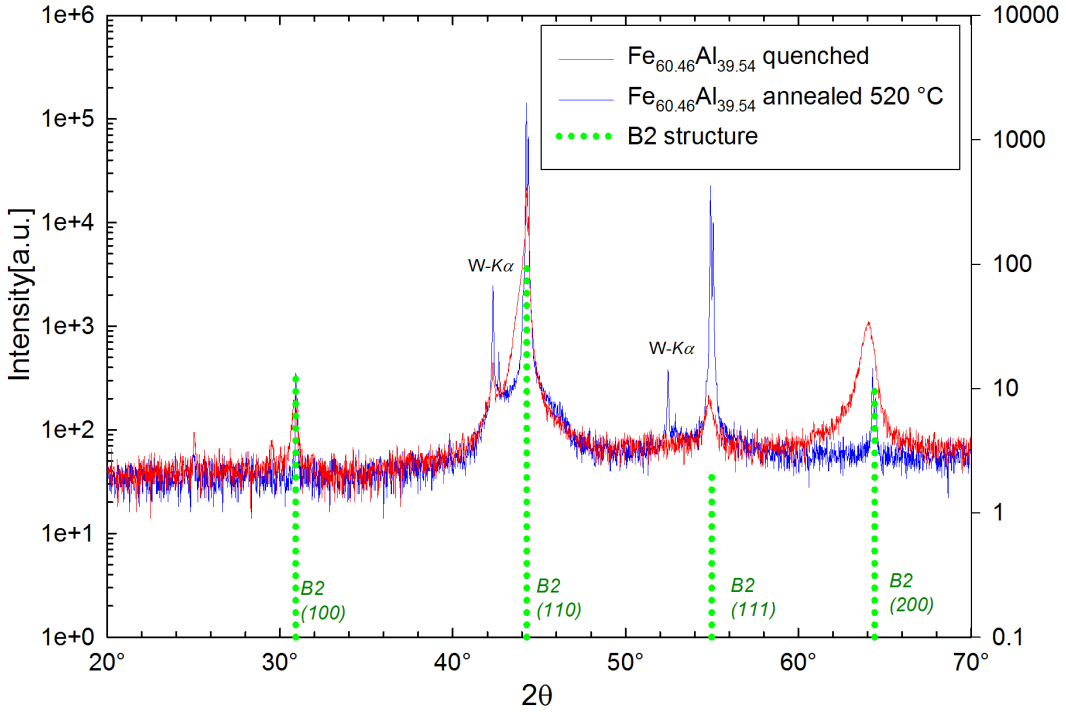

Figure 6: The recorded powder diffraction pattern of the samples $Fe_{60.46}Al_{39.54}$, low diffraction angles, Cu anode.

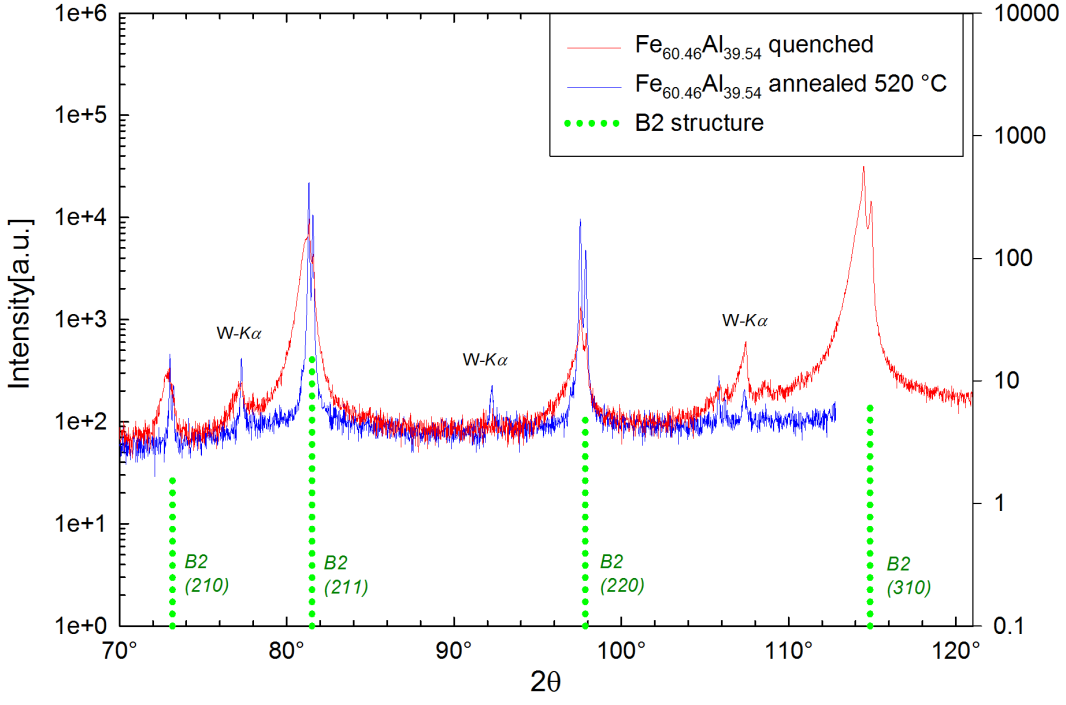

Figure 7: The recorded powder diffraction pattern of the samples $Fe_{60.46}Al_{39.54}$, high diffraction angles, Cu anode.

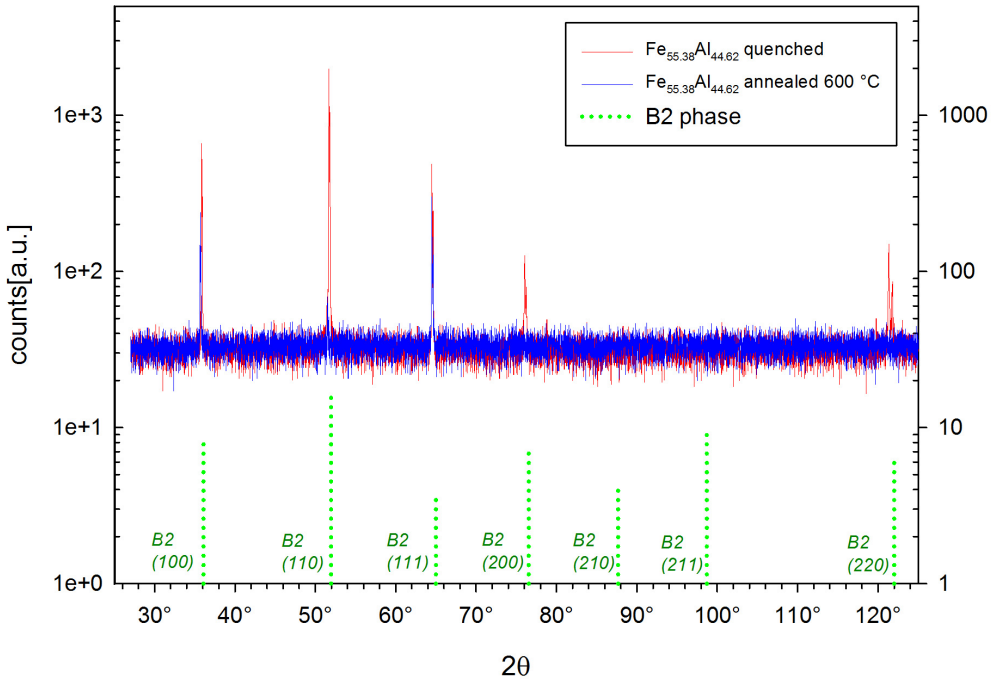

Figure 8: The recorded powder diffraction pattern of the samples $Fe_{55.38}Al_{44.62}$, Co anode.

$$F = \begin{cases} f(Fe) + f(Al) & \text{if } h+k+l = 2n \\ f(Fe) - f(Al) & \text{if } h+k+l = 2n+1 \end{cases}$$

For B2 structure with short range order (SRO), i.e. with B-sublattice sites filled randomly by Fe and A atoms the intensity of super-lattice reflections is lower.

The $D0_3$ structure consists of the ordered alternating Al and Fe atoms on the B-sublattice and Fe atoms on the A-sublattice. It means $D0_3$ unit cell is twice that of the BCC B2 cell and the Miller indices corresponding to the same planes are twice those for the B2 phase. This unit cell can be decomposed to the four interpenetrating face centered cubic (FCC) sublattices. New super-lattice reflections can appear in diffraction pattern of $D0_3$ structure. Diffraction pattern of $D0_3$ phase contains a complete set of reflections of the A2 phase, but in addition to that it contains also (111) and (200) super-reflections caused by long range ordering in the $D0_3$ phase. Since only the $D0_3$ structure yields a low-angle (111)-super-lattice reflection, the long-range ordered structures B2 and $D0_3$ can be distinguished from each other.

In ordered alloys there is a possibility to form regions with the same structure and symmetry but with a displacement of the unit cells. These regions are called antiphase domains and boundaries between them are called antiphase boundaries (APB). APB is the two dimensional defect with the energy corresponding to the stacking fault. In the Fe-Al alloys with B2 structure only APBs with displacement vector $a_0/4 < 111 >$ may be formed. Here a_0 is the lattice parameter of the B2 cell shown in Figure 9 taken from [13]. The Fe-Al alloys close to $Fe_{75}Al_{25}$ with $D0_3$ structure has two possible APBs with displacement $a_0'/4 < 111 >$ and $a_0'/2 < 100 >$. Here a_0' is the lattice parameter of the $D0_3$ unit cell shown in Figure 9.

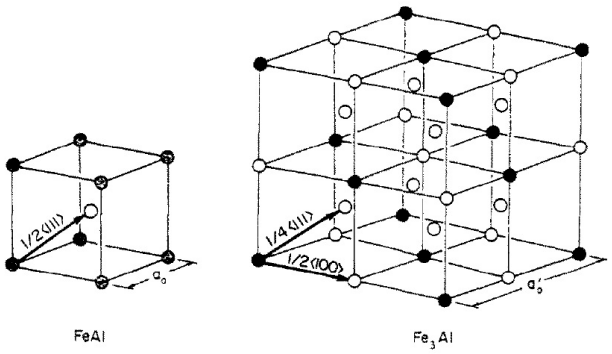

Figure 9: Atomic arrangements and possible superlattice displacement vectors for the ordered FeAl B2 structure and Fe_3Al $D0_3$ [13]. White circles represent Fe atoms and black circles Al atoms.

Table I shows lattice parameters obtained from the linear regression of the Cohen-Wagner plot in Figure 10 using the relation (1.33). The second column shows the lattice parameter a_{exp} of the BCC A2/B2 cell, while the third column shows the lattice parameter a'_{exp} of the $D0_3$ cell. Since $a'_{exp} = 2a_{exp}$ Table I shows also $2a_{exp}$ for the A2 and B2 phase and $a'_{exp}/2$ for the $D0_3$ phase for the sake of comparison. The error of the lattice parameters in Table I is the error of the parameter of the linear regression of the Cohen-Wagner plot.

Table I: The lattice parameters of the Fe-Al alloys measured by XRD. Lattice parameter a_{exp} is for B2 lattice and a'_{exp} for $D0_3$ superlattice obtained from linear regression of Cohen-Wagner plot in Figure 10.

Sample	Treatment	a_{exp}[Å]	a'_{exp}[Å]	Structure
$Fe_{75}Al_{25}$	Quench 1000°C	2.918(11)	5.836(22)	A2
$Fe_{75}Al_{25}$	Anneal. 520°C	2.900(2)	5.799(5)	$D0_3$
$Fe_{60.46}Al_{39.54}$	Quench 1000°C	2.899(3)	5.799(7)	B2
$Fe_{60.46}Al_{39.54}$	Anneal. 520°C	2.897(1)	5.794(2)	B2
$Fe_{55.38}Al_{44.62}$	Quench 1000°C	2.904(1)	5.808(3)	B2
$Fe_{55.38}Al_{44.62}$	Anneal. 600°C	2.896(3)	5.791(5)	B2

Figure 4 shows that the (100) reflection is not present in the XRD diffraction pattern of quenched $Fe_{75}Al_{25}$ although the reflection (200) is visible. According to shown calculated reflections this is possible only in the case of A2 structure, which prove that the as-quenched $Fe_{75}Al_{25}$ sample exhibits A2 phase. Hence, the peak broadening in this sample is caused by atomic disorder in the A2 phase. Subsequent ordering into LRO $D0_3$ structure in the annealed sample leads to narrowing of diffraction profiles. Closer look at the peaks in 4 - 7 revealed the broadening of diffraction peaks in quenched alloys which disappeared in samples annealed up to 520 °C. Note that no mechanical treatment was applied on samples, therefore, one can exclude broadening caused by dislocation-induced microstrains, which is in addition symmetrical. But one can see in Figures 6,7 that peak broadening in quenched $Fe_{60.46}Al_{39.54}$ sample is asymmetrical and XRD profiles have a long tail on the left side, i.e. at lower diffraction angles corresponding to larger interplannar distances. This asymmetry can be clearly seen in Figures 11(a) and 11(b)

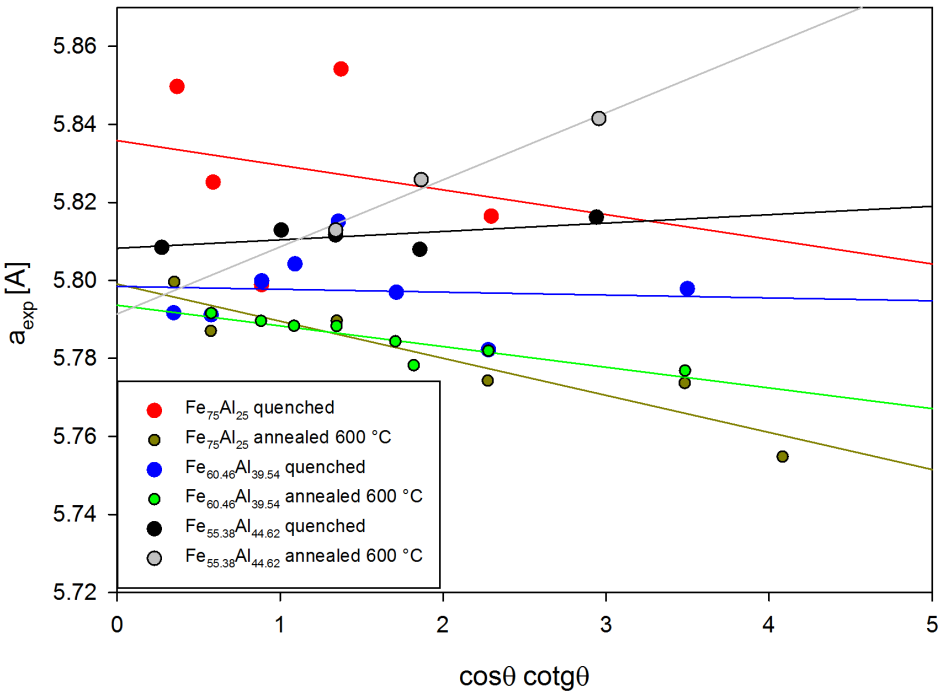

Figure 10: Cohen-Wagner plot of the alloys measured by XRD

which show (210) and (220) reflections measured in the as-quenched $Fe_{60.46}Al_{39.54}$ alloy.

According to the equilibrium phase diagram (see Figure 3) the $Fe_{60.46}Al_{39.54}$ alloy is a single phase system containing only the B2 phase. One can see in Figures 11(a) and 11(b) that XRD profiles in as-quenched $Fe_{60.46}Al_{39.54}$ sample cannot be fitted by a single XRD reflection. Inspection of the Figures revealed that XRD profiles in as-quenched $Fe_{60.46}Al_{39.54}$ alloy are composed from a sharp reflection with dominating intensity overlapped with a broader low-intensity reflection shifted to slightly lower diffraction angles. A plausible explanation is that the sharp intense peaks come from the perfect B2 phase while the small broad peak shifted to lower diffraction angles is diffuse scattering from point defects. PAS investigations discussed in the following text gave a clear evidence that as-quenched $Fe_{60.46}Al_{39.54}$ alloy contains a high concentration of di-vacancies surrounded by Al atoms. This is in agreement with theoretical ab-initio calculations [14] which revealed attractive interaction between Al atoms dissolved in Fe and vacancies resulting to predicted formation of vacancies surrounded by Al in Fe-Al alloys. Hence, small broad peaks observed in the as-quenched $Fe_{60.46}Al_{39.54}$ alloy can be attributed to diffuse scattering from Al clusters surrounding vacancies. This picture is further supported by the fact that an increase in Al concentration leads to an increase in the lattice parameter. As a consequence the broad peak originating from diffuse scattering from B2 lattice containing Al clusters surrounding vacancies are shifted to lower diffraction angles. Figures 12(a) and (b) show (211) and (220) reflections in as-quenched $Fe_{60.46}Al_{39.54}$ alloy decomposed into two contributions: (i) a sharp reflection from perfect B2 lattice and (ii) a broad diffuse scattering peak at lower diffraction angles caused by Al clusters surrounding vacancies. One

can see in Figures 12(a), (b) that this model describes satisfactorily the shape of the XRD reflection profiles in quenched $Fe_{60.46}Al_{39.54}$ alloy. The lattice parameter corresponding to B2 lattice containing clusters of di-vacancies surrounded by Al atoms determined by fitting of XRD spectra of the as-quenched $Fe_{60.46}Al_{39.54}$ alloy is 2.907(5). It means the relative lattice expansion caused by Al clusters surrounding divacancies is approximately 0.3%.

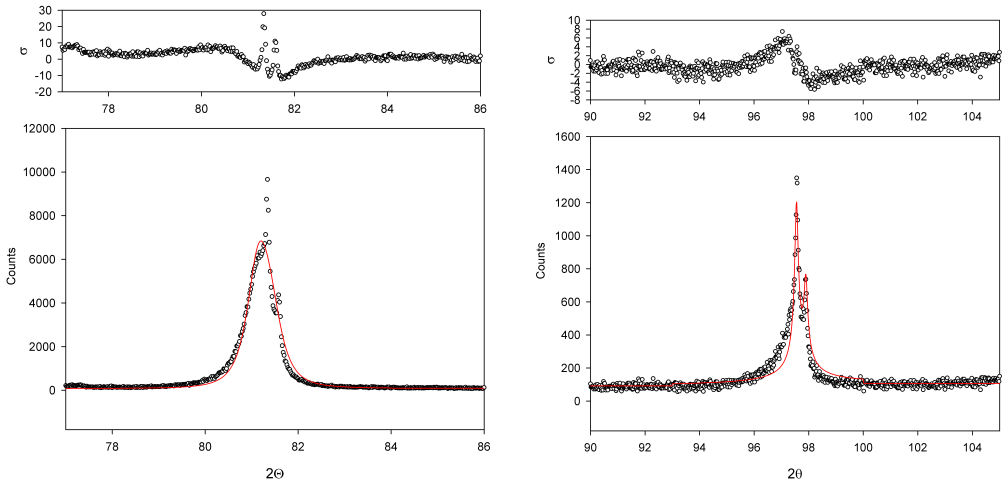

(a) peak (211) (b) peak (220)

Figure 11: Fit of XRD profiles and residuals (σ) in as-quenched $Fe_{60.46}Al_{39.54}$ spectra showing the asymmetry of peaks.

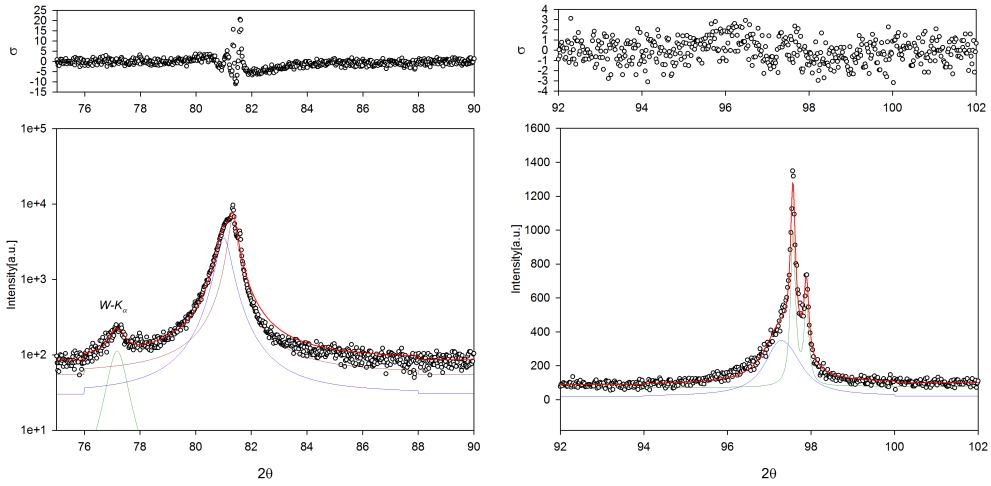

(a) peak (211) (b) peak (220)

Figure 12: Fit of XRD profiles and residuals (σ) in as-quenched $Fe_{60.46}Al_{39.54}$ spectra showing the asymmetry of peaks.

Annealing at 520 °C causes a substantial recovery of quenched-in vacancies. This leads also to decomposition of Al clusters due to repulsive Al-Al interaction. As a consequence the broad peaks from diffuse scattering were not observed in

XRD spectrum of annealed $Fe_{60.46}Al_{39.54}$ alloy and only sharp reflections from perfect B2 phase remained.

3.3 Microhardness

In this work was measured microhardness of Fe-Al alloys quenched from 1000 °C and subsequently subjected to isochronal annealing with heating steps 40 °C / 40 min. Each heating step was finished by quenching to room temperature. The obtained results, i.e. the dependence of microhardness HV0.1 on the annealing temperature, are shown in the Figure 13. Two points plotted by open triangles correspond to samples quenched from 1000 °C and subsequently annealed at 550 °C for 1h and quenched down to room temperature shown to demonstrate the effect of different thermal history of samples.

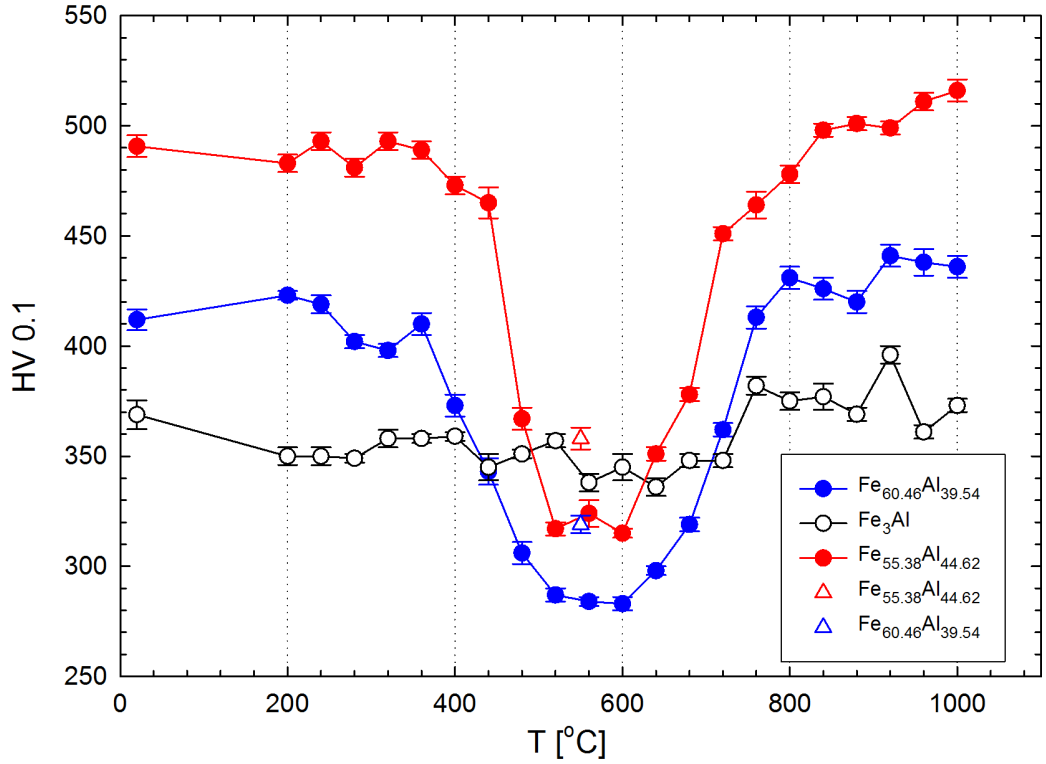

Figure 13: Microhardness of Fe-Al alloys quenched from 1000 °C and subsequently subjected to isochronal annealing with annealing steps 40 °C / 40 min (circles), samples quenched from 1000 °C and subsequently annealed at 550 °C for 1h and again quenched to room temperature (open triangles).

Comparison of microhardness of alloys quenched from 1000 °C revealed strong dependence on aluminium content. Samples with higher aluminium content exhibit higher microhardness. This effect could be explained by solution hardening. Dissolved Al atoms may act as obstacles for movement of dislocations. However subsequent thermal treatment can not be explained only by solution hardening effect due to varying concentration of dissolved Al atoms. Another mechanism of hardening must be considered. It was proposed that microhardness of Fe-Al alloys is influenced by the vacancy concentration [15]. The rapid quenching from

1000 °C guarantee high concentration of quenched-in thermal vacancies. Vacancies are also obstacles for dislocation movement and their concentration increases with increasing Al content [15]. Migration of vacancies is thermally activated process. In samples annealed above 400 °C vacancies become mobile and disappear by diffusion into sinks at grain boundaries and surface. As a consequence, hardness of $Fe_{60.46}Al_{39.54}$ and $Fe_{55.38}Al_{44.62}$ alloys strongly decreases above 400 °C and reaches its minimum at ∼560 °C.

When considering temperature dependence of microhardness the stoichiometric $Fe_{75}Al_{25}$ alloy differs from FeAl-based alloys $Fe_{60.46}Al_{39.54}$ and $Fe_{55.38}Al_{44.62}$. Microhardness of $Fe_{75}Al_{25}$ does not decrease and shows only a slight increase at high temperatures above 700 °C. The reason for such behavior can be found when concentration of quenched-in vacancies in various alloys is considered. The concentration of quenched-in vacancies was determined by slow positron implantation spectroscopy (SPIS) and is listed in Table II. Since on the contrary to the other two alloys with higher Al content the concentration of vacancies in $Fe_{75}Al_{25}$ sample is relatively low, hardness of this alloy is almost insensitive to variations in vacancy concentration. The effect of vacancies on hardness becomes significant only at higher concentration of vacancies.

X-ray measurements revealed that $Fe_{75}Al_{25}$ sample quenched from 1000 °C exhibits predominantly the A2 disordered phase. Annealing at temperatures around 400 °C should enhance diffusion which enables ordering into the equilibrium $D0_3$ phase. Subsequently above 545 °C the $D0_3$ phase is transferred into partially ordered B2 phase. No signs of steep change in microhardness connected with these phase transitions are visible in $Fe_{75}Al_{25}$ alloy in Figure 3. Therefore, the microhardness of $Fe_{75}Al_{25}$ exhibits only moderate changes with temperature on the contrary to hardness of Fe-Al based alloys which is strongly influenced by vacancy hardening.

Table II: Concentration of vacancies c_v determined by SPIS.

Sample	c_V[at.$^{-1}$]
$Fe_{55.38}Al_{44.62}$	$5.0(5) \times 10^{-2}$
$Fe_{60.46}Al_{39.54}$	$4.8(6) \times 10^{-4}$
$Fe_{75}Al_{25}$	$7.0(8) \times 10^{-5}$

Microhardness HV0.1 measured on Fe-Al alloys of various composition is plotted in Figure 14 as a function of Al content. The samples quenched from 1000 °C are compared with samples quenched from 1000 °C and subsequently annealed at 520 °C for 1 hour and quenched to room temperature.

One can see in Figure 14 that microhardness of samples quenched from 1000 °C strongly increases with Al content. For alloys with Al content up to 25% subsequent annealing of samples at 520 °C does not cause any significant change in microhardness. On the other hand, annealing at 520 °C leads to a substantial decrease of microhardness in alloys with Al content of 39% and higher. Alloys with low Al content (up to 26%) exhibit low concentration of vacancies, see Section 3.4, therefore, hardness of these alloys is influenced predominantly by the solute hardening, while effect of vacancies is negligible here. Because of this reason the annealing at 520 °C which removes vacancies has basically no influence on hardness. On the other hand, the effect of vacancy hardening is substantial in alloys

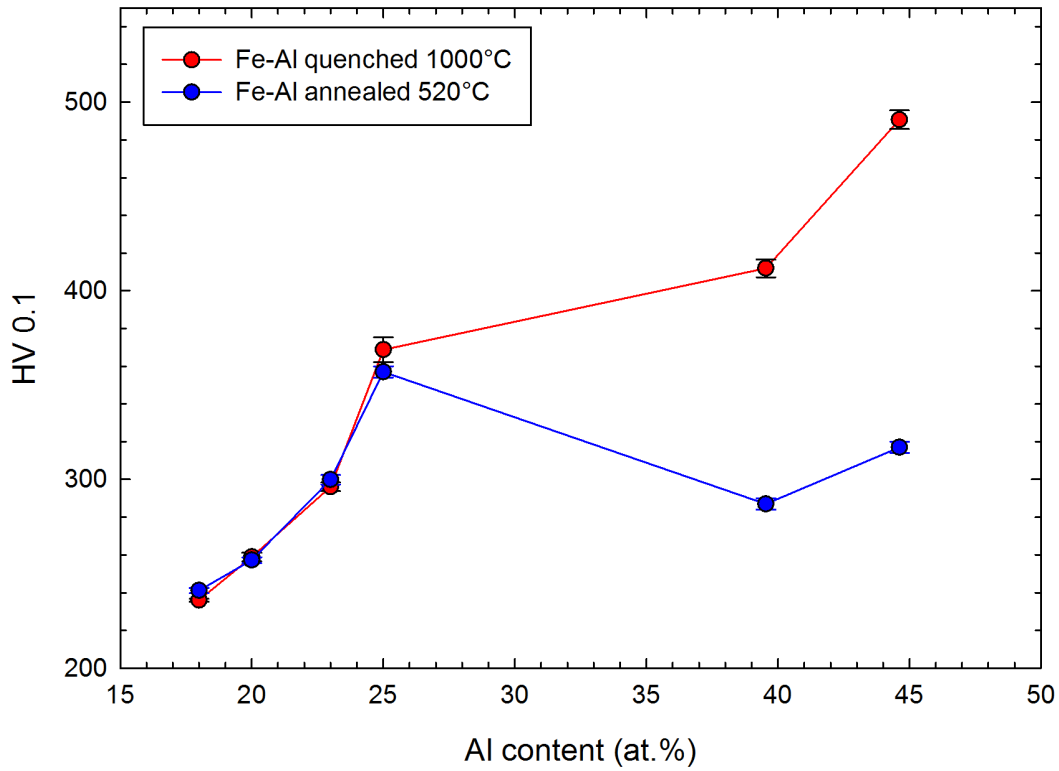

Figure 14: Microhardness of Fe-Al alloys vs. Al content. Alloys quenched from 1000 °C (red points); alloys quenched from 1000 °C, subsequently annealed at 520 °C for 1 h and quenched again to room temperature (blue points).

with high Al content (39% or higher). Hence, annealing at 520 °C, which causes a significant decrease in concentration of vacancies, leads also to a significant decrease of hardness. Hence, one can conclude that the effect of vacancy hardening on microhardness becomes significant when concentration of vacancies exceeds $10^{-4}\mathrm{at}^{-1}$.

3.4 Positron annihilation spectroscopy results

3.4.1 Positron Lifetime

Positron lifetime spectra were measured by high resolution digital spectrometer described in [2, 3] equipped with two Hamamatsu H3378 photomultipliers coupled with BaF_2 scintillators. Detector pulses are sampled in real time by two ultra-fast 8-bit digitizers Acqiris DC211 with a sampling frequency of 4 GHz. The digitized pulses are acquired in a PC and worked out off-line by a software using a new algorithm for integral constant fraction timing [16]. The time resolution of the digital LT spectrometer was 150 ps (FWHM, ^{22}Na). At least 10^7 annihilation events were accumulated in each LT spectrum.

Positron lifetime spectra were fitted by the code written in FORTRAN using fitting library MINUIT [17]. The maximum likelihood method is used to estimate parameters in equation (1.5). Various number of components are possible to fit to measured data. The quality of the fit is quantified by the standard χ^2 test, in ideal case χ^2 per number of degrees of freedom equals 1.

The ^{22}Na positron source with activity of 1.5 MBq was deposited in the from of Na_2CO_3 on 2 μm thick Mylar foil. In PAS measurement positron source was always sandwiched between two identical specimens. Hence, there is necessarily a contribution of positrons annihilated in the source. In our case the source contribution consists of two components: (i) shorter component with lifetime of 368 ps and intensity of ~ 8 % representing a contribution of positrons annihilated in the Na_2CO_3 source spot, and (ii) long-lived component with lifetime ~ 1.5 ns and intensity of ~ 1 % which comes from ortho-positronium formed in the covering mylar foil. The lifetime of the shorter source component was fixed in fitting at the value 368 ps determined in measurements on reference well annealed Fe sample. Intensity of this component depends on the Z value of the measured sample. Therefore, it was fitted as a free parameter. Nevertheless, in all measured samples intensity of the shorter source component was found to be in a reasonable agreement with the value determined on reference well-annealed Fe sample and corrected to different Z using the formula described in [18]. The lifetime and intensity of the long-lived source component were fitted as free parameters because this component is well separated from the other components in positron lifetime spectra and correlation of its lifetime and intensity with other parameters is low.

From three to five components were fitted in the spectra including the two source components. Intensities of physically interesting components coming from the positrons annihilating in the sample were subsequently renormalized to 100%.

3.4.2 Coincidence Doppler Broadening

The CDB spectrometer consists of two HPGe detectors and commercial NIM modules operated by a PC. The overall energy resolution of the spectrometer was 1.0 keV (FWHM) at energy of 511 keV. At least 10^8 events were gathered in each two-dimensional spectrum, which was subsequently reduced into one-dimensional Doppler profile and instrumental resolution cuts. The relative changes of Doppler profiles were followed as ratio curves of the Doppler profile normalized counts to those of the well annealed α-Fe reference profile. The CDB profiles are symmetrical with respect to the origin and only the parts corresponding to positive

Doppler shifts are shown.

Figure 15 shows two dimensional CDB spectrum, i.e. sum of energies of annihilation photons plotted versus difference of these energies, measured on $Fe_{75}Al_{25}$ alloy quenched from 1000 °C. The vertical cut of the CDB spectrum for values which fulfill $E_1 - E_2 = 0$ is used to obtain the resolution function of the spectrometer. The horizontal cut at $E_1 + E_2 = 2 \times 511$ keV gives Doppler broadened annihilation profile, i.e. one-dimensional momentum distribution of electrons which annihilated positrons convoluted with the resolution function. Both horizontal and vertical cuts from Figure 15 are plotted in Figure 16.

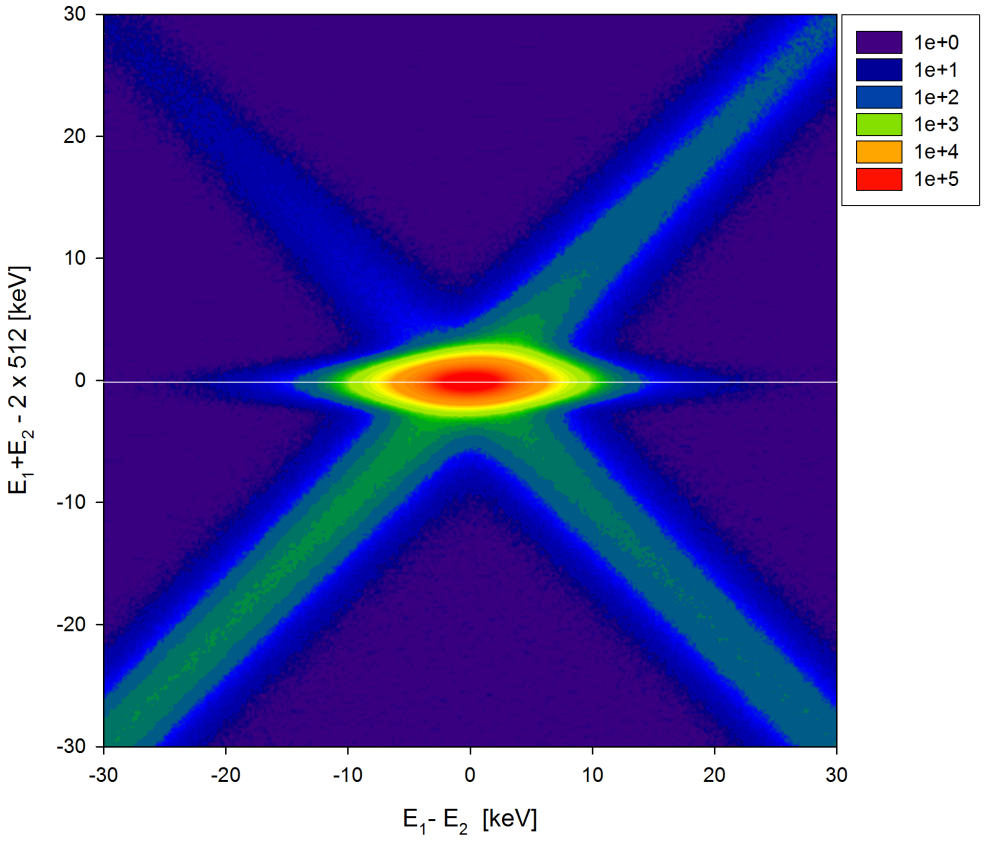

Figure 15: Two dimensional CDB spectrum of $Fe_{73}Al_{27}$ alloy quenched from 1000 °C.

3.4.3 Quenched Fe-Al alloys of various compositions

Samples of Fe-Al alloys samples with various compositions were prepared by quenching from 1000 °C as described in Section 3.1.

The results obtained from fitting of positron lifetime spectra are listed in Table III. The shorter component with lifetime τ_1 and intensity I_1 represents a contribution of free positrons while the longer component with lifetime τ_2 and intensity I_2 can be attributed to positrons trapped in quenched-in vacancies. Dependence of the lifetime τ_2 and the intensity I_2, respectively, on Al content is plotted in Figures 17(a),(b). The intensity of positrons trapped in vacancies and positron

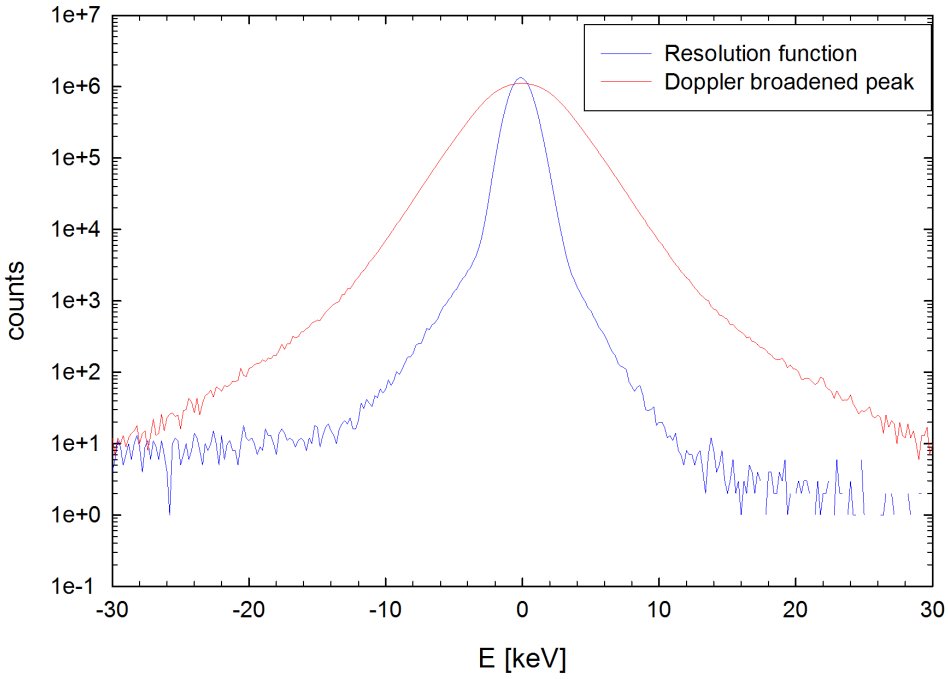

Figure 16: Horizontal and vertical cuts of two dimensional CDB spectra of $Fe_{73}Al_{27}$ alloy quenched from 1000 °C represent Dopppler broadening peak profile and resolution function of CDB spectrometer, respectively.

lifetime of this component clearly increase with increasing Al content. For samples with Al content $c_{Al} \geq 26\%$ the intensity of trapped positrons I_2 reaches 100%, i.e. concentration of vacancies is so high that virtually all positrons annihilate from the trapped state (saturated positron trapping). The quantity τ_f was calculated using equation (1.19). The positron trapping rate at a vacancy K_v was calculated using equation (1.17) where τ_f was used as the bulk positron lifetime. Subsequently the concentration of vacancies was calculated using equation (1.16) assuming the specific positron trapping rate $\nu_v = 4 \times 10^{14}$ s^{-1} determined for vacancies in Fe_3Al in [19]. The fraction of positrons annihilating at vacancies F_v was calculated using equation (1.20). The quantities K_v, c_v, F_v obtained by application of STM are listed in Table III.

The vacancy concentration c_v is plotted in Figure 18 as a function of Al content in the alloy. Vacancy concentration determined in [20] is plotted in the figure as well. The determination of vacancy concentrations by positron lifetime measurements was possible for samples $Fe_{82}Al_{18}$ - $Fe_{75}Al_{25}$. Alloys with higher Al content exhibit vacancy concentration above the limit $c_{Vmax,LT}$ given by equation (1.18), i.e. saturated positron trapping in vacancies occurs. Samples $Fe_{60.46}Al_{39.54}$ and $Fe_{55.38}Al_{44.62}$ were measured by SPIS and c_v was calculated from the obtained mean positron diffusion length using equations (1.25) and (1.23). One can clearly see in Figure 19 that concentration of quenched-in vacancies strongly increases with Al content in the alloy. If we compare $Fe_{55.38}Al_{44.62}$ and $Fe_{82}Al_{18}$ alloy (i.e. samples with the highest and the lowest Al content studied in this work), the difference in vacancy concentration is four orders of magnitude.

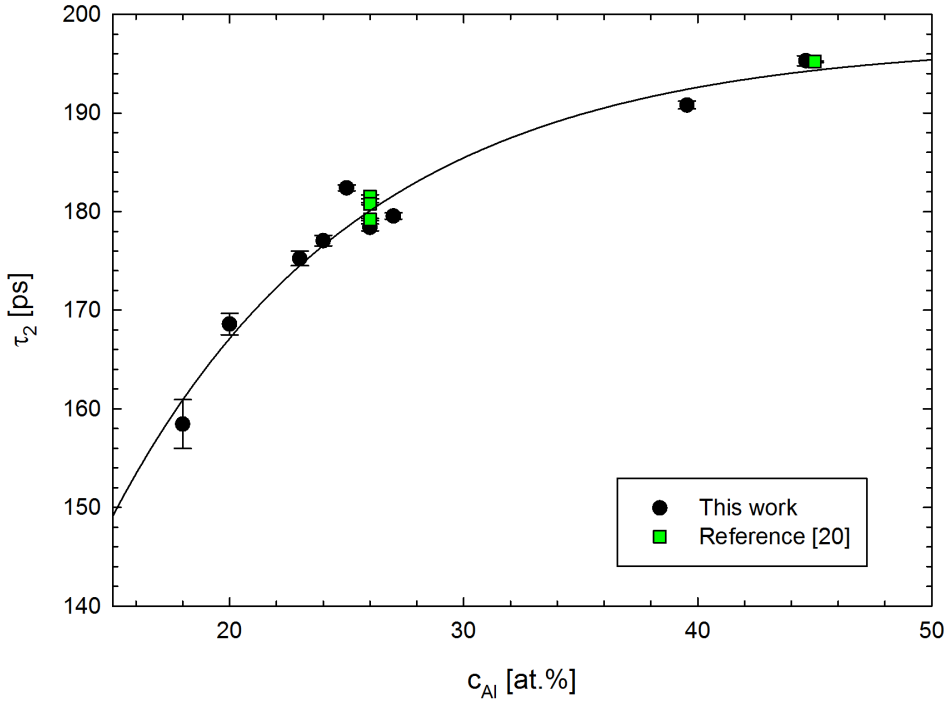

(a)

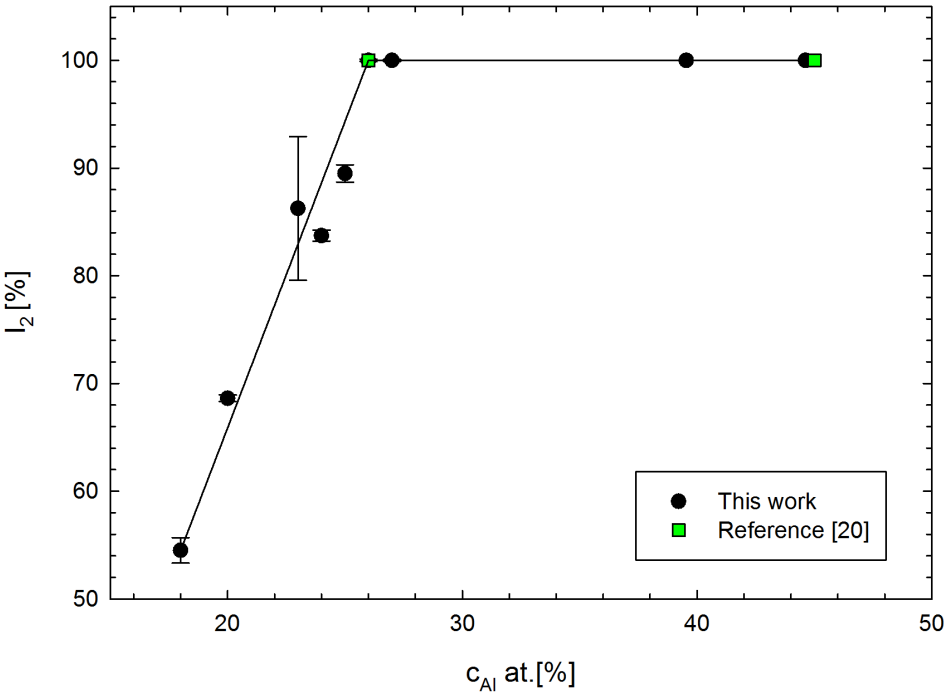

(b)

Figure 17: (a) Positron lifetime of defect component τ_2 and (b) its intensity I_2 plotted as a function of Al content of quenched Fe-Al alloys.

Table III: Results of positron lifetime measurement on Fe-Al alloys quenched from 1000 °C. Samples noted by * were measured by SPIS, see section 1.3. c_{Al} is the Al content in the alloy, τ_f is the quantity calculated using equation (1.19), K_D is the positron trapping rate to vacancies, F_v denotes the fraction of positrons annihilated from trapped state in vacancies, c_v is vacancy concentration.

c_{Al}	τ_f[ps]	$K_D[10^{-3}\mathrm{ps}^{-1}]$	F_v[%]	$c_v[10^{-6}\mathrm{at}^{-1}]$
Quenched from 1000°C				
18	107(11)	3.7(2)	28(3)	9.2(6)
20	107(2)	7.5(2)	44(2)	18.7(5)
23	102(9)	25(6)	72(3)	6(2)
24	113(2)	16(5)	65(2)	41(12)
25	114(2)	28(3)	76(2)	70(2)
26	-	-	100	>200
27	-	-	100	>200
39.54	-	-	100	480(60)*
44.62	-	-	100	$50(5)\times10^{3}$*

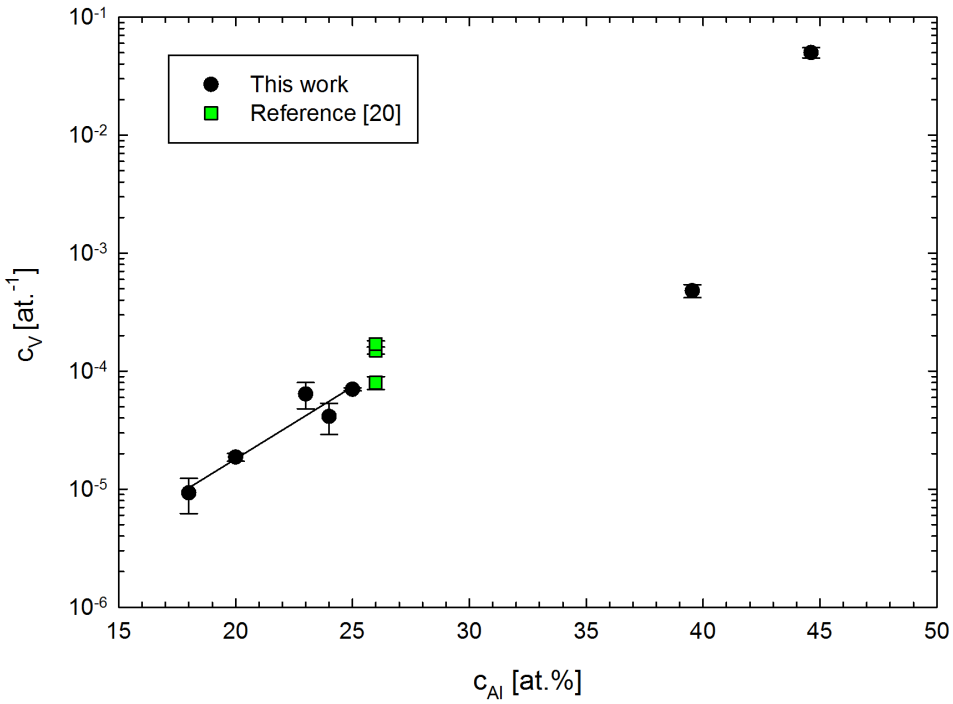

Figure 18: Vacancy concentration c_v for different Fe-Al alloys of various compositions quenched from 1000 °C.

Correlation of vacancy concentration c_v and positron lifetime τ_2 for samples quenched from 1000°C is shown in Figure 19. One can see in the figure that there is a positive correlation between lifetime of trapped positrons and concentration of quenched-in vacancies.

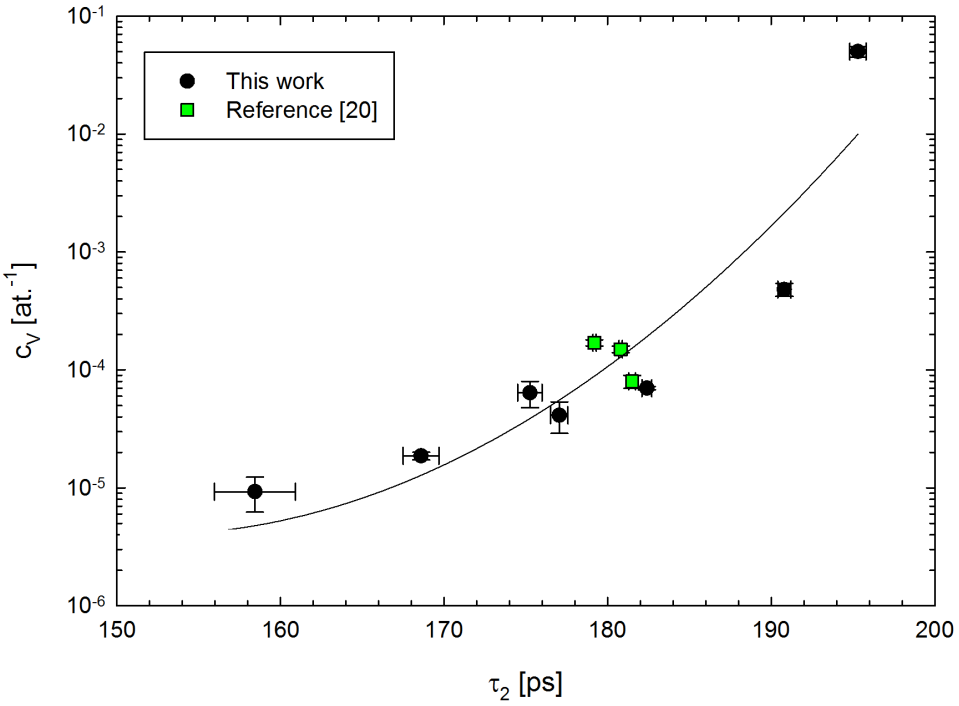

Figure 19: Vacancy concentration of Fe-Al alloys quenched from 1000 °C versus the positron defect component lifetime τ_2.

High momentum range of Doppler broadened annihilation peak measured on quenched Fe-Al alloys by CDB consists generally of four contributions:

(i) delocalized positrons annihilated by Fe electrons,

(ii) delocalized positrons annihilated by Al electrons,

(iii) positrons trapped in vacancies annihilated by Fe electrons,

(iv) positrons trapped in vacancies annihilated by Al electrons.

The momentum distribution of annihilating electron-positron pair is different for these four possibilities. To determine shape of Doppler broadened profile for these four contributions CDB measurements were performed on reference pure Fe and Al samples.

Firstly, the reference Doppler broadened profiles were measured on well annealed α-Fe (99.99%) and well annealed Al (99.999%) samples to obtain the momentum profiles $n_{Fe,B}$ and $n_{Al,B}$ for the case of annhilation of delocalized positron. The momentum distributions $n_{Fe,B}$ and $n_{Al,B}$ are plotted in Figure 20(a)

Secondly, Doppler broadened profiles $n_{Al,def}$ and $n_{Fe,def}$ were measured at deformed Al and α-Fe samples by CDB. These samples contain vacancy-like open volume defects (jogs at dislocations and vacancies anchored in the elastic field of dislocations) [21]. Therefore, Doppler broadened profile measured on cold rolled samples resembles that for positrons trapped in vacancies. In the vicinity of the

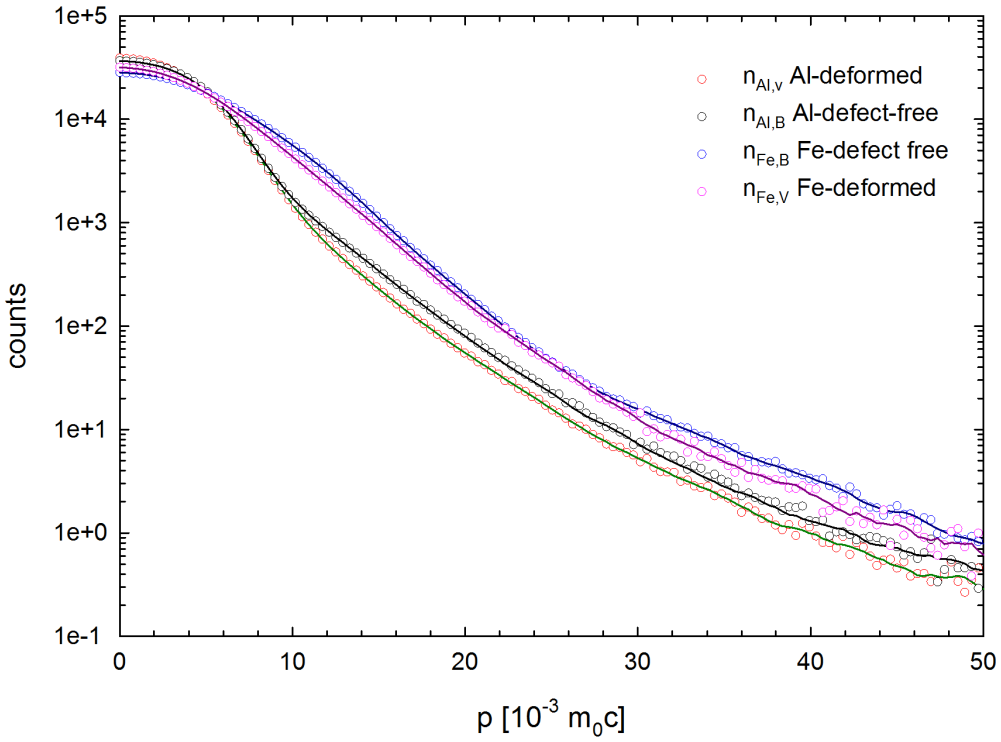

(a) Reference Doppler broadened CDB profiles.

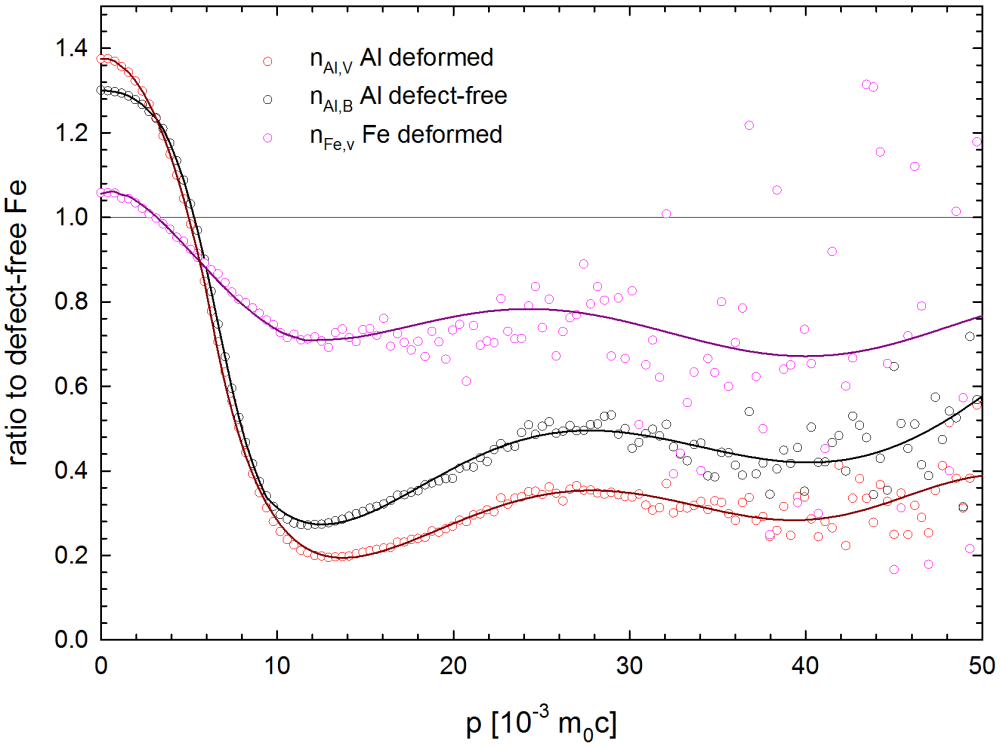

(b) Reference CDB ratio curves related to $n_{Fe,B}$, (i.e. defect-free Fe).

Figure 20: CDB profiles of reference samples.

vacancy the missing atom causes local decrease of core electrons, therefore, the low momentum contribution to annihilations is increased while the high momentum core annihilations are decreased.

The reference momentum profiles $n_{Fe,v}$, $n_{Al,v}$ were obtained by the following procedure:

(i) momentum profiles $n_{Al,def}$ and $n_{Fe,def}$ were measured on cold rolled Al and Fe samples by CDB

(ii) the cold rolled Al and Fe samples were measured also by positron lifetime spectroscopy and the fraction F'_v of positrons annihilated at vacancy-like defect was determined using STM

(iii) the momentum profile measured on cold rolled samples can be described as $n_{x,def} = (1 - F'_v)n_{x,B} + F'_v n_{x,V}$, where x stands for Fe or Al and $n_{x,B}$ is the momentum distribution of delocalized positrons which was determined on well annealed reference Fe and Al sample.

Hence, momentum distribution corresponding exclusively to positrons trapped at vacancy-like defects can be calculated using the equation

$n_{x,v} = (n_{x,def} - (1 - F'_v)n_{x,B})/F'_v$.

Momentum distributions $n_{Fe,v}$, $n_{Al,v}$ obtained by this procedure are plotted in Figure 20(a), while Figure 20(b) shows CDB ratio curves for these contributions related to the momentum distribution $n_{Fe,B}$ of free positrons in pure Fe.

Let's denote the fraction of annihilations of a positron in the free state and in the localized state in a vacancy by F_B and F_v, respectively. The sum of these fractions is unity, $F_B + F_v = 1$. From the measuring of positron lifetime one can derive the quantity F_v. For studied alloys it is listed in Table III. The fraction of positrons annihilated from the free state by Al electrons is denoted by $\xi_{Al,B}$. These quantities for various Fe-Al alloys were obtained by theoretical calculations performed for delocalized positron in Section 4.1.1 and are listed in Table V on page 53. The fraction of positrons trapped at vacancy and annihilated by Al electrons is denoted by $\xi_{Al,v}$. Analogically the symbols $\xi_{Fe,B}$ and $\xi_{Fe,V}$ denote the fractions of positrons annihilated by Fe electrons from the free state and from the trapped state in vacancies. The Doppler broadened profile measured on Fe-Al alloy can be then described by equation

$$n = F_v\xi_{Fe,v}n_{Fe,v} + F_v\xi_{Al,v}n_{Al,v} + F_B\xi_{Fe,B}n_{Fe,B} + F_B\xi_{Al,B}n_{Al,B}. \qquad (3.1)$$

Since there are only two kinds of atoms (Fe and Al) the fractions of annihilations at defects fulfill the condition $\xi_{Fe,v} + \xi_{Al,v} = 1$ and similarly the corresponding fractions for delocalized positrons fulfill the condition $\xi_{Fe,B} + \xi_{Al,B} = 1$. Therefore, the only unknown quantity in equation (3.1) is the $\xi_{Al,v}$ which is important for the determination of the chemical environment of a vacancy in Fe-Al alloys.

Figure 21 shows CDB ratio curves (related to well annealed pure Fe) measured on Fe-Al alloys of various compositions quenched from 1000 °C. The CDB ratio curve for well annealed pure Al sample is plotted in the figure as well. With increasing Al content the CDB ratio curves in Figure 21 clearly shift towards the curve for pure Al. This testifies that contribution of positrons annihilated by Al electrons increases.

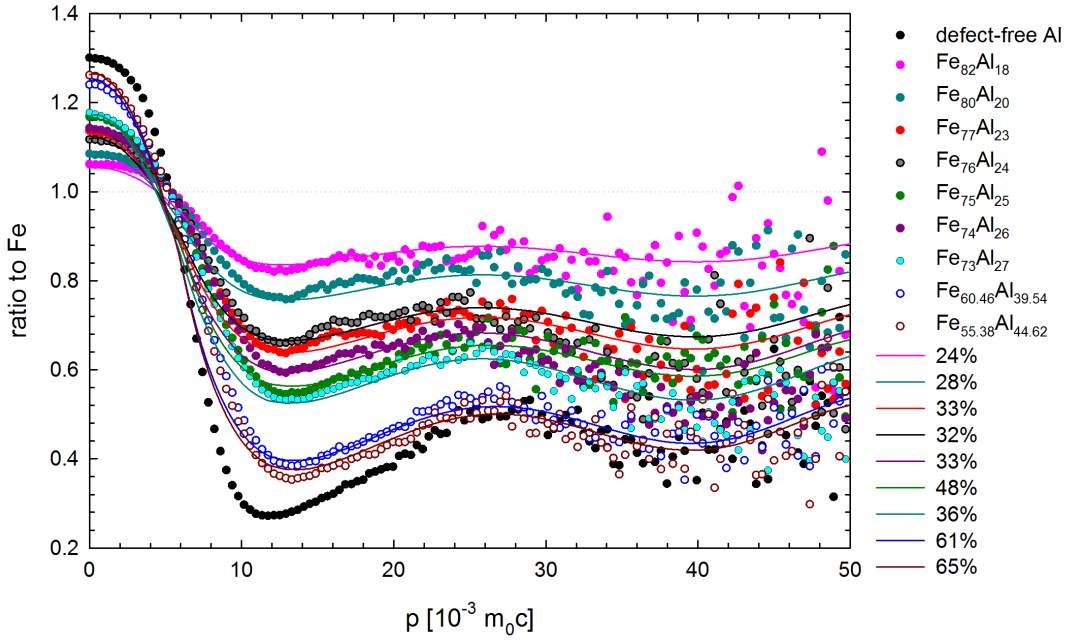

Figure 21: Fitted CDB ratio curves (related to well-annealed pure Fe) for Fe-Al alloys quenched from 1000 °C. Solid lines show fits by equation (3.1). The fractions $\xi_{Al,v}$ which give the best fit with experimental data are listed in legend.

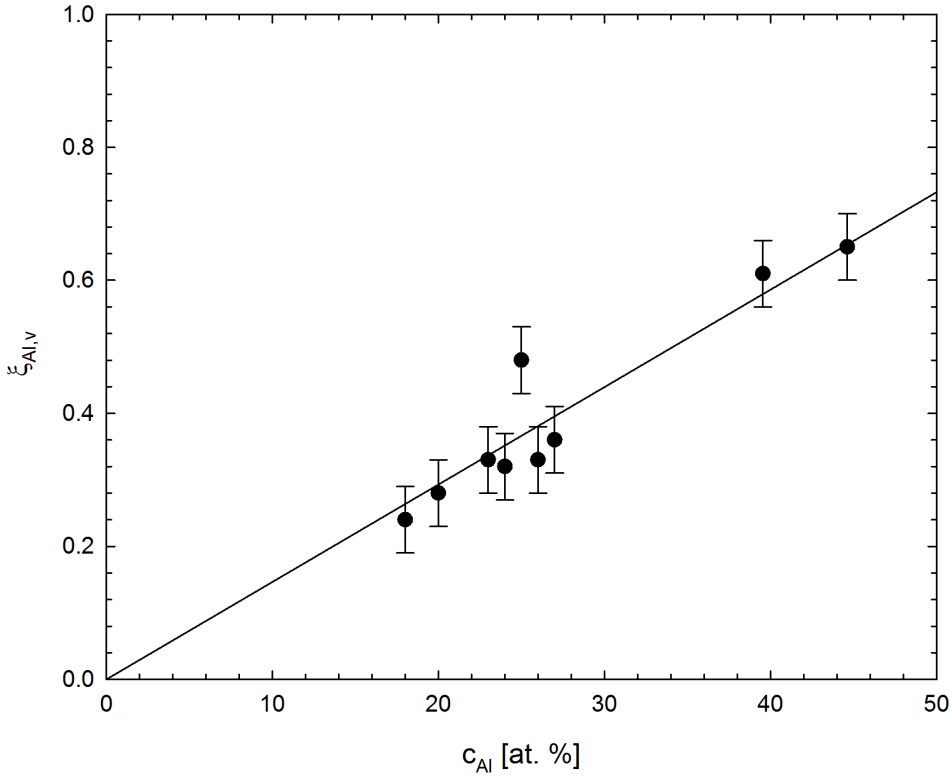

Figure 22: Fractions of trapped positrons annihilated by Al electrons determined by combination of CDB and LT spectroscopy on Fe-Al alloys samples quenched from 1000 °C.

The fraction $\xi_{Al,v}$ was determined from fit of Doppler broadened profiles by equation (3.1) and is plotted in Figure 22 as a function of Al content in the alloy. The fraction $\xi_{Al,v}$ obtained from experiment can be compared with $\xi_{Al,v}$ obtained from theoretical calculations for vacancies surrounded by various number of Al atoms which are listed in the Table VIII on page 64.

Solid lines in Figure 21 show fits of CDB profiles by equation (3.1). One can see in the figure that the model function (3.1) describes well the experimental points. The fractions $\xi_{Al,v}$ which gave the best fit are shown in Figure (3.1) in the legend.

Figure 23 shows $\xi_{Al,v}$ determined from fitting of CDB profiles plotted versus the lifetime τ_2 of positrons trapped in vacancies. One can see in Figure 23 that there is a strong positive correlation between τ_2 and $\xi_{Al,v}$. The higher number of Al atoms is surrounding vacancy the higher is the lifetime of trapped positrons.

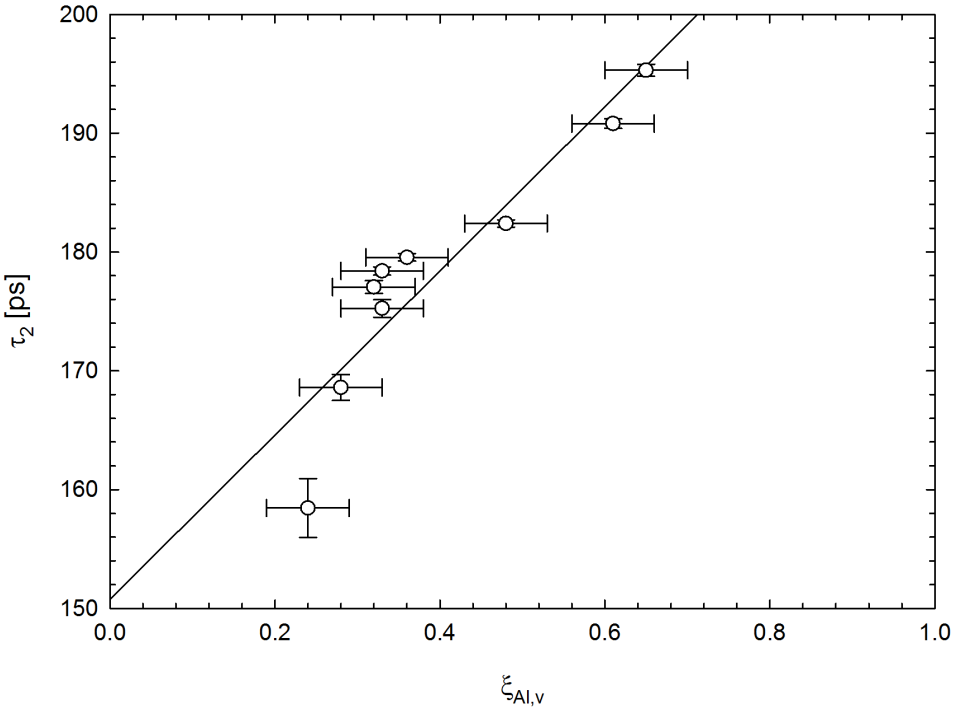

Figure 23: Positron lifetime of defect component τ_2 plotted versus the fraction of trapped positrons annihilated by Al electrons for Fe-Al alloys quenched from 1000 °C.

3.4.4 Annealed Fe-Al alloys of various compositions

Samples from the Section 3.4.3 quenched from 1000 °C were subsequently annealed at 520 °C for an hour and quenched to room temperature. Results of positron lifetime measurements on annealed samples are listed in Table IV.

Vacancy concentration c_v in annealed samples is lower than in quenched samples from Section 3.4.3 due to recovery of vacancies, i.e. thermally activated migration of vacancies to sinks at grain boundaries and on the surface of the sample.

Table IV: Results of positron lifetime measurements of Fe-Al alloys quenched from 1000 °C and subsequently subjected to annealing at 520 °C for 1 h finished again by quenching to room temperature.

c_{Al}	τ_f[ps]	$K_D[10^{-3}\mathrm{ps}^{-1}]$	F_v[%]	$c_v[10^{-6}\mathrm{at}^{-1}]$
Annealed at 520°C				
18	112(1)	0	0	<1
20	110(7)	2.0(6)	18(4)	5.1(7)
23	107(7)	4.9(2)	34(1)	12.2(5)
24	108(3)	5.4(9)	37(2)	14(2)
25	114(1)	14.5(2)	62(2)	14.7(5)
26	111(9)	4.3(2)	32(2)	10.7(5)
27	112(5)	4.1(1)	31(2)	10.2(3)
39.54	-	-	100	>200
44.62	-	-	100	>200

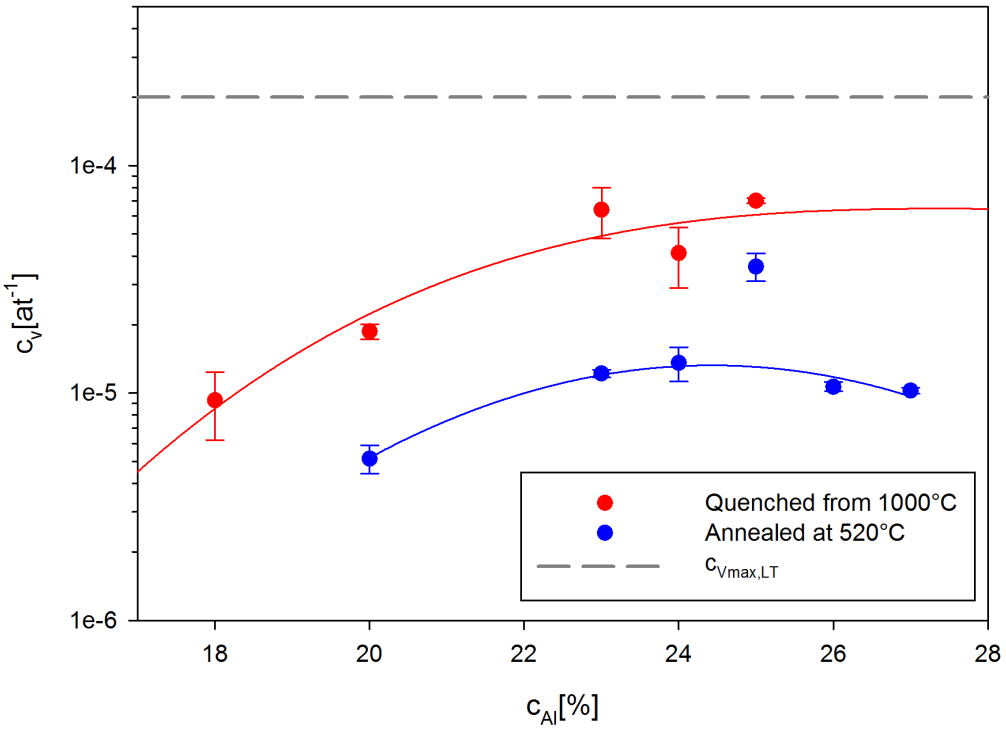

Figure 24: Vacancy concentration for different compositions of Fe-Al alloys quenched from 1000 °C (red points) and samples quenched from 1000 °C and subsequently annealed at 520 °C (blue points). Concentrations above the limit $c_{Vmax,LT}$ shown by dashed line are not measurable by PAS due to saturated trapping.

The driving force for recovery of vacancies is the tendency to reach equilibrium vacancy concentration which is at the annealing temperature of 520 °C substantially lower than concentration of quenched-in vacancies. This is well demonstrated in Figures 24. Samples with high Al content ($c_{Al} \geq 39\%$) exhibit saturated positron trapping at vacanies, i.e. the concentration of vacancies in these samples exceeds upper limit of $c_{Vmax,LT}$ from equation (1.18) shown in Figure 24 by dashed line. Value for $Fe_{75}Al_{25}$ slightly differs from sketched dependency which can be caused by the impurities mixed in by preparation because it was prepared elsewhere.

Positron lifetime spectrum of annealed alloy $Fe_{82}Al_{18}$ exhibited only one component with lifetime (112±1) ps originated from free positron annihilations, therefore, positron trapping rate at vacancies is virtually zero which means that the vacancy concentration c_v is below the detectable limit of 10^{-6} at.$^{-1}$.

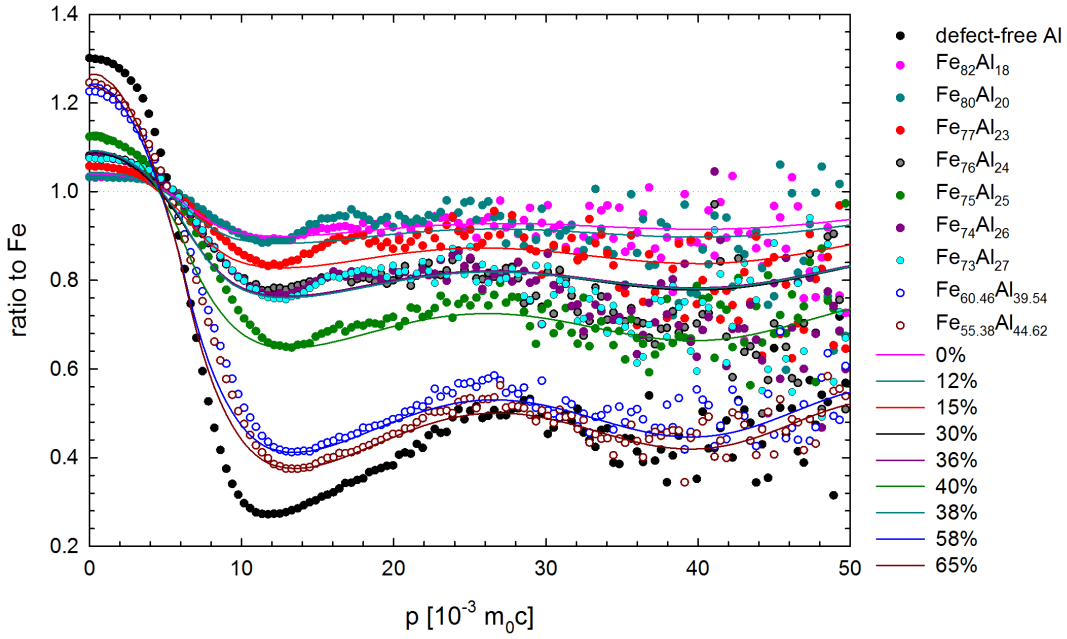

Figure 25: CDB ratio curves (related to well annealed Fe) for Fe-Al alloys quenched from 1000 °C and subsequently annealed at 520 °C. Solid lines show fit of CDB curves by equation (3.1). The fractions $\xi_{Al,v}$ which resulted in the best fit of experimental points are shown in the legend. The ratio curve for well-annealed reference pure Al sample is plotted in the figure as well.

Figure 25 shows CDB ratio curves (related to well-annealed Fe) for various Fe-Al alloys quenched from 1000 °C and subsequently annealed at 520 °C. One can see in the figure that similarly to the samples quenched from 1000 °C shape of CDB ratio curves resembles to the shape of CDB curve for pure Al. Obviously the contribution of positrons annihilated by Al electrons increases with increasing Al content in the alloy. This is similar trend as in the samples quenched from 1000 °C, compare with Figure 21. However, the comparison with samples quenched from 1000 °C shows that in samples annealed at 520 °C is the fraction of positrons annihilated by Al electrons generally decreased. This is due to lowered concentration of vacancies in samples annealed at 520 °C which was testified by

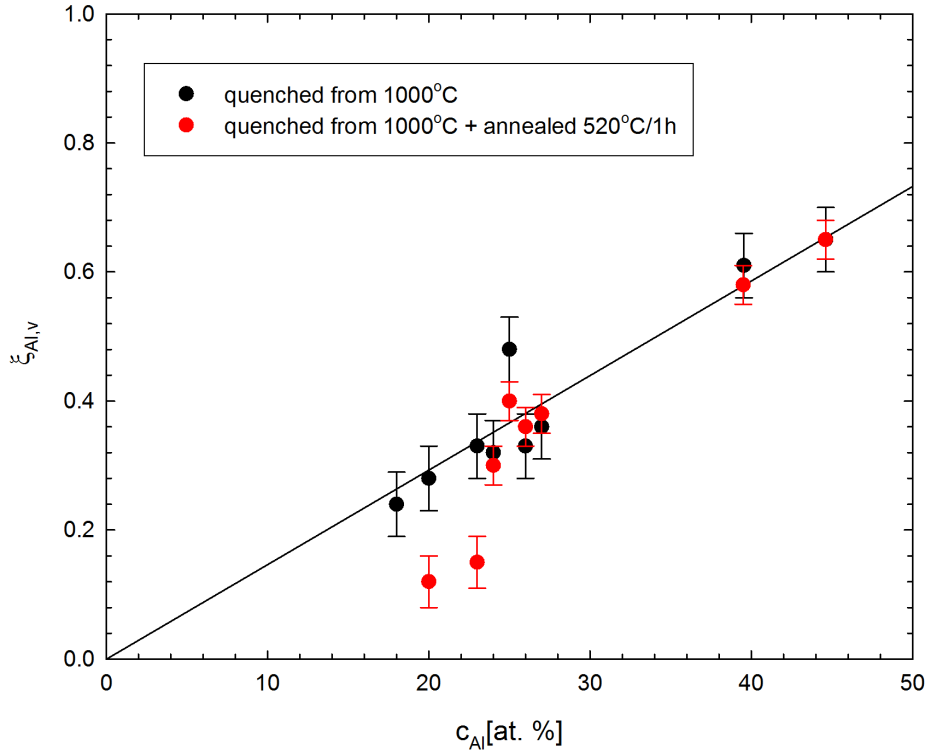

Figure 26: Results of fitting of CDB spectra of Fe-Al alloys quenched from 1000°C and subsequently annealed at 520 °C.

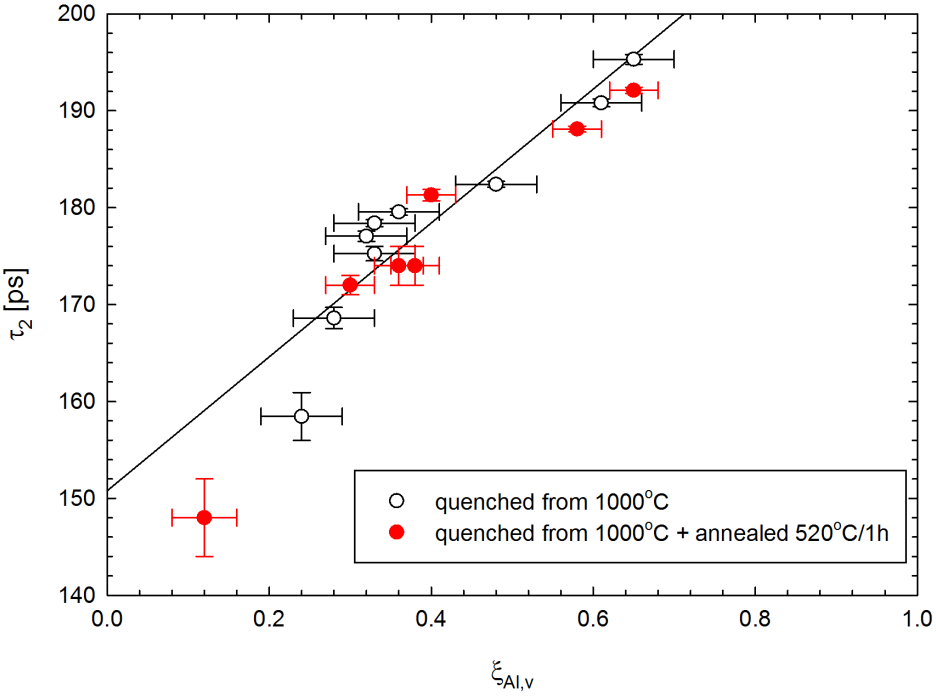

Figure 27: Correlation of the lifetime τ_2 of positrons trapped in vacancies with the fraction $\xi_{Al,v}$ for Fe-Al alloys quenched from 1000°C and subsequently annealed at 520 °C.

positron lifetime measurements. One can see in Figure 25 that CDB ratio curves measured on annealed samples are well described by equation (3.1). The fraction of positrons trapped in vacancies and annihilated by Al electrons $\xi_{Al,v}$ obtained from the best fit of experimental points by equation (3.1) is plotted in Figure 26 as a function of Al content. Clearly this dependence is very similar to that in the alloys quenched from 1000 °C. This indicates that the nature of defects in the alloys annealed at 520 °C remains unchanged and only their density was lowered. The correlation of the lifetime τ_2 of positrons trapped at vacancies with the fraction $\xi_{Al,v}$ is plotted in Figure 27. Obviously this correlation is similar to that in samples quenched from 1000 °C. This again testifies that annealing at 520 °C does not cause any change in the nature of positrons traps but only reduces their concentration.

3.4.5 Isochronally annealed Fe-Al alloys

Three selected quenched samples from Section 3.4.3 namely $Fe_{75}Al_{25}$, $Fe_{60.46}Al_{39.54}$ and $Fe_{55.38}Al_{44.62}$ were subjected to isochronnal annealing with annealing steps 40 °C / 40 min starting from 200 °C. Each annealing step was finished by quenching to silicon oil bath of room temperature and PAS investigations, namely positron lifetime measurements and CDB.

Positron lifetime spectra of isochronally annealed $Fe_{75}Al_{25}$ alloy consist of two components with lifetimes τ_1 and τ_2 and relative intensities I_1 and I_2 ($I_1 + I_2 = 100\%$). Temperature dependence of positron lifetimes τ_1, τ_2 and the relative intensity I_2 are plotted in Figure 17(a) and (b), respectively. The shorter component with lifetime τ_1 represents a contribution of free positrons, while the longer component with the lifetime τ_2 comes from positrons trapped at vacancies. Isochronally annealed $Fe_{60.46}Al_{39.54}$ and $Fe_{55.38}Al_{44.62}$ alloys exhibit single component positron lifetime spectra. Hence, concentration of vacancies in these alloys is so high that saturated positron trapping occurs and virtually all positrons are trapped in vacancies (i.e. I_2 is 100%). Temperature dependence of the lifetime τ_2 of positrons trapped in vacancies in $Fe_{60.46}Al_{39.54}$ and $Fe_{55.38}Al_{44.62}$ alloys is plotted in Figure 17(a).

One can see in Figure 17(b) that intensity of positrons trapped in vacancies in $Fe_{75}Al_{25}$ alloy exhibits a steep decrease at the temperatures above 400 °C. This testifies that concentration of vacancies in this alloy decreases, i.e. more positrons are annihilated from the free state. Minimum of I_2 values is reached at 480 °C. Annealing at higher temperatures causes again an increase in I_2 indicating an increase in concentration of defects. Lifetime of positrons trapped in vacancies remains constant except for statistical scattering. This testifies that the nature of defects remains unchanged and annealing causes only variations in the concentration of vacancies. Vacancy concentrations in $Fe_{75}Al_{25}$ alloy was determined using STM equations (1.14) - (1.17). Temperature dependence of the concentration of vacancies in $Fe_{75}Al_{25}$ alloy is plotted in Figure 29.

From inspection of Figure 29 one can realize that concentration of quenched-in vacancies does not change up to ∼400 °C. Annealing above 400 °C leads to a strong decrease in vacancy concentration. This indicates recovery of vacancies by diffusion into sinks at grain boundaries and on the surface. The minimum concentration of vacancies is achieved at 480 °C. Subsequent annealing at higher temperatures leads to a increase in vacancy concentration. This effect is caused by thermal vacancies. Above 480 °C the equilibrium concentration of quenched-in vacancies becomes high enough ($> 10^{-6}$at^{-1}) to be detected by positron lifetime spectroscopy. Hence, after each annealing step at temperatures above 480 °C the vacancy concentration in the sample is enhanced due to quenched-in thermal vacancies. One can notice the vacancy concentrations at temperatures above 720 °C are higher than the c_v after initial quench at 1000 °C. The possible reason could be that the initial annealing was performed in evacuated ampoule (p = 10^{-3} mbar) and therefore the quenching rate was slower than in case of isochronally annealed samples which were directly immersed in silicon oil of room temperature.

Isochronally annealed $Fe_{75}Al_{25}$, $Fe_{60.46}Al_{39.54}$ and $Fe_{55.38}Al_{44.62}$ were investigated by CDB. Figure 30 shows evolution of CDB ratio profiles (related to well-annealed reference Fe sample) for isochronally annealed $Fe_{75}Al_{25}$ alloy. One can see in the figure that above 400 °C the ratio profiles change and become closer

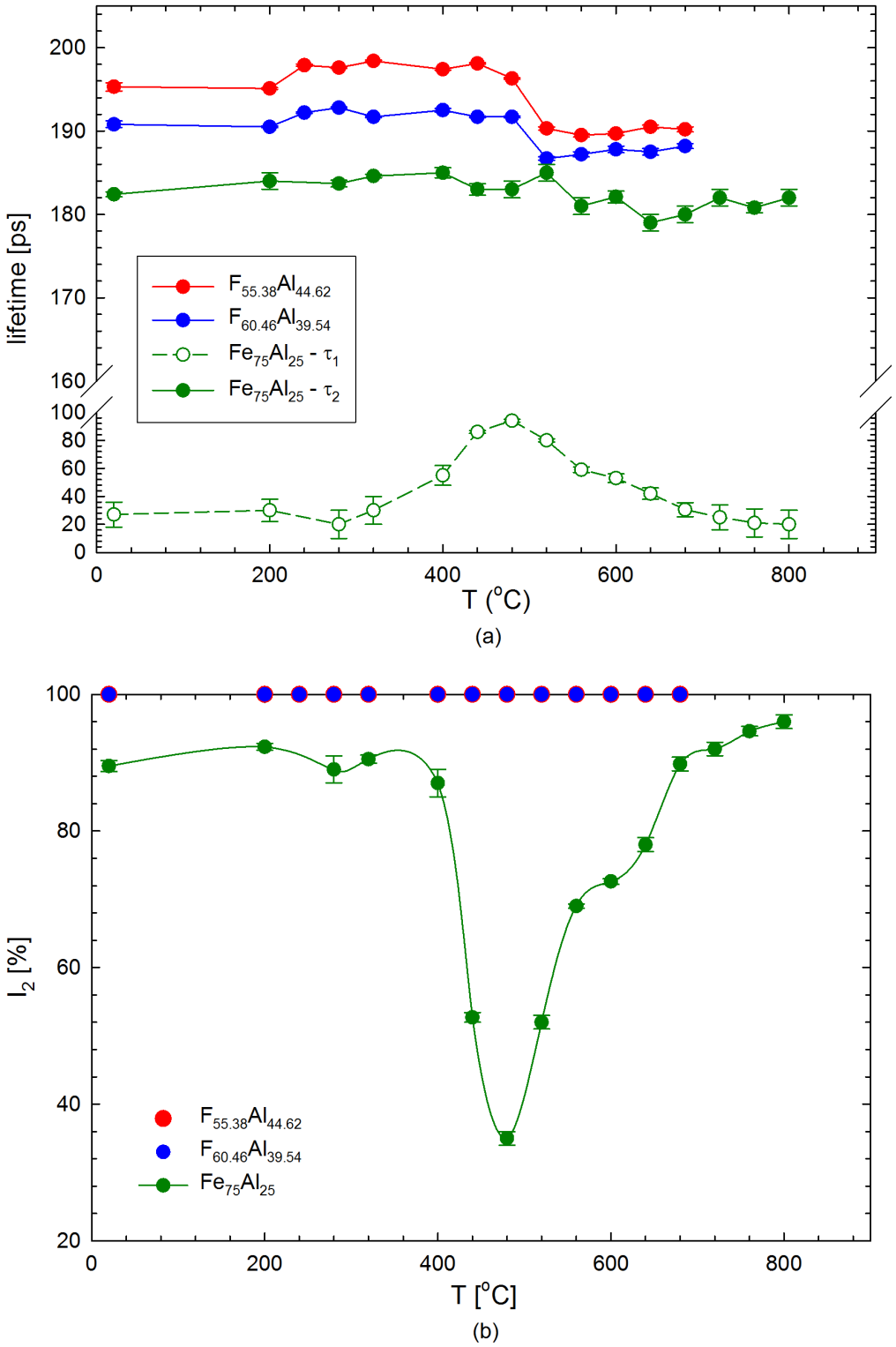

Figure 28: Temperature dependence of (a) positron lifetimes and (b) intensity I_2 of the shorter component from positrons trapped at vacancies in isochronally annealed alloys. Connecting lines are shown just to guide the eyes.

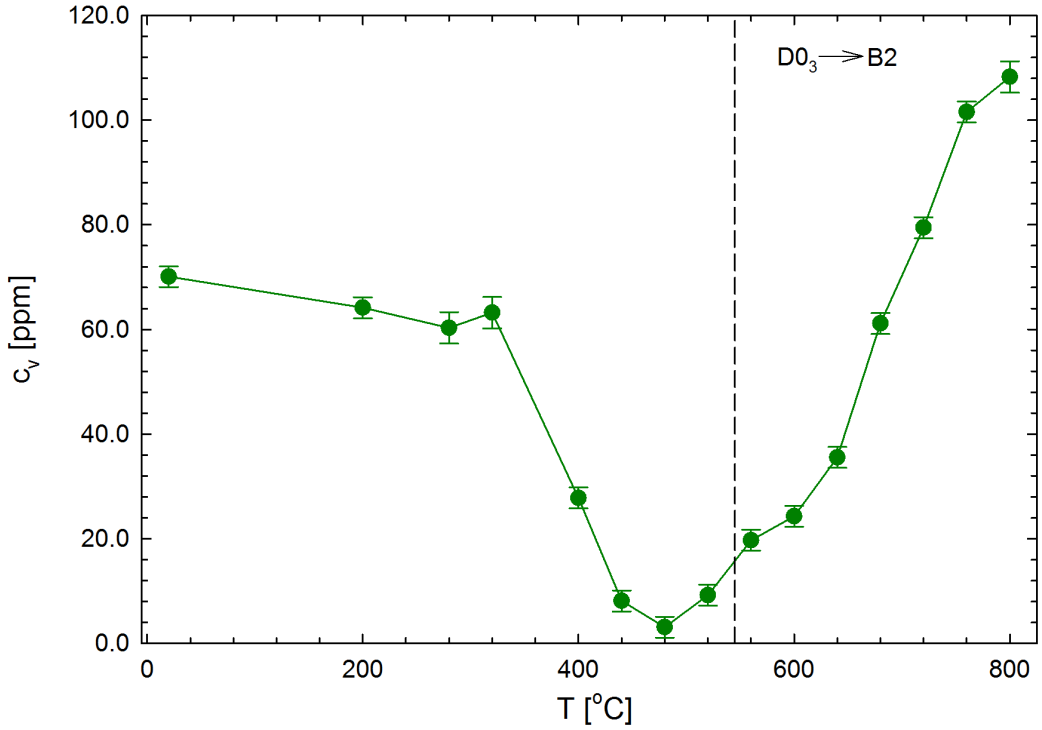

Figure 29: Temperature dependence of vacancy concentration in $Fe_{75}Al_{25}$ alloy quenched from 1000 °C and subsequently isochronally annealed.

to unity, i.e. the contribution of positrons annihilated by Al electrons decreases. This corresponds well with recovery of vacancies in this temperature range.

The development of the CDB ratio curves during isochronal annealing of $Fe_{60.46}Al_{39.54}$ and $Fe_{55.38}Al_{44.62}$ alloy is plotted in Figures 31 and 32, respectively. Contrary to $Fe_{75}Al_{25}$ alloy the CDB ratio curves measured in $Fe_{60.46}Al_{39.54}$ and $Fe_{55.38}Al_{44.62}$ alloys remain basically unchanged with temperature. This is due to saturated positron trapping in vacancies. Quenched $Fe_{60.46}Al_{39.54}$ and $Fe_{55.38}Al_{44.62}$ alloys contain significantly higher concentration of vacancies than $Fe_{75}Al_{25}$ alloy, see Figure 18. Hence, although the concentration of vacancies in $Fe_{60.46}Al_{39.54}$ and $Fe_{55.38}Al_{44.62}$ alloys annealed above 400 °C most probably decreased as indicated by a drop in microhardness (see Figure 14) it remains still high enough to cause saturated positron trapping.

Using equation (3.1) it is possible to determine the fraction $\xi_{Al,v}$ of positrons trapped in vacancies and annihilated by Al electrons. The fraction $\xi_{Al,v}$ obtained from fitting of CDB ratio curves of isochronally annealed samples is plotted in Figure 33 as a function of the annealing temperature. One can see in Figure 33 that

(i) the fraction $\xi_{Al,v}$ becomes higher in alloys with higher Al content;

(ii) for each alloy the fraction $\xi_{Al,v}$ remains approximately constant during annealing. This testifies that annealing causes only variation in vacancy concentration while the chemical environment of vacancies remains unchanged.

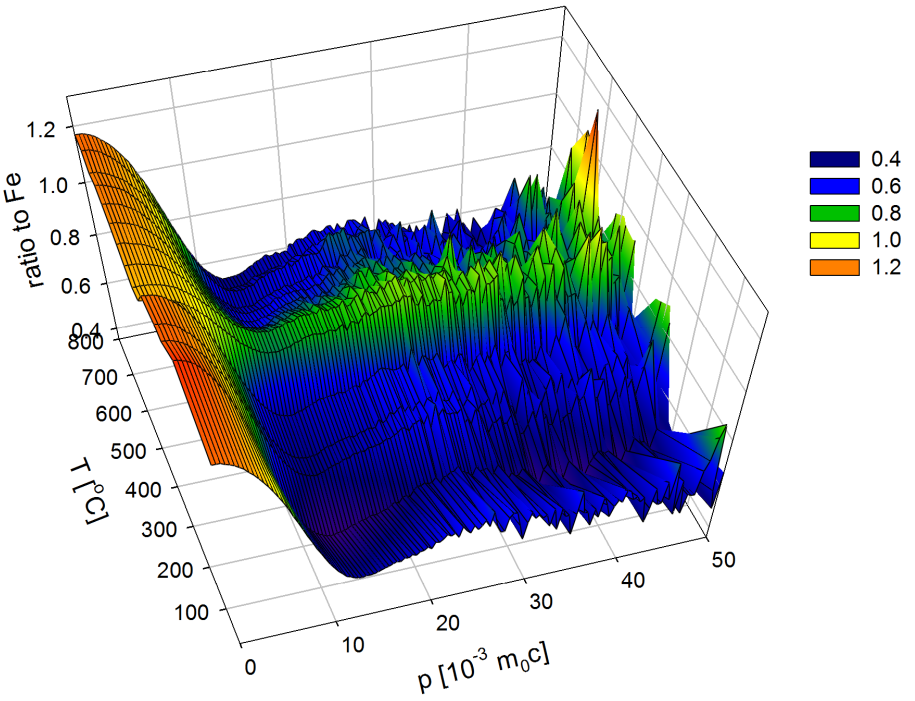

Figure 30: 2.5D color plot showing the development of CDB ratio curves (related to well-annealed Fe) for $Fe_{75}Al_{25}$ alloy during isochronal annealing.

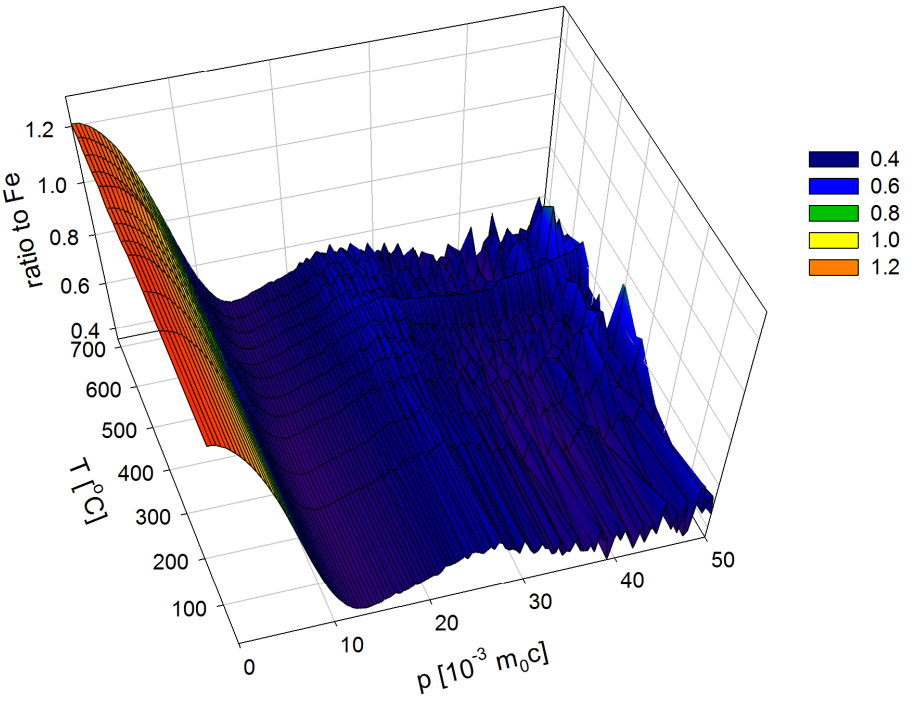

Figure 31: 2.5D color plot showing the development of CDB ratio curves (related to well-annealed Fe) for $Fe_{60.46}Al_{39.54}$ alloy during isochronal annealing.

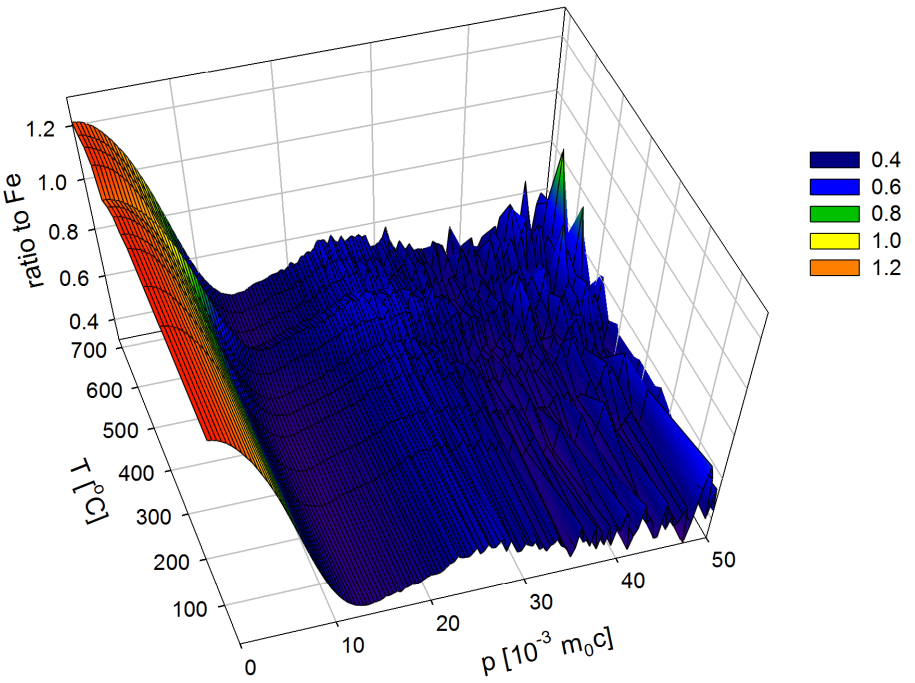

Figure 32: 2.5D color plot showing the development of CDB ratio curves (related to well-annealed Fe) for $Fe_{60.46}Al_{39.54}$ alloy during isochronal annealing.

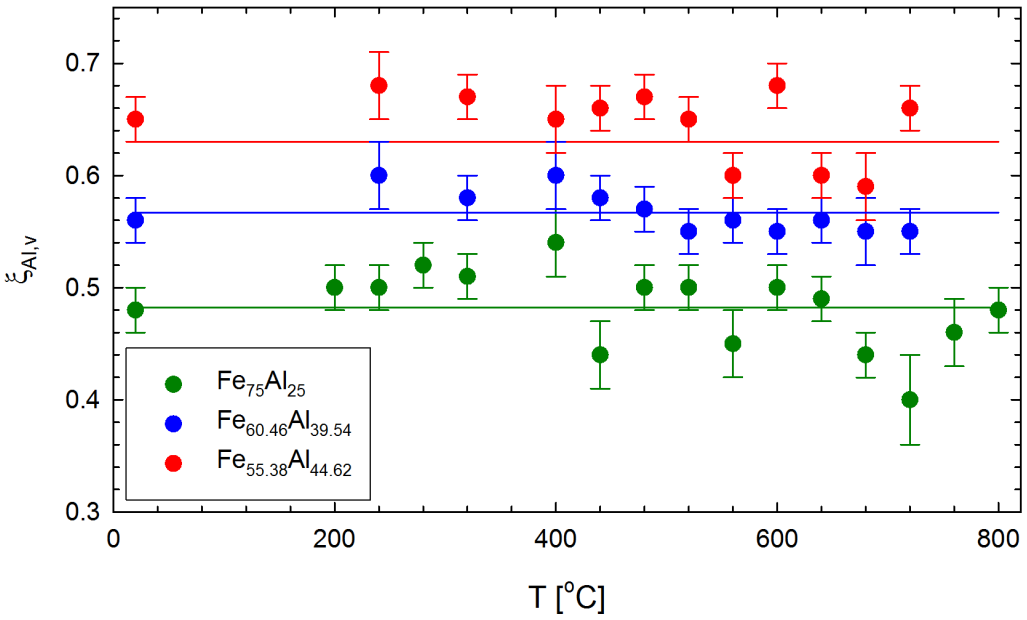

Figure 33: Temperature dependence of the fraction $\xi_{Al,v}$ of positrons trapped in vacancies annihilated by Al electrons determined from fitting of CDB ratio curves by equation (3.1)

Chapter 4

Results of the theoretical calculations

4.1 PAS characteristics calculations

The quantum-mechanical theoretical calculations were performed by ATSUP code for Fe-Al alloys with broad range of composition from $Fe_{82}Al_{18}$ to $Fe_{50}Al_{50}$. The lattice parameters used in calculations are listed in Table I. For the $Fe_{75}Al_{25}$ and $Fe_{60.46}Al_{39.54}$ the lattice parameters determined by XRD in this work were used, while for other alloys were used lattice parameters determined by XRD in [22]. Theoretical calculations performed on a B2 supercell contained 1024 atom sites and A-sublattice was occupied exclusively by Fe atoms, while the B-sublattice was randomly filled by Fe and Al atoms so that the overall composition in the superlattice equals to the composition of the studied alloy. Calculations for A2 structure were performed on a supercell containing 1024 atom sites which were randomly occupied by Al and Fe atoms. For each composition 10 configurations of atoms in supercell for the B2 structure were generated and similarly also for some compositions of the A2 structure supercells. Calculation of positron parameters was run independently for each configuration and the average of these 10 independent runs was taken. Variance of the calculated parameters for each composition was estimated from the spread of the results obtained in the 10 independent runs.

4.1.1 Delocalised positron

The positron annihilation characteristics were calculated firstly for a perfect (defect-free) lattice of Fe-Al alloys with B2 structure. The results of calculations of positron annihilation characteristics, i.e. the lifetime of delocalized positron and the fraction of positrons annihilated by Al electrons, in a B2 structure supercell are shown in Table V.

From the values $\xi_{Al,B}$ for $Fe_{75}Al_{25}$ alloy one can see that the fraction of positrons annihilated by Al electrons is almost insensitive to variation of the lattice constant found in the experiment. However, $\xi_{Al,B}$ is sensitive to the composition of the sample, i.e to the number of Al atoms in the supercell. The positron bulk lifetime varies with the lattice parameter for these samples. It decreases with decreasing lattice constant, which is in agreement with decreasing electron den-

Table V: The results of calculations for the Fe-Al alloys quenched from T_Q measured by XRD (this work and [22]). The bulk lifetime and fraction of positrons annihilated by Al. The $D0_3$ structure lattice parameter a'_{exp}, which is two times the lattice parameter a_{exp} of B2 structure, is given only for comparison. The uncertainly of calculated parameters (one standard deviation) estimated from calculations in 10 randomly generated B2 supercells is given in brackets.

Composition	T_Q[°C]	a_{exp}[Å]	a'_{exp}[Å]	τ_B[ps]	$\xi_{Al,B}$[%]
$Fe_{82}Al_{18}$	600	2.8953	5.7906	107.5(6)	11.6(9)
$Fe_{80}Al_{20}$	600	2.8970	5.7940	107.9(9)	13(1)
$Fe_{77}Al_{23}$	600	2.8977	5.7954	108.5(5)	14.7(7)
$Fe_{76}Al_{24}$	600	2.8990	5.7980	108.9(7)	15.6(8)
$Fe_{75}Al_{25}$	1000	2.9179	5.8358	111.1(1)	16.1(6)
$Fe_{75}Al_{25}$	520	2.8996	5.7991	109.1(1)	16.1(6)
$Fe_{70}Al_{30}$	600	2.8967	5.7934	109.7(1)	20(1)
$Fe_{72}Al_{28}$	600	2.8960	5.7920	109.3(2)	18.4(8)
$Fe_{65}Al_{35}$	600	2.8943	5.7886	110.6(3)	25(2)
$Fe_{60.46}Al_{39.54}$	1000	2.8993	5.7985	112.5(3)	30(1)
$Fe_{60.46}Al_{39.54}$	520	2.8969	5.7937	112.3(5)	30(1)
$Fe_{60}Al_{40}$	600	2.8963	5.7926	112.3(3)	30(2)
$Fe_{55}Al_{45}$	600	2.9023	5.8046	114.7(2)	37.2(9)
$Fe_{50}Al_{50}$	600	2.9090	5.8180	117.4(-)	42.1(-)

sity due to increasing volume of the supercell. The overlap integral (1.2) decreases and so the annihilation rate λ_B decreases.

The computational program enables to save the files with the calculated electron and positron density. From these output files it is possible to make cuts in an arbitrary direction (2D graph) or in any crystallographic plane (3D graph). Figures 34 and 35 show in the middle panel color coded contour plot of calculated positron density in two different (001) planes in the A-sublattice in $Fe_{55}Al_{45}$ alloy. Note that the A-sublattice contains only Fe atoms. The adjacent (002) planes, i.e. B-sublattice planes parallel to the (001) plane are shown in the upper and lower panel. Note that (002) planes are occupied preferentially by Al atoms. In the alloy with composition $Fe_{55}Al_{45}$ the probability that a site in the B-sublattice will be filled by Al atom is 90%, while the probability that it will be occupied by Fe atom is only 10%. In Figures 34,35 the Al atoms are shown as big circles while the Fe atoms are plotted as small circles. One can see in the figures that positron density is spread over a large volume - i.e. positron is delocalized in the lattice.

Moreover, one can see that positron density in (001) plane is elevated in the region where Fe atoms are present in adjacent (002) planes in the B-sublattice. It means that positrons are repelled from Al atoms more than from Fe atoms and tends to be located preferentially along the A-sublattice. Due to this effect the calculated fractions $\xi_{Al,B}$ of positrons annihilated by Al electrons, which are listed in Table VI, are generally lower than the atomic concentration of Al atoms in the corresponding alloys. The results are illustrated in Figure 36 and one can notice the parabolic dependence of $\xi_{Al,B}$ on aluminium content in the supercell. For the comparison the calculations on A2 structure supercells were performed. For each composition ten supercells containing 1024 atom sites occupied with Fe

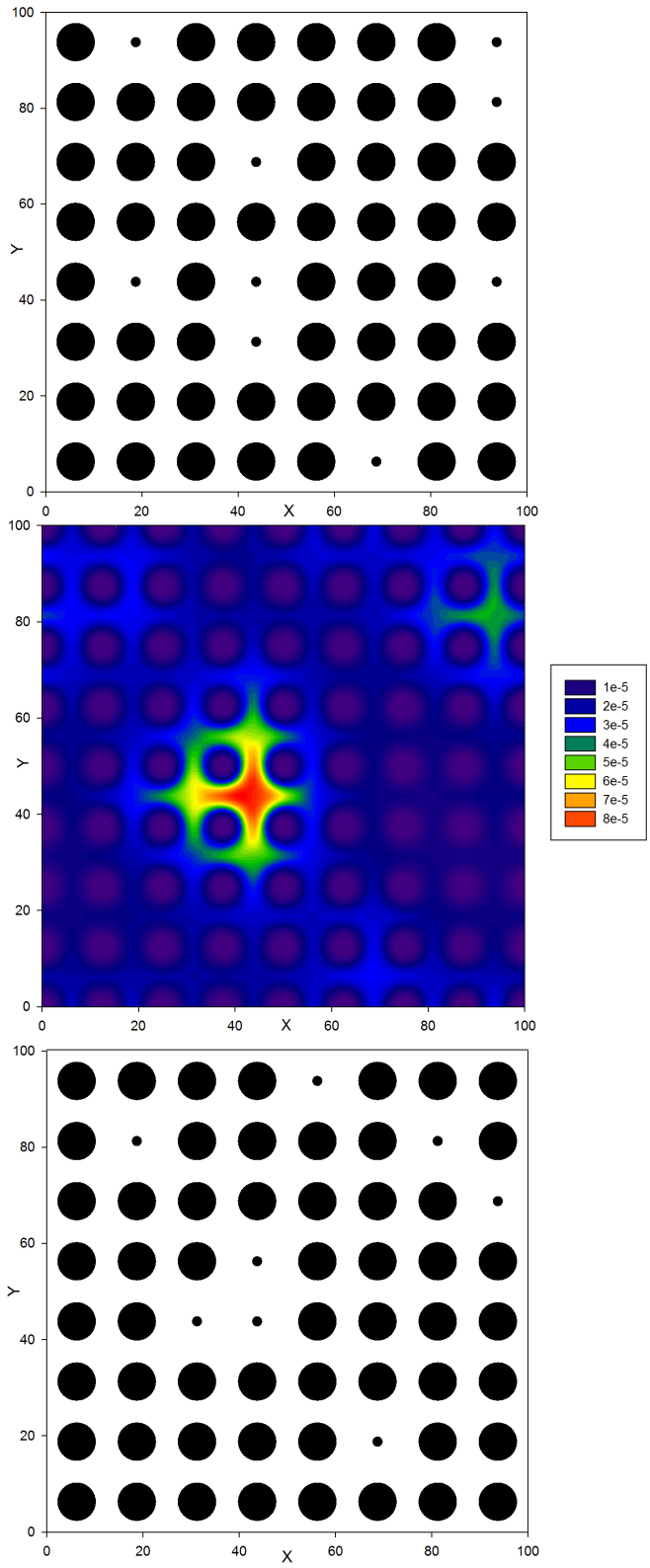

Figure 34: Upper and lower panel show positions of atoms of Fe (large circles) and Al atoms (small circles) in the (002) planes belonging to the B-sublattice and adjacent to the A-sublattice (001) plane. The positron density in the A-sublattice (001) plane is plotted in the central panel.

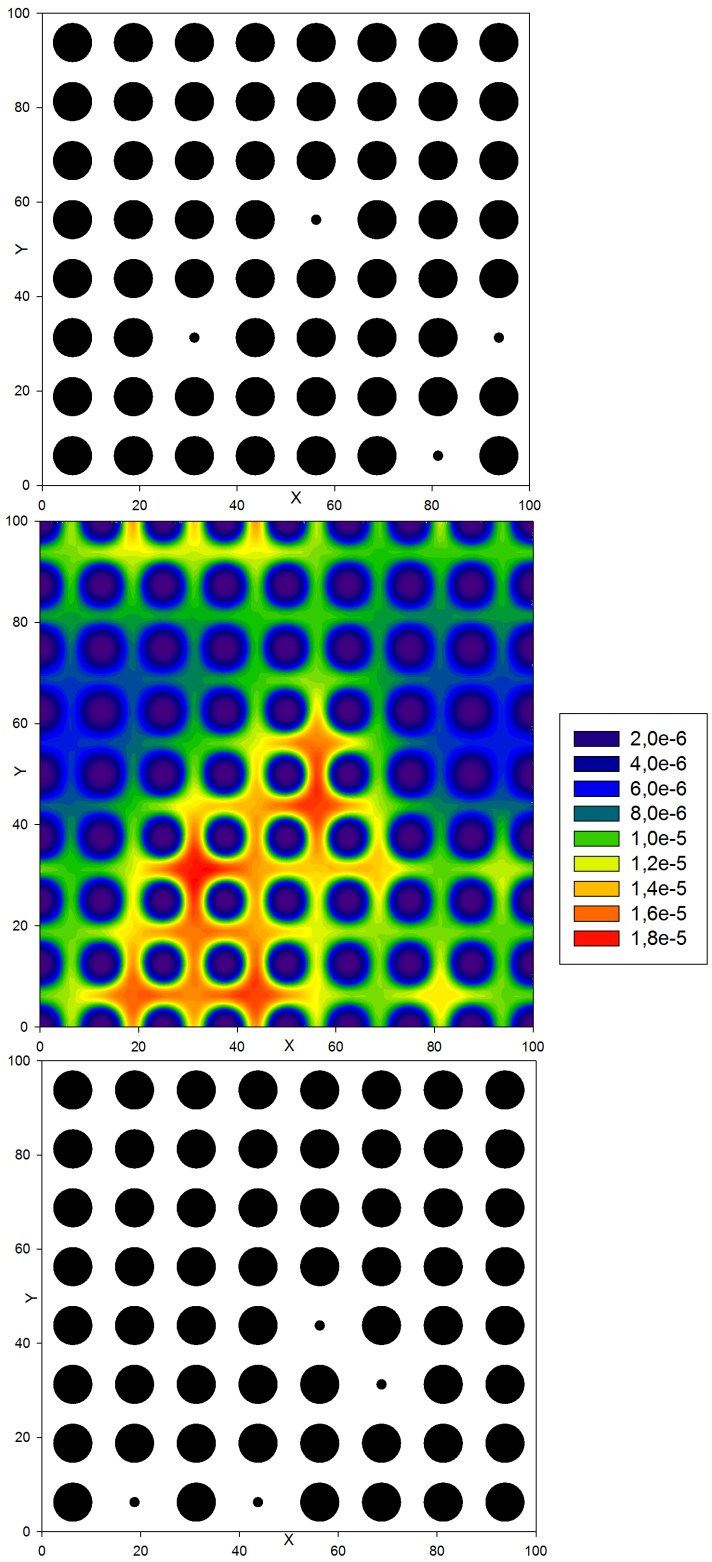

Figure 35: The same plot as in Figure 34, however taken in a different part in the B2 supercell.

an Al atoms in the fraction corresponding to the compositions were generated in order to obtain delocalized positron annihilation characteristics by ATSUP code calculations. Results for A2 structure calculations shown in Figure 36 differs from B2 ordered structure results. In A2 structure positron annihilations are purely random and fraction of Al annihilations increase linearly with increasing Al content. Moreover, fraction of annihilations with Al $\xi_{Al,B}$ is much lower than is the composition of model alloy, which is in concordance with the Figures 34,35 showing positron density elevated at the regions with higher Fe occurence. Therefore, the quadratic dependency suggest that the positron do not annihilate randomly in B2 structure with both Fe and Al atoms. Delocalized positron density is preferentially spread in the A-sublattice containing Fe atoms, moreover, it is repelled from regions with higher Al content in the nearest B-sublattice sites. This statement is supported by the two extreme cases, $Fe_{50}Al_{50}$ and $Fe_{75}Al_{25}$. Firstly, in $Fe_{50}Al_{50}$ all the B-sublattice sites are occupied exclusively by Al atoms, therefore, positron density is spread more uniformly in A-sublattice which in the close neighbourhood of Al atoms from B-sublattice and so $\xi_{Al,B}$ is the highest. Secondly, in $Fe_{75}Al_{25}$ the distribution of Fe and Al atoms is random with 50% probability at each site of B-sublattice so the positron density is inevitably in the regions with Al content. On the other hand, at the composition between these two extreme cases, the positron has an opportunity to chose random regions with lower Al content in B-sublattice so that the positron density is elevated at the regions containing more Fe atoms. As a consequence, the fraction of positron annihilated by Al electrons is decreased and the curve connecting two compositions $Fe_{50}Al_{50}$ and $Fe_{75}Al_{25}$ is not linear but the Al fraction of annihilation $\xi_{Al,B}$ is lowered relatively to the random dependency which would be linear as is the A2 structure curve.

The dependency of calculated bulk positron lifetime is plotted in the Figure 37 for B2 and A2 structure. Both curves show increasing quadratic dependency of τ_B on Al content with small deviations caused by different lattice parameters of model supercells.

Correlation of τ_B and $\xi_{Al,B}$ is illustrated in Figure 38 for A2 and B2 structures. Positron lifetime in defect-free Fe-Al alloys increases with increasing fraction of positron annihilation with Al atoms.

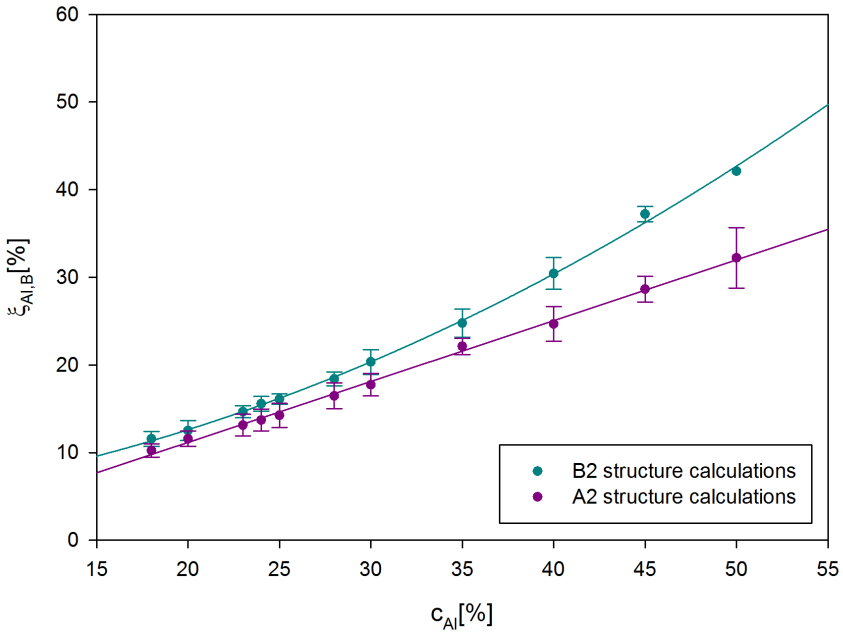

Figure 36: Calculated bulk positron fraction of annihilations with Al for Fe-Al alloys of various compositions. Parabolic regression fits best the B2 structure while linear regression is more suitable for A2 structure calculation results of $\xi_{Al,B}$.

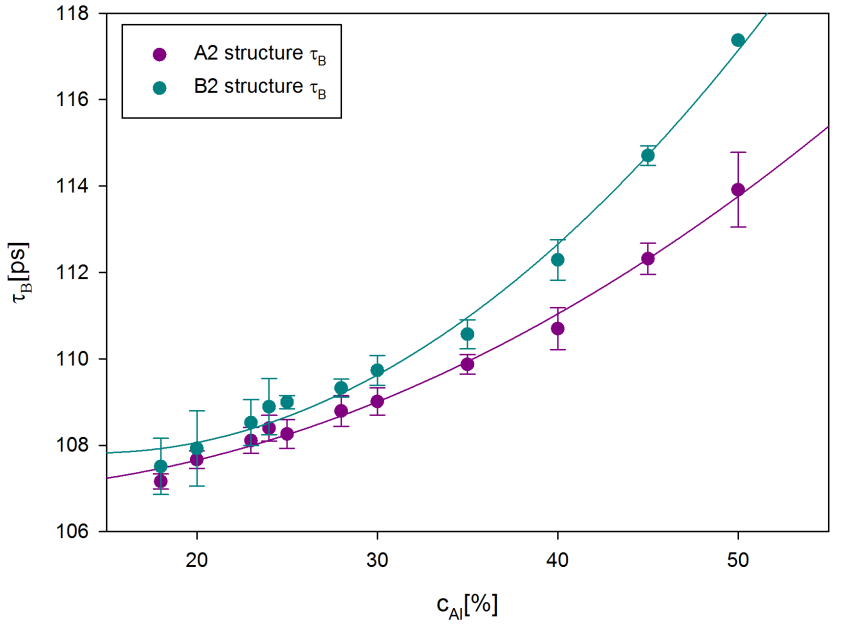

Figure 37: Calculated positron bulk lifetime for Fe-Al alloys of various compositions. Quadratic regression curves are illustrated as well.

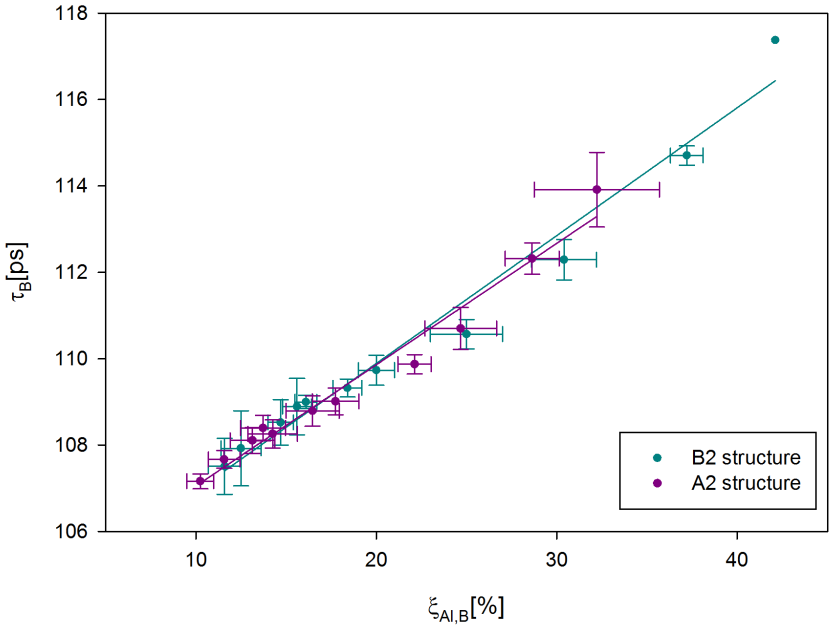

Figure 38: Calculated bulk positron lifetime in correlation with fraction of annihilations with Al for Fe-Al alloys of various compositions. Linear fits of data corresponds well to each other for B2 and A2 structure.

4.1.2 The positron trapped at a vacancy

A positron trapped at a vacancy in the A-sublattice in Fe-Al alloys was modeled in a B2-structure supercell containing 1023 atoms. Vacancy represents potential well for positrons due to reduced positive charge density. As a consequence positron can be localized (trapped) at vacancy. Positron binding energy to vacancy E_B is the difference between the ground state energy of delocalized positron and positron trapped in vacancy. Calculation of electron and positron density was performed by ATSUP code. Cuts of electron and positron densities were made in the plane containing the vacancy. It is well known that a vacancy in the B-sublattice exhibits significantly higher energy than vacancy in the A-sublattice [23]. For this reason only vacancies in the A-sublattice were considered in calculations.

Figures 39(a) and 39(b) show 3D plots of density of the positron trapped in vacancy in linear and logarithmic scale, respectively. The positron density plot shows highly localized positron, therefore positron density is vanishing in the volume of defect-free lattice and highly increased in the volume of the vacancy.

In Figure 40 is contour plot of electron density in logarithmic scale.

The results of the calculations of the positron annihilation characteristics for vacancy in the A sub-lattice are shown in the Table VI. The nearest neighbors of the vacancy are atoms on the B sub-lattice which were randomly populated by Al atoms according to the composition of corresponding alloy, e.g. for $Fe_{75}Al_{25}$ alloy 50% of sites in the B-sublattice is occupied by Al atoms.

Table VI: Results of the calculations for Fe-Al alloys with a'_{exp} measured by XRD, positron lifetime in a monovacancy τ_v and its fraction of annihilations with Al electrons $\xi_{Al,v}$. The error values noted in brackets are the deviations from the aritmetic average calculated from 10 independent calculations.

Samples			B2		A2	
c_{Al}[%]	T_Q[°C]	a'_{exp}[Å]	τ_v[ps]	$\xi_{Al,v}$[%]	τ_v[ps]	$\xi_{Al,v}$[%]
18	600	5.7906	185(3)	26(17)	184(2)	19(12)
20	600	5.7940	185(2)	25(12)	184(1)	19(9)
23	600	5.7954	186(2)	30(13)	185(1)	21(7)
24	600	5.7980	186(3)	27(18)	186(2)	27(12)
25	1000	5.8358	191(2)	38(12)	184(1)	21(9)
25	520	5.7991	188(2)	38(12)	-	-
28	600	5.7920	188(2)	39(12)	185(2)	24(11)
30	600	5.7934	188(2)	39(15)	185(1)	26(9)
35	600	5.7886	188(5)	44(10)	186(3)	35(17)
39.54	1000	5.7985	191(1)	53(7)	-	-
39.54	520	5.7937	190(2)	48(12)	-	-
40	600	5.7926	191(1)	55(8)	187(3)	36(15)
45	600	5.8046	192(1)	58(7)	189(2)	41(13)
50	600	5.8180	195.6(-)	67(-)	190(2)	45(12)

One can see in Table VI that the lifetime τ_v of positrons trapped in vacancy in the A-sublattice is influenced by lattice parameters. Furthermore, increase of Al content in the alloy leads to an increase of Al concentration in the vicinity

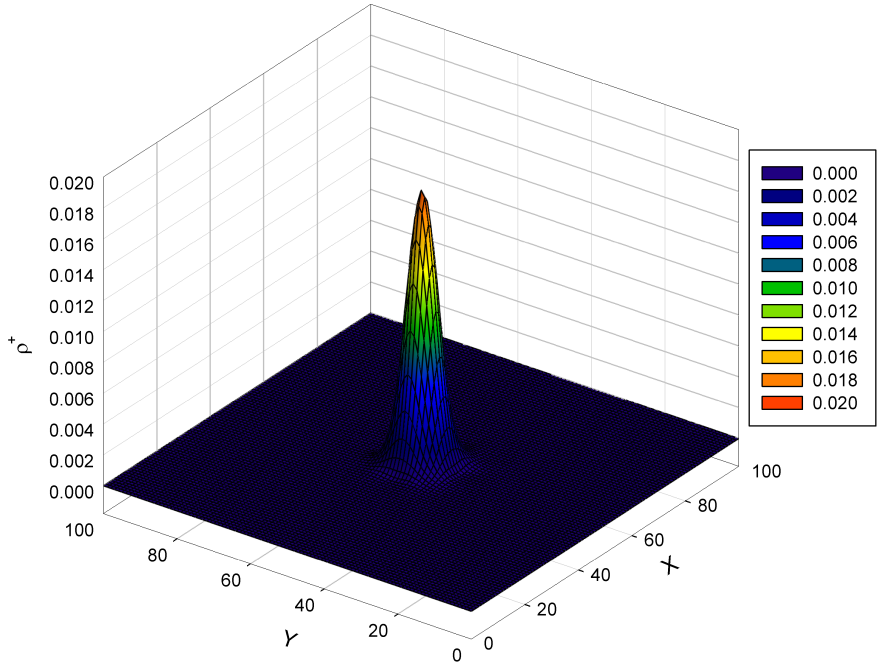

(a) linear scale

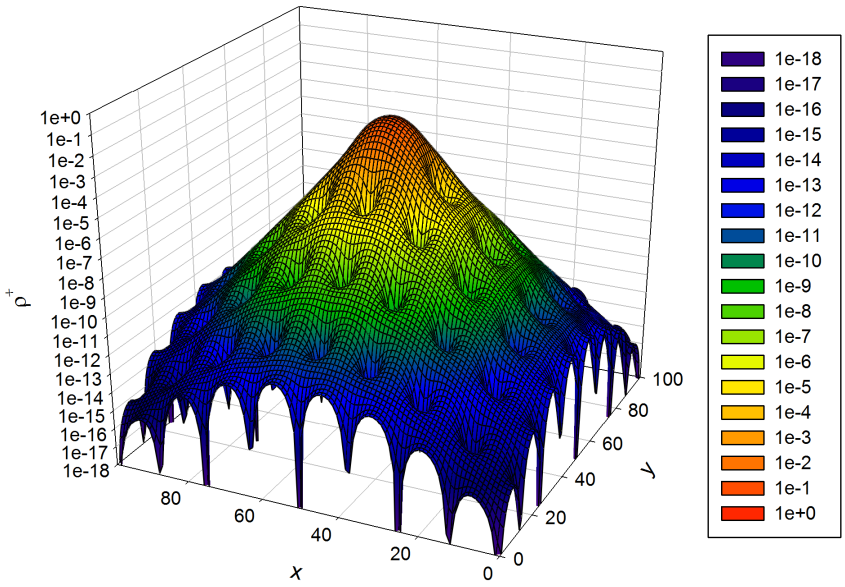

(b) logarithmic scale

Figure 39: Positron density in (001) plane containing vacancy.

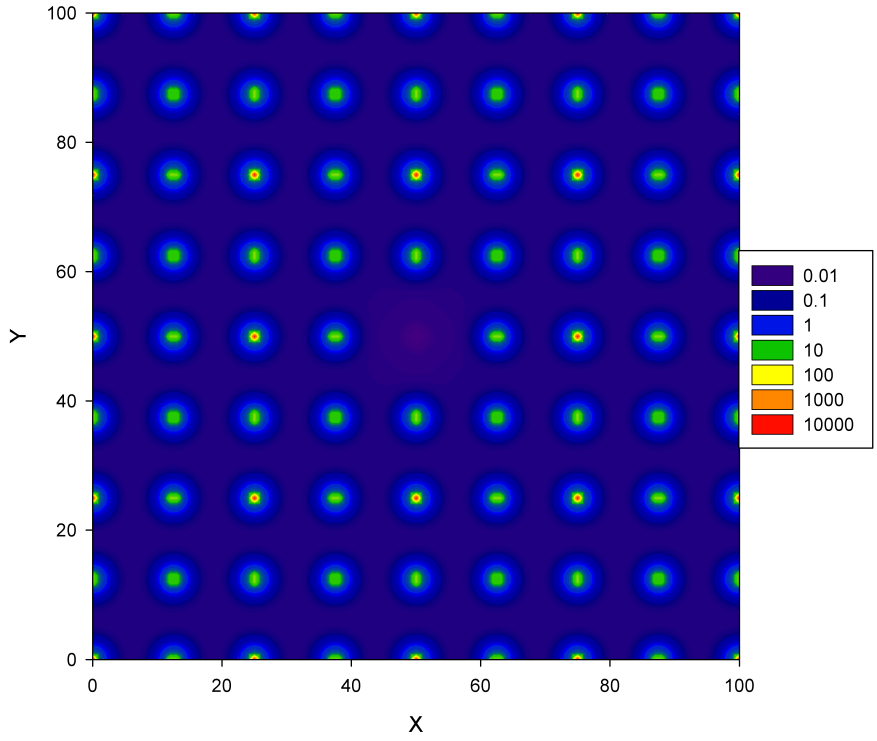

Figure 40: Electron density in a plane containing A-vacancy.

of vacancy. As a consequence, positron lifetime increases. Fraction of positrons annihilated by Al electrons $\xi_{Al,v}$ strongly depends on the chemical environment of monovacancy, therefore there is large spread of $\xi_{Al,v}$ values in Table VI.

Quantum mechanical calculation results in Table VI show that the monovacancy on the A-sublattice of B2 structure exhibits higher fraction of annihilations with Al electrons than is the concentration of Al atoms for all the compositions.

Calculations for monovacancy in the A-sublattice of B2 structure show higher $\xi_{Al,v}$ than calculation for vacancy in A2 structure. This is caused by the fact that in B2 structure the A-sublattice contain exclusively Fe atoms and therefore NN sites of vacancy occupy the B-sublattice containing lower fraction of Fe atoms than in the case of A2 structure, which is completely disordered.

The fractions of positrons annihilated by Al electrons were calculated for various defects and are listed in Table VII. Lattice parameters from the Table I were used in calculations performed in a supercell of B2 structure containing 1024 atom sites. Only one calculation was performed for each composition. The rough estimation of the error of f_{Al} is below 1%.

The calculations were performed for the following defects: vacancy in the A-sublattice with Fe antisite atom (vac+$\mathrm{Fe_{Al}}$), monovacancy in the A-sublattice with the all nearest neighbors (NN) sites occupied by Al atoms (vac+NN), divacancy aligned in [100] direction in the A sub-lattice surrounded by Al atoms in NN sites (2vac+NN), so called triple defect consisting of two vacancies in the

A sub-lattice with Fe antisite and aligned in [100] direction (triple), triple defect in ordered B2 with only Al atoms in NN B-sublattice sites (B2-triple), see Figure 41(a), monovacancy in the A-sub-lattice with NN and next nearest neighbors (NNN) sites occupied by Al atoms (vac+NNN), divacancy aligned in [100] direction in the A-sublattice of ordered B2 structure with 2 Fe antisite (2vac+2Fe_{Al}), see Figure 41(b). These defects have different open volume and chemical environment.

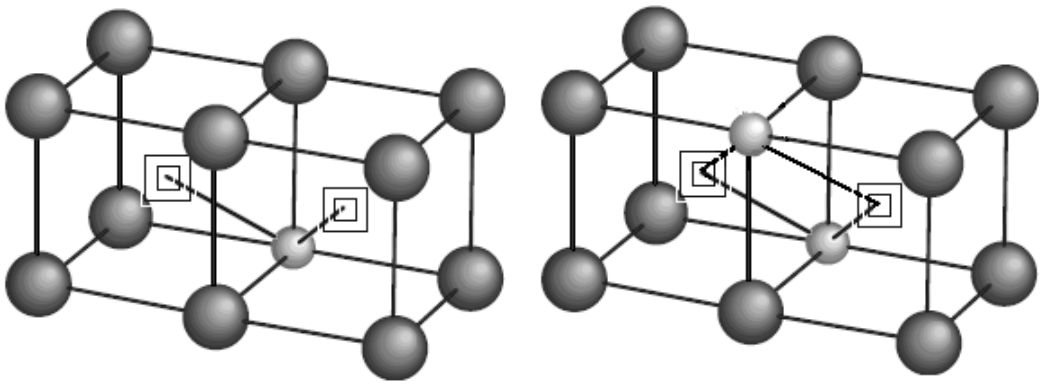

(a) Triple defect (b) 2vac+2Fe_{Al}

Figure 41: Geometry of (a) triple defects and (b) 2vac+2Fe_{Al} in Fe-Al alloys. Bigger atoms are Al, smaller are Fe atoms, squares represents a divacancy in A-sublatice.

Table VII: Fraction of annihilations with Al-atoms f_{Al}[%] calculated for some compositions and various defects. Spread of calculated fractions (one standard deviation) for defects where occupation of NN or NNN sites varies randomly is shown in parenthesis. Spread was estimated from 10 independent calculations.

c_{Al}[%]	vac+Fe_{Al}	vac+NN	2vac+NN	triple	B2-triple	vac+NNN
25	31(10)	66	72	31(10)	59	95
28	33(10)	65	73	35(11)	59	95
30	35(14)	65	72	37(15)	59	95
35	38(9)	66	73	40(15)	59	95
40	47(7)	66	73	48(11)	59	95
45	51(6)	66	73	52(5)	60	95

The results in Table VII show that the calculated positron wavefunction localized in the vacancy is not very sensitive to the lattice parameter of the Fe-Al alloys, since calculated fractions of positrons trapped at a certain defects with defined neighbourhood annihilated by Al electrons are similar for alloys with various compositions.

One can see in Table VII that a positron trapped at the monovacancy surrounded exclusively by the Al-atoms in NN sites is annihilated with $\sim 66\%$ probability by Al electrons. It means although positron is localized in vacancy there is still non-negligible positron density at NNN sites. For a monovacancy surrounded not only by Al atoms in the NN sites but also by additional Al-atoms in NNN sites the probability that positron will be annihilated by Al electron becomes

$\sim$ 95%. The divacancy with NN Al-atoms has slightly higher Al-annihilation fraction $\sim$ 73% because the open volume of the defects is increased and localization of trapped positron is stronger. In case of the triple defect surrounded by Al atoms, which is created by adding one Fe-atom to the vicinity of the divacancy, the fraction of positrons annihilated by Al electrons is decreased to the value $\sim$ 59%, which is even slightly lower than corresponding fraction for monovacancy with NN sites occupied by Al.

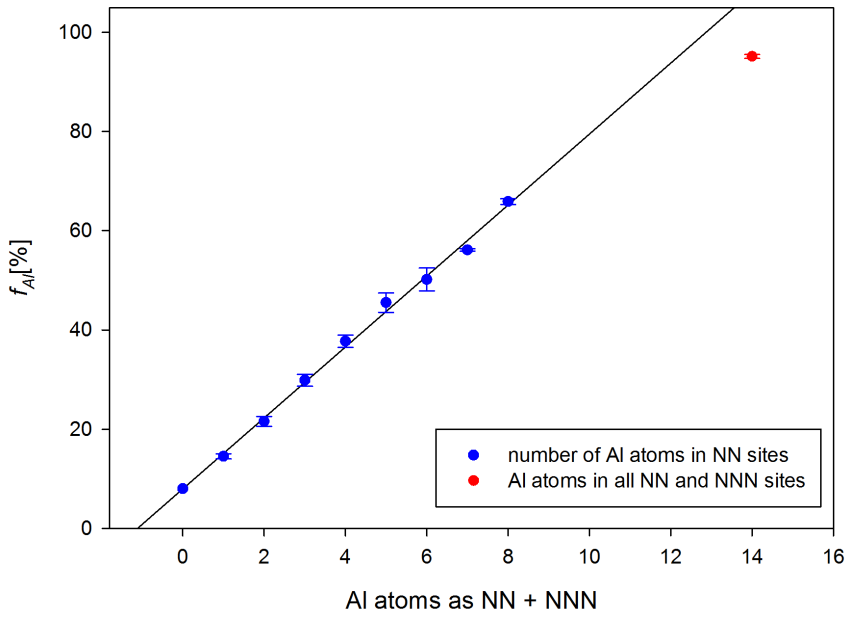

Figure 42: The fraction of positrons annihilated by Al electrons f_{Al} for various numbers of Al atoms occupying NN sites around the vacancy in the A-sublatice of B2 structure (blue points). For comparison the fraction f_{Al} calculated for vacancy in the A-sublattice surrounded by Al atoms in all NN and also NNN sites (vac+NNN) is shown by the red point.

From the Table VII it is obvious that the number of the Al atoms in the vicinity of the monovacancy considerably influences the fraction of positrons annihilated by Al electrons. This is illustrated in the Figure 42 showing dependence of f_{Al} on the number of Al atoms occupying NN sites (0-8) in the B2 structrure. For comparison the fraction of f_{Al} for vac+NNN defect is shown in the figure as well. In completely ordered B2 structure all 8 NN sites around a vacancy in the A-sublattice are located in the B-sublattice and occupied by Al atoms, while 6 NNN sites are located in the A-sublattice and occupied by Fe atoms. All the 14 NN and NNN sites must be occupied by Al atoms in order to achieve 100% probability that positron will be annihilated by Al electron. Hence, positron density becomes negligible at the distance from vacancy higher than radius of the second coordination shell. It means atoms in NN and NNN sites must be considered in estimation of the fraction of positrons annihilated by Al electron.

In Table VIII are listed the lifetimes of a positron trapped at the certain defects. In case of B2 phase in Fe-Al alloys with Al content below 50% the B-sublattice contains both Al and Fe atoms. For this reason several independent

calculations were performed for each composition. The calculations were made in B2 supercell with the B-sublattice randomly filled by Fe and Al atoms keeping the total composition in the supercell equal to the composition of the alloy considered. For defects vac+NN, 2vac+NN, B2-triple, vac+NNN, where type of atoms in all NN and NNN sites is fixed and only occupation of other sites was varied three independent calculations were performed. Ten calculation were performed for other defects where type of atoms in NN or NNN sites was varied (vac+Fe_{Al}, triple) in order to achieve sufficient statistics. The mean values of the calculated lifetimes are shown in Table VIII. Estimated dispersion for each value is given in brackets. Results of calculations are illustrated in Figure 43.

Table VIII: Calculated lifetimes of positrons trapped at various defects in Fe-Al alloys with Al content c_{Al}. Estimated spread of calculated lifetimes due to random variations in chemical environment of defects is given in parenthesis.

$c_{Al}[\%]$	vac+Fe_{Al}	vac+NN	2-vac+NN	triple	B2-triple	vac+NNN
25	187(2)	193.56(5)	202.98(1)	194.3(6)	200.22(3)	197.50(7)
28	187(2)	193.3(2)	202.72(8)	194.8(7)	199.92(9)	197.3(1)
30	187(2)	193.1(1)	202.54(3)	195.0(9)	199.73(5)	197.1(1)
35	187(2)	193.14(2)	202.41(1)	195.5(9)	199.61(1)	197.06(4)
40	189(1)	193.50(1)	202.78(1)	197.1(7)	199.98(2)	197.42(1)
45	190(1)	194.46(5)	203.73(5)	198.9(3)	200.92(4)	198.46(1)

The values in Table VIII show that lifetime of localized positron is not very sensitive to variations of the composition and the lattice parameter of Fe-Al alloys. However, positron lifetime is strongly influenced by open volume of defect and its chemical environment. Divacancy is characterized by higher positron lifetime because its open volume is higher and therefore electron density in divacancy is lower than in monovacancy. For the same reason the positron lifetime of the triple defect, which is constructed from divacancy, is slightly higher than the lifetime of monovacancy in VI.

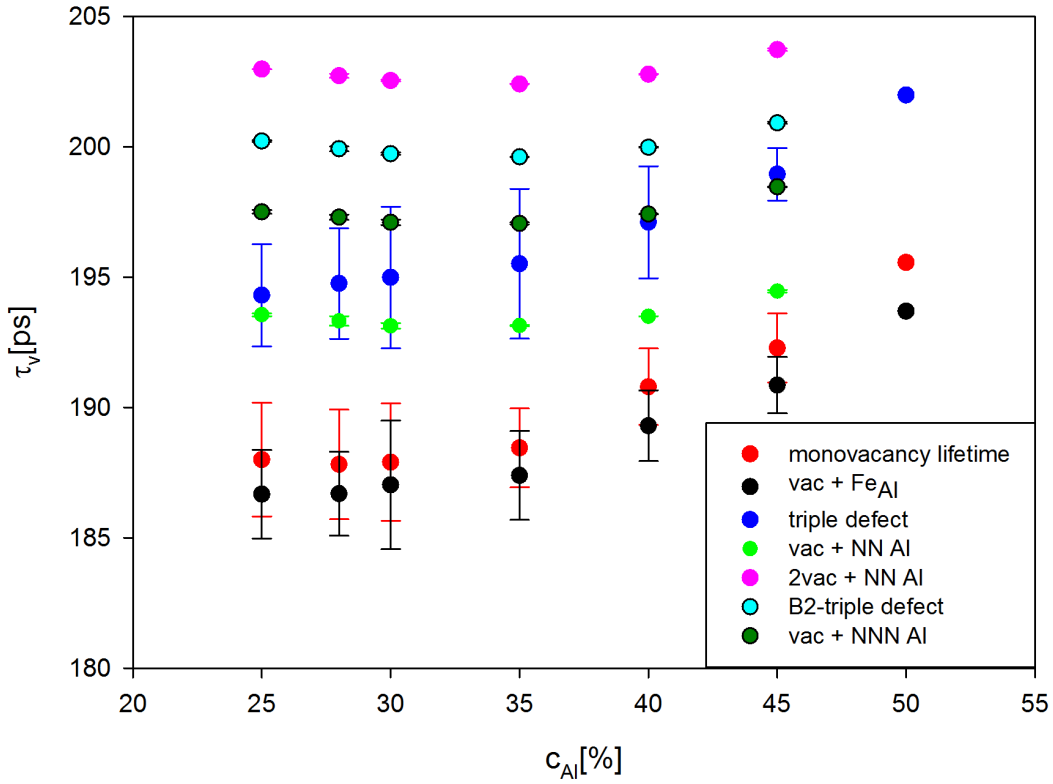

Figure 43: Lifetime of a positron trapped at various defects.

Chapter 5

Discussion

5.1 Hardening effect of vacancies

The microhardness of $Fe_{60.46}Al_{39.54}$ and $Fe_{55.38}Al_{44.62}$ alloys decreases in the temperature range 400-500 °C, see Figure 13. Unfortunately, the vacancy concentration in these samples is impossible to determine by positron lifetime measurement due to saturated positron trapping. However, positron lifetime investigations of $Fe_{75}Al_{25}$ alloy, which exhibits lower concentration of vacancies and saturated positron trapping does not occur here, revealed a decrease in the vacancy concentration in the temperature range 400-480 °C, see Figure 29. Moreover, comparison of vacancy concentration of quenched samples with annealed samples shown in Figure 24 clearly prove that the annealing of Fe-Al alloys at 520 °C decreases the vacancy concentration in Fe-Al alloys of various composition.This testifies that recovery of vacancies takes place in this temperature interval. Hence, it is reasonable to assume that the drop of microhardness observed in the temperature range 400-500 °C in $Fe_{60.46}Al_{39.54}$ and $Fe_{55.38}Al_{44.62}$ alloys is caused by recovery of vacancies.

As discussed in Section 3.3 only the vacancy concentrations above 10^{-4} at.$^{-1}$ has a measurable hardening effect on Fe-Al alloys. Hence, relatively low concentration of vacancies in $Fe_{75}Al_{25}$ alloy explains why microhardness of this sample remains almost unchanged during isochronal annealing, see Figure 13. On the other hand, microhardness of $Fe_{60.46}Al_{39.54}$ and $Fe_{55.38}Al_{44.62}$ alloys is strongly influenced by vacancies and, thereby, recovery of vacancies causes significant softening.

5.2 Comparison of PAS results with ab-inito theoretical calculations

Experimental PAS results should be compared with ab-inito theoretical calculations of positron parameters described in section 4.1.2 in order to identify type of quenched-in vacancies in Fe-Al alloys.

CDB measurements revealed that the fraction $\xi_{Al,v}$ of positrons trapped at vacancies and annihilated by Al electrons significantly increases with increasing Al content, see Figures 22 and 26. The point defects as vac + NN, 2vac + NN, B2-triple and vac + NNN exhibit $\xi_{Al,v}$ almost independent from Al content c_{Al}, see

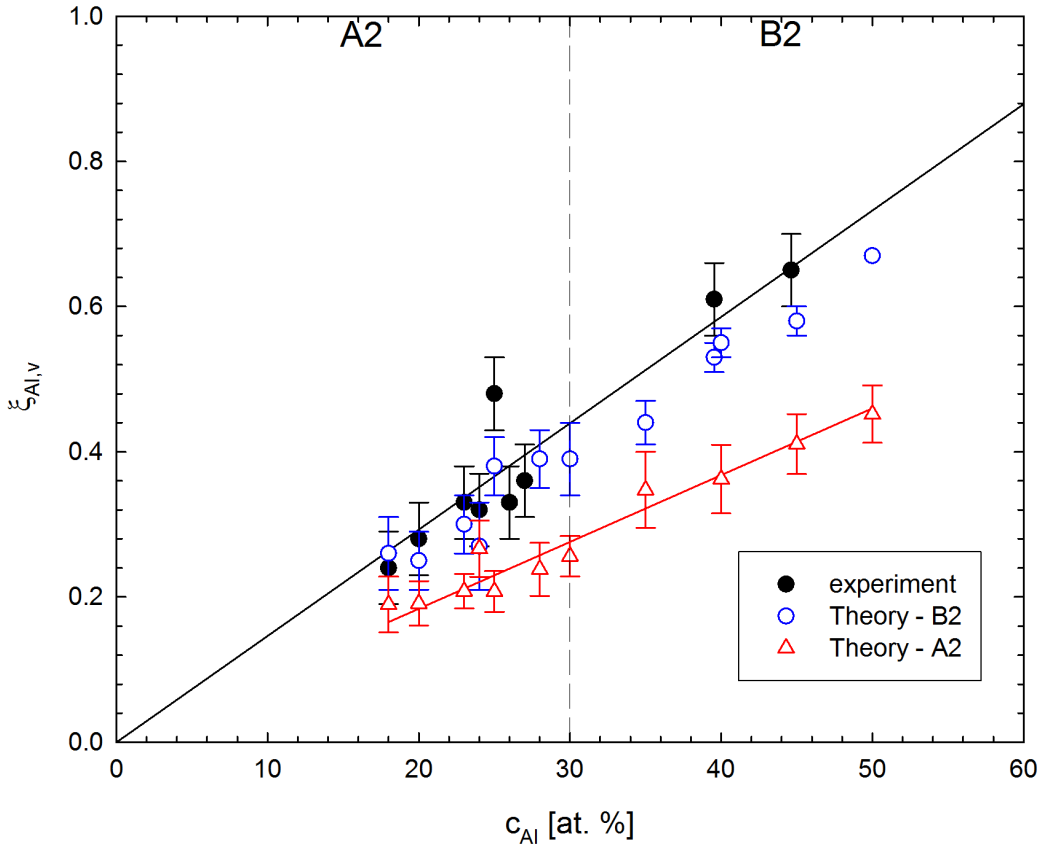

Figure 44: Experimental and theoretical values of $\xi_{Al,v}$ for various Fe-Al alloys quenched from 1000 °C. Experimental values were obtained from PAS measurements of positron lifetime and Doppler broadening of CDB peak. Theoretical calculations for positron trapped at a monovacancy in A2 structure and a monovacancy on A-subblatice of B2 structure exhibit lower $\xi_{Al,v}$ than experimental values. Vertical line shows which phase is formed at 1000 °C according to equilibrium phase diagram in Figure 3.

Table VII. Therefore, one can exclude the defects consisting from only Al atoms in NN or both NN and NNN sites. Hence, although these defects may be present in the alloys with high Al content (close to $Fe_{50}Al_{50}$ composition) they can be ruled out from a list of possible candidates for quenched-in defects in Fe-Al alloys with lower Al content. This is supported also by the fact that the lifetime τ_2 of positrons trapped in quenched-in defects considerably increases with Al content, see Figure 17(a). On the contrary, Table VIII shows that the defects vac+NN, 2vac+NN, B2-triple and vac+NNN exhibit only moderate increase in calculated positron lifetime τ_v.

Vacancy in the A-sublattice, vac+Fe_{Al} and triple defect are remaining possible candidates for quenched-in defects in Fe-Al alloys. All these defects exhibit variable number of Al atoms in NN sites, which is in accordance with increase of τ_2 and $\xi_{Al,v}$ with Al composition observed in the experiment.

Figure 44 shows the fraction $\xi_{Al,v}$ of trapped positrons annihilated by Al electrons determined by fitting of CDB ratio curves plotted as a function of Al con-

tent. In addition, the fraction $\xi_{Al,v}$ obtained from theoretical calculations for monovacancies in A2 structure and in the A-sublattice of B2 structure in Fe-Al alloys of various composition are plotted in the figure as well. Theoretical calculations were performed for

(i) Fe-Al alloys with B2 structure (i.e. the B-sublattice is filled randomly by Fe and Al atoms, while the A-sublattice is occupied by Fe atoms only),

(ii) Fe-Al alloys with A2 structure (i.e. both sublattices filled randomly with Fe and Al atoms).

Phase diagram in Figure 3 declare that the samples with $c_{Al} > 30\%$ quenched from 1000 °C exhibit A2 structure, which was supported by the XRD measurement on sample $Fe_{75}Al_{25}$ in Figures 4 and 5. Samples with $c_{Al} < 30\%$ exhibit B2 phase. However, Figure 44 claims that for Fe-Al alloys with $c_{Al} < 30\%$ quenched in A2 phase is the measured $\xi_{Al,v}$ value slightly higher than showed the teoretical calculations performed on A2 supercell. Moreover, one can notice in Figure 44 that experimental $\xi_{Al,v}$ values agree very well with those calculated for vacancies in the B2 phase. This indicates that quenched-in defects in Fe-Al alloys with $c_{Al} > 30\%$ which are quenched from the B2 phase are monovacancies in the A-sublattice typical for the B2 phase with the corresponding composition. On the other hand, Fe-Al alloys with $c_{Al} < 30\%$ which are quenched from the A2 phase exhibit quenched-in vacancies resembling that in the B2 phase, i.e. vacancies in the A-sublattice with Al atoms occupying NN sites on the B-sublattice but not NNN sites on the A-sublattice. This result indicates that in Fe-Al alloys with low Al content an attractive interaction exists between Al atoms and vacancy. Such attractive interaction was predicted by ab-initio theoretical calculations [14]. One can see clearly in Figure 44 that local environment of vacancies is enriched by Al when comparing to completely random distribution of Al atoms corresponding to the A2 phase.

Figure 45 shows correlation of defect component lifetime τ_2 with the fraction $\xi_{Al,v}$ of trapped positrons annihilated by Al electrons. Calculated values for various defects are shown in the figure as well. Experimental data are compared with theoretical calculations for various defects including vacancy in the A-sublattice in the B2-phase and in the A2 phase. From inspection of Figure 45 one can conclude that although the fraction $\xi_{Al,v}$ calculated for the vacancy in B2 phase is in a good agreement with experiment (as proved already in Figure 44), the calculated lifetime of trapped positrons is higher than experimental values in alloys with low Al content. This discrepancy is most probably due to inward relaxation of NN atoms towards vacancy which reduces lifetime of trapped positrons and is most pronounced in Fe-Al alloys with low Al content. This can be easily understood taking into account the attractive interaction between Al atom and vacancy and repulsive interaction between Al atoms [14]. Vacancies in Fe-Al with low Al content are surrounded by low number of Al atoms, therefore, the attractive interaction between Al and vacancy dominates and inward relaxation of Al towards vacancy is relatively strong. With increasing Al content the number of Al atoms surrounding vacancy increases as well. As a consequence the attractive interaction between Al and vacancy is compensated by the repulsive Al-Al interaction. This makes the relaxation of Al atoms substantially smaller.

It should be mentioned that several authors [24, 25] reported attractive interaction between vacancies in the A-sublattice leading to formation of triple defects,

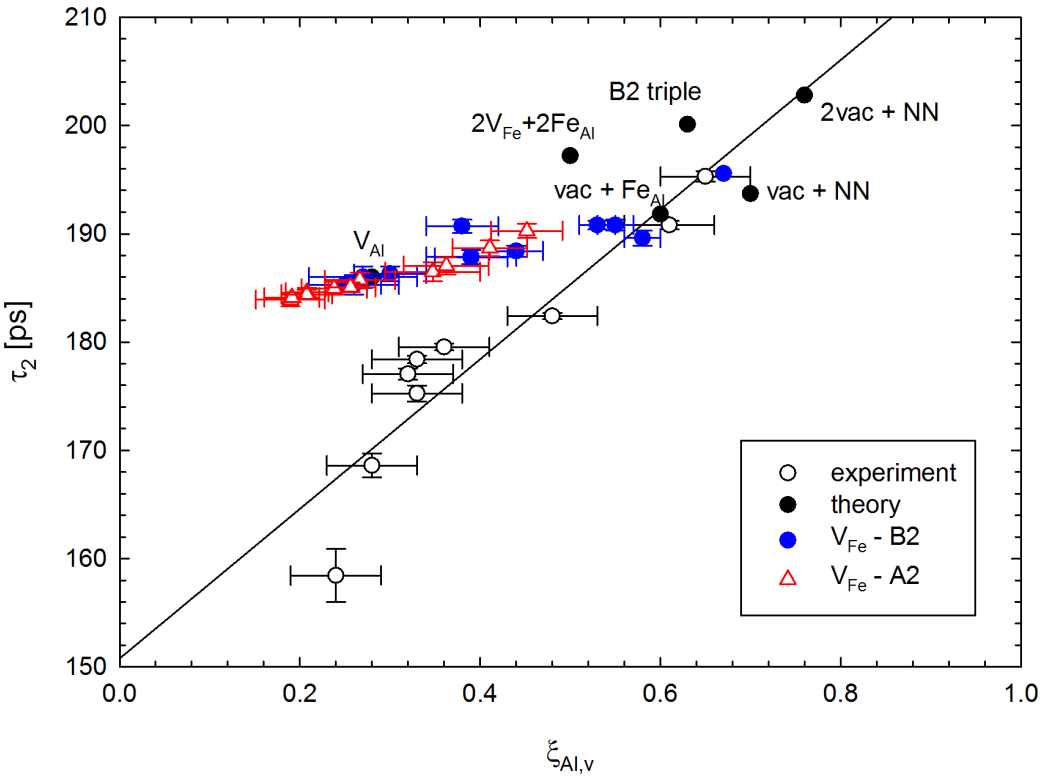

Figure 45: Correlation of defect lifetime component with $\xi_{Al,v}$ of Fe-Al alloys quenched from 1000°C compared with the results of theoretical calculations for various types of defects from Section 4.1.2.

i.e. pairs of vacancies aligned in the [100] direction in the A-sublattice associated with Fe antisite atom in the B-sublattice (see Figure 41(a)). in Fe-Al alloys with high Al content. One can see in Figure 45 that the point calculated for the triple defect in the ordered B2 structure (B2-triple) lies very close to the experimental point for $Fe_{55.38}Al_{44.62}$ alloy. Hence, formation of triple defects by attractive interaction of vacancies in Fe-Al alloys with Al content approaching 50% is very probable.

Figure 42 shows $\xi_{Al,v}$ calculated for monovacancy in B2-sublattice surrounded by different number of Al atoms which enables the comparison with $\xi_{Al,v}$ obtained by PAS measurements. A monovacancy in perfectly ordered B2 structure has 8 NN Al atoms. CDB results of $\xi_{Al,v}$ of various Fe-Al alloys plotted in Figure 26 increase with increasing Al content. Therefore, number of Al atoms in the vicinity of the monovacancy is increasing with increasing Al content. Moreover, quenched and annealed samples with Al content from $c_{Al} = 24\%$ to 28% exhibit similar $\xi_{Al,v}$ although in the quenched samples A2 phase is formed while in the annealed samples $D0_3$ ordered phase forms during annealing at 520 °C. Isochronal annealing of Fe-Al alloys in Section 3.4.5 clearly showed that the fraction $\xi_{Al,v}$ remains constant (see Figure 33), and therefore the defect type does not change during annealing. Moreover, defect type is not influenced even by phase transition as seen in sample $Fe_{75}Al_{25}$ and depends exclusively on composition of Fe-Al alloy.

Chapter 6

Conclusions

(I) Crystal structure and lattice parameter of various Fe-Al alloys were determined by X-ray diffraction measurements. The quenched alloys with Al content below 30% exhibit A2 structure while the alloys with higher Al content exhibit B2 structure.

(II) Positron annihilation spectroscopy of quenched Fe-Al alloys of various compositions revealed very high concentrations of vacancies. Concentration of vacancies strongly increases with Al content from $\sim 10^{-5}$ in $Fe_{82}Al_{18}$ up to $\sim 5 \times 10^{-2}$ in $Fe_{55.38}Al_{45.62}$ alloy.

(III) Recovery of quenched-in vacancies by thermally activated diffusion into sinks takes place in the temperature range 350 - 500 °C. In alloys with composition close to $Fe_{75}Al_{25}$ it is accompanied by ordering into $D0_3$ phase.

(IV) Correlation of microhardness with vacancy concentrations above $10^{-4}at^{-1}$ confirmed vacancy hardening of Fe-Al alloys.

(V) Comparison of quantum mechanical theoretical calculations with experimental results of positron annihilation spectroscopy revealed preferential occupation of vacancy NN sites by Al atoms. Quenched-in defects were identified as monovacancies in the A-sublattice with local chemical environment resembling that in B2 phase even when the quenched alloy exhibits disordered A2 phase. In alloys with high Al content approaching 50% the attractive interaction of vacancies leads to formation of triple defects, i.e. two vacancies in the A sublattice aligned in the [100] direction and associated with Fe antisite atom on the B sublattice.

References

[1] Dupasquier A., Mills A.P. (eds.): *Proceedings of the International School of Physics Enrico Fermi*, IOS Press, Varenna (1995).

[2] Bečvář F., Čížek J., Procházka I., Janotová J.: *The asset of ultra-fast digitizers for positron-lifetime spectroscopy*, Nuclear Instruments and Methods in Physics Research A **539**, 372-385 (2005) 372-385.

[3] Bečvář F., Čížek J., Procházka I.: *High-resolution positron lifetime measurement using ultra fast digitizers Acqiris DC211*, Applied Surface Science **255**, (2008) 111–114.

[4] Bardeen J., Shockley W.: *Deformation Potentials and Mobilities in Non-Polar Crystals*, Phys. Rev. **80** (1950) 72–80

[5] Schaefer H. E., Damson B., Weller M., Artz E., George E. P.: *Thermal Vacancies and High-Temperature Mechanical Properties of FeAl* Phys. stat. sol. (a) **160** (1997) 531–540

[6] Kittel Ch.,: *Úvod do fyziky pevných látek*, Academia, Praha, (1985) Kapitola 1 - Krystalová struktura, 21-34

[7] Hall M.M.: *The Approximation of Symmetric X-Ray Peaks by Pearson Type VII Distributions* J. Apl. Cryst. **10** (1977) 66.

[8] Kužel R., *http://krystal.karlov.mff.cuni.cz/kfes/vyuka/lp/*

[9] Boroński E., Nieminen R.M: *Electron-positron density-functional theory*, Phys. Rev. B **34** (1986) 3820.

[10] Puska M. J., Nieminen R. M.: *Defect spectroscopy with positrons: a general calculation method*, J. Phys. F: Met. Phys. **13** (1983) 333-346.

[11] Harju A., *Positron lifetime calculations for the High T_C superconducting Copper-Oxide material $Nd_{2-x}Ce_xCuO_{4-\delta}$*, Master's Thesis, Helsinki University of Technology, Espoo (1994).

[12] Kubaschewski, O.: *Fe-Al in Binary-Iron Phase Diagrams* Springer Verlag, Berlin, (1982) 5–9

[13] Allen S. M., Cahn J. W.: *A microscopic theory for antiphase boundary motion and its application to antiphase domain coarsening*, Acta Metallurgica, (1979), **27** 1085-1095

[14] Amara H., Fu C. C., Soisson F., Maugis P.: *Aluminum and vacancies in α-iron: Dissolution, diffusion, and clustering* Phys. Rev. B **81** (2010) 174101

[15] Chang Y. A., Pike L. M., Liu C. T., Bilbrey A. R., Stone D. S.:*Correlation of the hardness and vacancy concentration in FeAl*, Intermetallics **1** (1993) 107–115

[16] Bečvář F.: *Methodology of positron lifetime spectroscopy: Present status and perspectives*, Nuclear Instruments and Methods in Physics B **261** (2007) 871–874.

[17] James F.:*MINUIT tutorial on Function Minization* CERN (2004) http://seal.web.cern.ch/seal/MathLibs/Minuit2/html/index.html

[18] McGuire S., Keeble D.J. *Positron lifetimes of polycrystalline metals: A positron source correction study* J. Appl. Phys. **100**, (2006) 103504

[19] Schaefer H. E., Wűrschum R., Šob M., Žák T., Yu W. Z., Eckert W., Banhart F.: *Thermal vacancies and positron-lifetime measurements in $Fe_{76.3}Al_{23.7}$*, Phys. Rev. B **41** (1990) 11869–11874

[20] Golovin I.S., Divinski S.V., Čížek J., Procházka I., Stein F.: *Study of atom diffusivity and related relaxation phenomena in Fe_3Al-(Ti,Nb)-C alloys* Acta Materialia **53** (2005) 2581-2594

[21] Smedskjaer L. C., Manninen M., Fluss M. J.: *An alternative interpretation of positron annihilation in dislocations* J. Phys. F: Met.Phys. **10** (1980) 2237

[22] Taylor A., Jones R. M.: *Constitution and magnetic properties of iron-rich iron-aluminium alloys*, J. Phys. Chem. Solids **7** (1958) 16-37.

[23] Fähnle M., Mayer J., Meyer B.: *Theory of atomic defects and diffusion in ordered compounds, and application to B2-FeAl*, Intermetallics **7** (1999) 315-323.

[24] Fu C.L., Ye Y.-Y., Yoo M.H., Ho K.M.:*Equilibrium point defects in intermetallics with the B2 structure: NiAl and FeAl*, Phys Rev B **48** (1993) 6712

[25] de Diego N., Plazaola F., Jiménez J.A., Serna J., del Río J.: *A positron study of the defect structures in the $D0_3$ and B2 phases in the Fe-Al system*, Acta Materialia **53** (2005) 163–172.

List of Tables

List of Abbreviations

APB - Antiphase boundaries
BCC - Body centered cubic
CDB - Coincidence Doppler broadening
DFT - Density functional theory
FCC - Face centered cubic
FWHM - Full width at half maximum
HF - Hartree-Fock method
LDA - Local density approximation
LRO - Long range order
LT - Lifetime spectroscopy
NIM - Nuclear instrumentation modul
NN - Nearest neighbour
NNN - Next nearest neighbour
PAS - Positron annihilation spectroscopy
PC - Personal computer
SIC - Self-interacting correction
SPIS - Slow positron implantation spectroscopy
SRO - Short range order
STM - Simple trapping model
XRD - X-ray diffraction

Appendix A

INPUT file for ATSUP code

```
ATSUP_3.18
HEADER
          Fe-Al, test version 3.18
SWITCHES  modes_of_calculation
           ATSUP
!            ATSUP   HMC2
ENHANCE   enh_switch dieps_or_alpha
          BN  9999999999.d0
!          SL  9999999999.d0
!          SK  9999999999.d0
!          GC  0.22
POSITRON  #levels energies    mass
          1       1.0         1.0
3DMESH    nr1 nr2 nr3
          100 100 100
!         24  24  24
MESHLIMIT mesh_reduction_(+-x,+-y,+-z), averaging_(x,y,z), energy
          0 0  0 0  0 0   0 0 0    0.0
BOUNDARY  BC_type_in_all_directions, init., average
           1  1  1   0 1
!         -1 -1 -1   1 1
!          0  0  0   1 1
ATOM      atomic_numbers_of_all_species
           26  13
LATTICE   lattice_constant cutoff units
!         6.23689 12.0   au
          5.818  12.0    aa
VECTORS   lattice_translation_vectors (in three lines)
          4.0 0.0 0.0
          0.0 4.0 0.0
          0.0 0.0 4.0


POSITION  types_and_coordinates_of_all_atoms
```

```
          1   0.000000000000000   0.000000000000000   0.000000000000000
          2   0.500000000000000   0.500000000000000   0.500000000000000
ITERATION #iterations precision preconditioning KSnew?
          500  1.d-12   0.01                    1
OUTPUT    output_switches
           ma dp de
!           no

HMC       HMC_basic_parameters:  prmax npr wfminr cutoff2 units
          100.0  200    1.d-20   5.0  au
SAVERAGE  HMC_averaging_parameters: pdir(3)  nth nph
          0. 0. 0.   10 20
ORBITAL   orbital_info_for_hmc:
          1 8 1 8 1 4 1 4
WPARAM    range_for_W-parameter_calculation: p1 p2
          15. 25.
RFUNCTION resolution_function_parameters: FWHM
          3.9
```